

Mass Spectrometry Technologies for Spaceflight Applications
by

Tanouir Aloui

Department of Electrical and Computer Engineering
Duke University

Defense Date: November 21st, 2023

Approved:

Jeffrey T. Glass, advisor

Jason J. Amsden, co-advisor

Michael Gehm

Hisham Massoud

Adrienne Stiff-Roberts

Dissertation submitted in partial fulfillment of the requirements for the degree of Doctor
of Philosophy in the Department of Electrical and Computer Engineering in The Graduate School
of
Duke University
2023

ABSTRACT

Mass Spectrometry Technologies for Spaceflight Applications

by

Tanouir Aloui

Department of Electrical and Computer Engineering
Duke University

Defense Date: November 21st, 2023

Approved:

Jeffrey T. Glass, advisor

Jason J. Amsden, co-advisor

Michael Gehm

Hisham Massoud

Adrienne Stiff-Roberts

An abstract of a dissertation submitted in partial fulfillment of the requirements for the degree of
Doctor of Philosophy in the Department of Electrical and Computer Engineering in The Graduate
School of
Duke University
2023

Copyright by
Tanour Aloui
2023

Abstract

The National Research Council's Planetary Science 2013-2022 Decadal Survey underscores three interrelated themes pivotal to planetary science research: understanding solar system beginnings, searching for the requirements for life, and understanding the workings of solar systems. *In situ* mass spectrometry (MS) is the primary technique for the analysis of planetary substances, directly addressing the critical inquiries associated with these themes. The quintessential mass analyzer engineered for space exploration is envisioned to embody a suite of features: a mass range extending from 1 u to at least 500 u, capability for high-precision measurement of stable isotope ratios within a tolerance of $\pm 1\%$, and the ability to resolve distinct isobaric species at a low mass below 60 u, all with low power requirements. Incorporation of these capabilities within a single instrument is crucial for facilitating the exploration of the necessities of life and for advancing our understanding of solar system genesis and planetary development. Nevertheless, state-of-the-art existing spaceflight mass spectrometers do not fully integrate all these capabilities.

In this research, three technologies are investigated to close this gap; spatial aperture coding, super-resolution, and field emission electron sources. The development of these three technologies as presented in this dissertation represent a significant step towards a mass spectrometer having all of the characteristics described above.

First, Spatial aperture coding is a technique used to improve throughput without sacrificing resolution, historically in optical spectroscopy, and more recently as demonstrated by our laboratory at Duke University, in sector mass spectrometry (MS). Previously we demonstrated that aperture coding combined with a position-sensitive array detector in a miniature cycloidal mass spectrometer was successful in providing high-throughput, high-resolution measurements.

However, due to poor alignment and field non-uniformities, reconstruction artifacts were present. In this dissertation, two methods were implemented to significantly reduce the presence of artifacts in reconstructed spectra. First, I employed a variable system response function across the mass range (10 – 110 u) instead of using a fixed function. Second, I modified the design by shifting the coded aperture slits relative to the center of the ionization volume to enable even illumination of the coded aperture slits. Both methods were successful in significantly reducing artifacts at low mass from above 35% of the peak height to less than 6% of the peak height.

Second, higher resolution in fieldable mass spectrometers (MS) is desirable in space flight applications to enable resolving isobaric interferences at $m/z < 60$ u. Resolution in portable cycloidal MS coupled with array detectors could be improved by reducing the slit width and/or by reducing the width of the detector pixels. However, these solutions are expensive and can result in reduced sensitivity. In this dissertation, I demonstrate high-resolution spectral reconstruction in a cycloidal coded aperture miniature mass spectrometer (C-CAMMS) without changing the slit or detector pixel sizes using a class of signal processing techniques called super resolution (SR). I developed an SR reconstruction algorithm using a sampling SR approach whereby a set of spatially shifted low-resolution measurements are reconstructed into a higher-resolution spectrum. This algorithm was applied to experimental data collected using the C-CAMMS prototype. It was then applied to synthetic data with additive noise, system response variation, and spatial shift nonuniformity to investigate the source of reconstruction artifacts in the experimental data. Experimental results using two 1/2 pixel shifted spectra resulted in a resolution of 3/4 pixel full width at half maximum (FWHM) at $m/z = 28$ u. This resolution is equivalent to 0.013 u, six times better than the resolution previously published at $m/z = 28$ for N_2^+ using C-CAMMS. However, the reconstructed spectra exhibited some artifacts. The results of the synthetic data study indicate that the artifacts are most likely caused by the system response

variation. Despite these artifacts, it was shown that the super-resolution algorithm is capable of resolving the isobaric interference between N_2 and CO at $m/z = 28$.

Third, Field emission electron sources for MS electron ionization have been of interest to spaceflight applications due to their low power compared to thermionic sources. However, state-of-the-art devices suffer from limitations such as high turn-on macroscopic field, low macroscopic current density, poor emission stability, and short lifetime. Field emitter arrays with a high spatial density of uniform emitters have the potential to address these problems. In this work, process development, fabrication, and testing of two novel field emission based devices are presented, including CNT array emitters and metallic nanowires. Instability in CNT emission was investigated using noise analysis and a polymer encapsulation process to reduce the effect of adsorbates on the tips of CNTs. This treatment was not successful in reducing emission noise in CNTs. Thus, electron beam lithography and templated electrodeposition were used to fabricate a high spatial density array of metallic nanowires, resulting in electron field emission with high macroscopic current density (2 A/cm^2) and low turn-on macroscopic field ($4.35 \text{ V}/\mu\text{m}$). Results indicate that templated electrodeposition of metallic nanowire arrays is a promising method for producing high performance field emitters.

Dedication

To them, Palestinian children of Gaza.

This work was supposed to be dedicated to my parents and sister, my loving family, but the war happened when I started writing in October 2023. Thus, every chapter, every section and every word were typed with lots of tears. Reading it again reminds me of the innocent faces of the over 5000 children killed in the past four weeks in Gaza. I know many of them wanted to become scientists, but their dreams were, unfortunately, erased too soon. Children of Gaza, since you all are dear family members to me, please allow me to be your scientist.

The total number of civilians killed in Gaza as of today, November 6th, 2023 is more than 10022. 70% of them are children and women. But we are not numbers!

Contents

Abstract.....	iv
List of Tables	ix
List of Figures.....	x
Acknowledgements.....	xiv
1.Introduction	1
1.1 Mass spectrometers in planetary exploration.....	1
1.1.1 Motivations	1
1.1.2 History of spaceflight MS	2
1.1.3 Current state of the art in space flight MS for planetary exploration	3
1.2 Background	6
1.2.1 Cycloidal mass analyzers	6
1.2.2 Ion array detectors.....	8
1.2.3 Computational Sensing and spatial aperture coding	9
1.3 Research objectives.....	11
1.3.1 Reducing spectral reconstruction artifacts in C-CAMMS	11
1.3.2 Implementation of super-resolution in mass spectrometry	11
1.3.3 Field emission electron ionization	12
1.4 Dissertation outline	14
2. Enhancements for optimizing C-CAMMS reconstruction performance using spatially coded apertures.....	15
2.1 Introduction	15
2.2 Methods.....	17
2.3 Results and discussion.....	19

2.3.1 Introduction	19
2.3.2 Reconstruction with a variable system response.....	22
2.3.3 Reconstruction with spatially shifted coded aperture	23
2.4 Conclusion.....	26
3. A Super-Resolution proof of concept in a cycloidal coded aperture miniature mass spectrometer.....	28
3.1 Introduction.....	28
3.2 SR problem definition and solution framework.....	30
3.2.1 Super-resolution as an inverse problem.....	30
3.2.2 SR reconstruction: solving the SR inverse problem	33
3.2.2.1 Previous work on SR with a 1-D array detector.....	34
3.2.2.2 Characteristics of the SR transfer matrix.....	34
3.2.2.3 SR reconstruction approach used in this research	37
3.3 Results and discussion.....	39
3.3.1 Experimental results using C-CAMMS	39
3.3.2 Synthetic study using simulated spectra	45
3.3.3 SR-CAMMS isobaric separation of N ₂ and CO.....	52
3.4 Summary and conclusions.....	56
4. Field emission electron sources	58
4.1 Introduction	58
4.1.1 Motivations	58
4.1.2 Theoretical background and definitions.....	60
4.2 Carbon Nanotube based field emission electron sources.....	61
4.2.1 Methods.....	62
4.2.1.1 Device fabrication process.....	62

4.2.1.2 CNT growth.....	63
4.2.1.3 Encapsulation treatment	65
4.2.2 Results and discussion	66
4.3 Electron emission from an electrodeposited metal nanowire array	72
4.3.1 Experimental procedure	73
4.3.2 Results and discussion	77
4.3.2.1 Current-voltage measurement.....	77
4.3.2.2 Stability measurement	78
4.4 Summary and conclusions.....	79
5. Conclusions and future perspectives	81
5.1 Spatially coded apertures	81
5.2 Super-resolution reconstruction	82
5.2 Field emission electron sources	83
Appendix A.....	86
References.....	92
Biography	105

List of Tables

Table 1: Characteristics of an ideal mass analyzer for planetary exploration.	2
Table 2: comparison of space flight mass spectrometers	6

List of Figures

Figure 1. Cycloidal mass analyzer with (a) single slit and (b) coded aperture.....	8
Figure 2. Stability of CNT ion source using coded aperture with three slits	14
Figure 3. Stability of filament-based ion source using coded aperture.	14
Figure 4: a) Experimental (blue) and simulated (gray) coded mass spectra of 100 ppm toluene in dry air for electric field = 1143 V/m acquired with the C-CAMMS-MP instrument.....	21
Figure 5: Visual representation of the system response matrix H_{SRF} which is a square diagonal matrix (1704 x 1704) with values over its diagonal and zeros everywhere else.	23
Figure 6: Schematic representation depicting the effect of shifting the coded aperture slits on the corresponding ion trajectories.....	24
Figure 7: a) Experimental (blue) and simulated (gray) coded mass spectra of 100 ppm toluene balanced in dry air for electric field = 1143 V/m acquired with the C-CAMMS-MP instrument .	26
Figure 8: Schematic of super-resolution concept achieving 3x resolution improvement. a. Simulated three raw spectra shifted by a third of a pixel each.	31
Figure 9. Super-resolution reconstruction steps simplified diagram. We consider an ideal high-resolution spectrum S as the input to the instrument (mass analyzer).....	33
Figure 10. a. Coded mass spectrum of air. For ions of each m/z , a sequence of 3 peaks appears at the detector. b. Richardson-Lucy low-resolution reconstruction.....	44
Figure 11: Reconstructions of synthetic data containing no noise, 1% noise, 5% noise, and 10% noise. a-d) representative measurements, e-h) reconstructions of a-d respectively.	47
Figure 12. Reconstructions of synthetic data with variation in the sub-pixel shift. a-d) representative measurements, e-h) reconstructions of a-d respectively.	49
Figure 13. Reconstructions of synthetic data with a mismatch in the system response. a-d) representative measurements, e-h) reconstructions of a-d respectively..	51
Figure 14. Plot of root mean square error between the ideal spectrum and reconstructed spectrum for different amounts of noise, uncertainty in the subpixel shift.....	51
Figure 15. CAD model cross-section of the complete SR-CAMMS prototype.	53
Figure 16. Photograph of graduate student Tanouir Aloui holding the fully assembled SR-CAMMS electric sector.	54

Figure 17 Data for 100% N ₂ (blue) and a mixture of 10% CO and 90% N ₂ (orange). A) Data before reconstruction. B) Data before reconstruction zoomed in.....	56
Figure 18: schematic of the energy diagram representing electron field emission from a metal surface into vacuum.....	60
Figure 19: a) SEM image of 6 patterned CNT patches. b) Zoomed in SEM image of 1 of the 6 patches.	65
Figure 20. a) Cross section view of a typical CNT film grown using MPECVD. b) cross section view of an attempt at encapsulating a CNT film with PMMA.....	66
Figure 21. Photograph of the experimental setup. On the left is the high vacuum chamber held at 10 ⁻⁸ Torr. On the right is a photo of the CNT sample holder inside the vacuum chamber	67
Figure 22. IV curve from a CNT sample.....	67
Figure 23. Diagram of the circuit for Fourier noise analysis on the CNTs.	68
Figure 24. Fourier transform of the root mean square voltage across the resistor (U_{rms}) for a CNT field emitter (blue) and background noise without field emission.	69
Figure 25. Attempts at encapsulating a CNT film. The PMMA does not penetrate the CNT film and is mostly sitting on the top of the CNTs.	71
Figure 26. Encapsulation using PMMA diluted in its developer MIBK with a 2:1 ratio.....	71
Figure 27: Power spectral density of CNTs as grown (without encapsulation)	72
Figure 28: Power spectral density of encapsulated CNTs.....	72
Figure 29: Schematic of the nanowire fabrication process a) platinum-coated silicon wafer substrate b) EBL to produce arrays of holes ~35 nm in diameter, spaced by 150 nm..	74
Figure 30: SEM images of platinum nanowire array a) overview, the scale bar is 5 μ m b) close-up, the scale bar is 500 nm c) close-up, tilted at 45° away from viewer, the scale bar is 500 nm. 75	75
Figure 31: Schematic of the electron emission measurement apparatus.	76
Figure 32: Field emission measurements of a platinum nanowire field emitter array.	78
Figure 33: Electron emission current measured with the anode at a constant voltage of 700 V....	79
Figure 34: a. Coded mass spectrum of air. For ions of each m/z, a sequence of 3 peaks appears at the detector. b. Richardson-Lucy low-resolution reconstruction.....	86
Figure 35: Reconstructions of synthetic data containing no noise, 1% noise, 5% noise, and 10% noise. a-d) representative measurements, e-h) reconstructions of a-d respectively using CGLS...87	87

Figure 36: Reconstructions of synthetic data with variation in the sub-pixel shift. a-d) representative measurements, e-h) reconstructions of a-d respectively using CGLS..88

Figure 37: Reconstructions of synthetic data with a mismatch in the system response. a-d) representative measurements, e-h) reconstructions of a-d respectively using CGLS.89

Figure 38: a. Coded mass spectrum of air. A sequence of 3 peaks appears at the detector for ions of each m/z . b. Richardson-Lucy low-resolution reconstruction using 10 iterations.90

Figure 39: Schematic flow diagram of the process for the synthetic data study.91

Acknowledgements

I would like to acknowledge and thank my advisors, Prof. Jeffrey Glass, Prof. Jason Amsden, for giving me this opportunity that helped shape me as a researcher. I also want to thank all my lab mates, co-authors, and collaborators for making this hard journey easier. I also thank Dr. Charles Parker for helping me with different lab logistics and research advice. A special thanks goes out to Prof. Hisham Massoud who was a great mentor throughout my time at Duke. I thank Prof. Michael Gehm for his significant input into my research and his well-structured guidance. I would also like to thank each of my committee members, Prof. Adrienne Stiff-Roberts, Prof. Michael Gehm, Prof. Hisham Massoud, and both my advisors for their contribution and valuable feedback throughout my dissertation research and classes. I want to thank SMIF staff members who provided tremendous technical support. I want to thank all my friends for their support through difficult times. In particular, the Center for Muslim life at Duke (CML) for being my family away from home, Bro Jo, Hadeel, Imam Waheed, Professor Kadivar and Maha. Special thanks to my dear mentor from France Professor Mohamed Krir. I can't remember all the names but I am grateful to everyone for their generous support including Sonya, Husna, Nabil, Fayrouz, Afrah, Namyia, Fayrouz, Samira, Mohammed, Ahmed, Noura, Nourhan, Yusuf, AR, Hareth, Laila, Fatima, Wafa, Belinda, Ujue from Spain, Chaima, Ahlem, Ilhem, Atiyat Samira, Manel, Wania, Kulsoom, Saif, Ahmed, Khalil, Nour, Sherif, Shaker, Hafsa, Unzila, Eesha, Mays, Busra, Islam, Ala, Ala, Sehrish, Zeinab, Omar, Saad, baby Baya, Om Mahmoud, Luisa from Brazil, and many more.

Finally, no words can describe how grateful I feel for being blessed from God with caring and supportive family members, especially my parents and sister, Sokkar henem, who believed in me and made my educational dreams come true.

1. Introduction

1.1 *Mass spectrometers in planetary exploration*

1.1.1 Motivations

Mass spectrometry (MS) is a versatile analytical technique that can identify and quantify the composition of chemical samples by measuring the mass-to-charge ratio of charged particles. As such, MS have been and continue to be the primary *in situ* method for analysis of planetary materials to answer priority questions related to understanding solar system beginnings, searching for the requirements for life, and understanding the workings of solar systems as cross-cutting themes of planetary science research described in the 2013-2022 Decadal survey [1-5]. First, Studying the atmospheres of planets and moons can provide valuable insights into their histories and geologies which makes MS the number one instrument for atmospheric analysis because it can identify and quantify the various gases and compounds present, revealing processes like volcanic activity or potential indications of life [6]. Second, MS can help identify organic compounds and potential signs of past or present life, aiding in the search for life beyond Earth. For instance, as NASA explores other planets and celestial bodies, determining the composition of soils, rocks, atmospheres, and ices is essential [7]. Third, comets and asteroids are considered remnants from the early solar system. Thus, analyzing their composition can provide insights into the solar system's origins. MS can help in determining the elemental and molecular makeup of these celestial bodies [8]. In addition to planetary exploration and astrobiology MS can be important for health and safety in spaceflight missions because it can monitor the spacecraft's air quality. MS can detect and measure any potential contaminants or toxins, ensuring the safety of the crew [9].

An ideal mass analyzer for planetary exploration would have the characteristics listed in Table 1. These capabilities would enable the search for the requirements of life and the study of

the solar system and planet formation and evolution. However, as discussed below in section 1.1.3, none of the currently developed space flight mass spectrometers have all these capabilities.

Table 1: Characteristics of an ideal mass analyzer for planetary exploration.

(1)	A mass range from 1 u up to at least 500 u
(2)	Ability to measure stable isotope ratios with high precision (± 1 ‰)
(3)	Ability to distinguish between various isobaric species at low mass (<60 u)

1.1.2 History of spaceflight MS

MS have been introduced to space flight missions for planetary exploration starting with the Viking missions in 1975 [10, 11]. The Viking program consisted of a pair of American space probes sent to Mars, Viking 1 and Viking 2. The main objective of the mission was to search for signs of life on Mars. Although the biological experiments delivered ambiguous results, most scientists now believe that they were due to non-biological reactions of the Martian soil. The Viking landers' Gas Chromatograph MS (GCMS) did not detect any organic compounds, which was a surprising result at the time [12].

More recently, the Mars Curiosity Rover [13], a car-sized rover launched in 2011 and successfully landed on Mars in 2012, was designed to investigate the Martian climate and geology. It is also trying to assess whether the selected field site inside Gale Crater has ever offered environmental conditions favorable for microbial life. A Quadrupole Mass Spectrometer (QMS) that can analyze organics and gases from both atmospheric and solid samples was included in the Sample Analysis at Mars (SAM) suite on Curiosity. While the QMS can assess a wide mass range, its resolution isn't high enough for precise isotope ratio measurements. [14] Hence, Curiosity also carries a laser spectrometer for this purpose.

1.1.3 Current state of the art in space flight MS for planetary exploration

A state of the art MS instrument was supposed to be included in the ExoMars mission [15]. ExoMars was a joint endeavor between the European Space Agency (ESA) and the Russian space agency, Roscosmos. ExoMars was supposed to launch in 2020. However, the ExoMars was cancelled after the war between Russia and Ukraine started in February 2022 [16]. The ESA is taking ownership of the new mission that will be called ExoMars Rosalind Franklin rover [16]. The primary goal of the ExoMars program was to address the question of whether life ever existed on Mars. The MS used in ExoMars, developed by NASA Goddard Space Flight center, is called the Mars Organic Molecule Analyzer (MOMA). MOMA uses a combination of laser desorption and gas chromatography/ ion trap mass spectrometry to analyze samples. While MOMA can detect a wide range of biomolecules like lipids and amino acids, it has some limitations, especially for molecules with a mass-to-charge (m/z) ratio below 50 due to space charge and low mass cut-off limitations. It also has limited capabilities for high precision isotope ratio measurements because of limited sensitivity and precision required to detect the subtle differences in naturally occurring isotopic abundances [17-19].

Europa Clipper is a mission under development that aims to study Europa, one of Jupiter's moons [20]. Europa is considered one of the top places to search for signs of life beyond Earth because of its subsurface ocean. The mission will carry a suite of scientific instruments including a Time-of-flight MS, MASPEX that has extremely high resolution and a large mass range. However, it suffers from low dynamic range due to electron multiplier-based detectors. This lack of dynamic range along with drift of the gain of electron multiplier-based detectors over time makes high precision ($\pm 1\%$) isotope ratio measurements challenging [21].

In July 2020, China's first independent mission to Mars, Tianwen-1, was launched. In May 2021, the Zhurong rover successfully landed on Mars, making China the second nation to

land and operate a rover on the Martian surface. The Tianwen-1 orbiter is equipped with several instruments, including a Mars Energetic Particle Analyzer (MEPA) that uses a time-of-flight mass spectrometer [22].

Also in July 2020, NASA's Mars 2020 mission successfully launched and landed the Perseverance rover on Mars in February 2021. The rover aims to search for signs of past microbial life and collect samples that will be returned to Earth by future missions. The Perseverance rover carried an instrument called SHERLOC (Scanning Habitable Environments with Raman & Luminescence for Organics & Chemicals) that does not carry a regular mass spectrometer [23].

State-of-the-art MS instruments such as the ion trap and quadrupole systems do not have sufficient resolution to resolve low mass isobaric species. Orbitrap-based instruments have promising mass range and high resolution but there is limited data on the isotope ratio accuracy of fieldable Orbitrap based instruments [24, 25]. Sector instruments are preferred for isotope ratio measurements, but to achieve the large mass range of the TOF, quadrupole, and ion trap based instruments, and the resolution to resolve isobaric species, the sector instrument historically must be very large due to a throughput vs resolution tradeoff encountered during miniaturization [14]. Reducing the size and weight of a sector instrument traditionally requires either sacrificing the instrument throughput to maintain resolution or sacrificing instrument resolution to maintain throughput and sensitivity. Recently, our group has demonstrated a solution to the throughput vs resolution tradeoff in sector mass spectrometry in a cycloidal miniature mass spectrometer by applying the computational sensing technique of spatially coded apertures. Replacing the traditional exit slit of the mass analyzer with an array of slits or “coded aperture,” we achieved an order of magnitude increase in throughput without sacrificing resolution [25-30].

Currently, no flight mass spectrometer has all capabilities discussed above and summarized in section 1.1.2. Instruments based on cycloidal sector mass analyzers have the potential to achieve space flight requirements presented in Table 1. if paired with the appropriate set of technologies. These technologies include the computational sensing techniques of spatially coded apertures and super-resolution, carbon nanotube (CNT) field emission electron ionization sources, and capacitive transimpedance amplifier (CTIA) array detectors. This dissertation develops these technologies for space flight applications by improving reconstruction quality in a cycloidal mass analyzer using in spatially coded apertures, demonstrating super-resolution reconstruction in a mass spectrometer for the first time, and works towards improving CNT field emission sources. Section 1.2 provides background and a summary of previous work on cycloidal mass analyzers, ion array detectors, and spatial aperture coding. Section 1.3 introduces the research foci of this dissertation including improving reconstruction quality with spatially coded aperture, super-resolution, and CNT field emission. While the focus of this dissertation is the application of these technologies to cycloidal mass analyzers in space flight applications, these technologies are not specific to a cycloidal mass analyzer and can be implemented in different instruments as well.

Table 2: comparison of space flight mass spectrometers

Spacecraft	Instrument Acronym	Instrument Configuration	Mass Range	Weight [kg]	Power [W]	isobaric separation?	High precision isotope ratio?	Refs
Viking 1 and 2	NMS	Sector	1–49			No	No	[31]
	GCMS	Sector	12–215	25	25-140	No	No	[32]
Pioneer Venus Orbiter	ONMS	Quadrupole	1–45	3.8	12	No	No	[33]
	OIMS	Bennett RF	1-60	3	1.5	No	No	[34]
Pioneer Venus Probe	NPMS (BNMS)	Sector	1-208	11	14	No	No	[35]
Giotto	NMS	Sector	1–36			No	No	[36]
	IMS-HERS	Sector	1–64	9.2	8.5	No	No	[37]
	IMS-HIS	Sector	12–65	9.2	8.5	No	No	[37]
Galileo Probe	NMS	Quadrupole	2-150	13.2	13	No	No	[38]
Cassini Orbiter	INMS	Quadrupole	1–99	10.29	23.3	No	No	[39]
Huygens Probe (Cassini)	GCMS	GC-quadrupole	2–141	17.3	41	No	No	[40]
Deep Space 1	PEPE	TOF	1–140	5.5	9.6	No	No	[41]
Rosetta	ROSINA DFMS	Sector	12–150	16.2	19	No	No	[42]
	ROSINA RTOF	TOF	1->300	14.7	24	No	No	[42]
Philae lander	COSAC	GC-TOF	12–1500			No	No	[43]
	Ptolemy	ion trap	12-150	4.5	10	No	No	[44]
Phoenix	TEGA	Sector	0.7–140	5.7	13	No	No	[45]
MSL	SAM	GC-quadrupole	1.5-535			No	No	[46]
ExoMars	MOMA	ion trap	50-1000	11.5	82	No	No	[18]
Eurpoa Clipper	MASPEX	TOF	>1-1500	8		Yes	No	[20, 47]

1.2 Background

Cycloidal mass analyzers combined with array detectors, computational sensing techniques, and field emission electron sources have the potential to address some of the shortcomings of current space flight instruments described in section 1.1.3.

1.2.1 Cycloidal mass analyzers

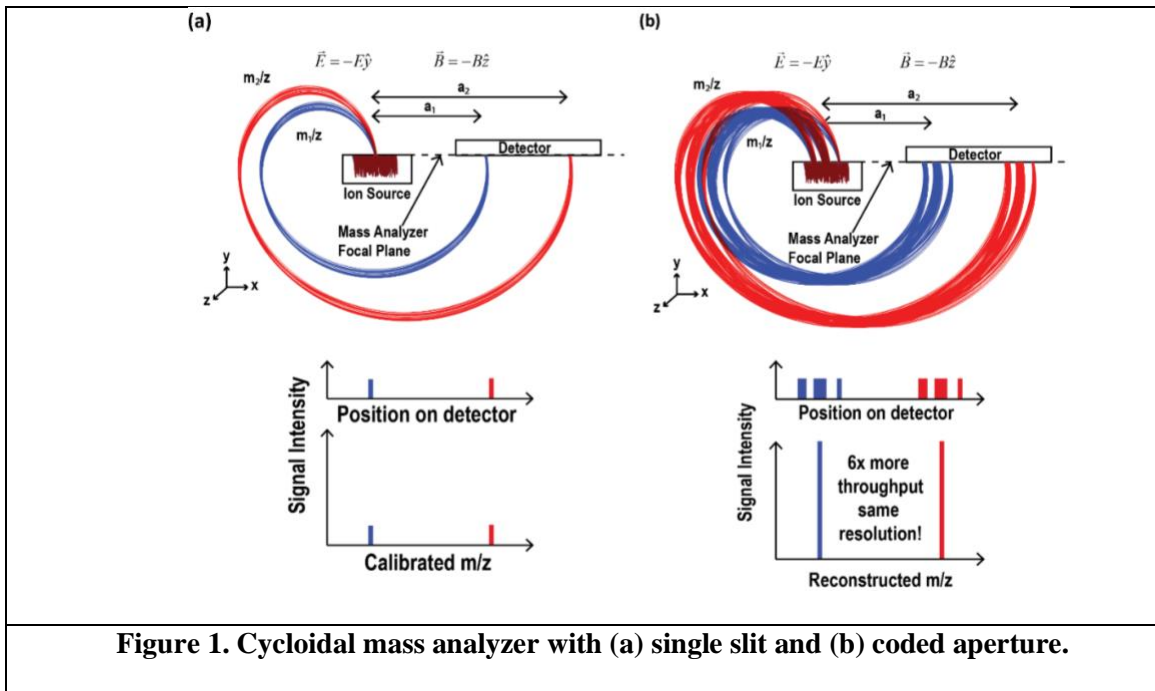
In 1938, Walker Bleakney and John A. Hipple Jr. introduced the cycloidal mass analyzer as the only sector configuration that offers perfect focusing properties [48]. In a cycloidal mass analyzer, ions are separated based on their mass-to-charge (m/z) ration due to homogenous, perpendicularly oriented magnetic and electric fields. Ions travel in a plane perpendicular to the

magnetic field and parallel to the electric field with cycloidal trajectories Figure 1.a. By definition, a cycloidal trajectory refers to the path of a point rigidly attached outside, inside or on a circle rolling on a fixed line [49]. After traveling through 360 degrees, ions of different mass-to-charge ratios are focused at different positions along the mass analyzer focal plane according to the following equation:

$$a_i = \frac{m_i}{z} \frac{2\pi E}{B^2} \quad \text{Equation 1}$$

where a_i is the distance along the focal plane measured from the ion source slit center, m_i is the ion mass, z is the ion charge, E is the electric field magnitude, and B is the magnetic field magnitude.

Note that there is a linear relationship between the focus position a and the mass to charge ratio m/z [48]. This focus position, also called the pitch, is independent of the initial velocity or energy of ions that is the main advantage of the cycloidal configuration over other double focusing sector analyzers which only offer a small correction for the initial velocity distributions [48]. Simultaneous detection of a wide mass range with a 100% duty cycle can be enabled when using an appropriate array detector placed at the cycloidal mass analyzer focal plane. These capabilities are important for analysis involving isobaric separation, high precision isotope ratios, or transient events. Details about the motion equations and movement of ions inside a cycloidal mass analyzer can be found in our previous publications [50].



1.2.2 Ion array detectors

Detectors in mass spectrometers provide information on ion abundance after mass separation inside the mass analyzer. Broadly, detectors can be categorized into focal-point detectors, which measure ions one m/z at a time, and focal-plane detectors, which simultaneously monitor ions with a range of mass to charge ratios. Focal-point detectors are typically paired with scanning mass analyzers, while focal-plane detectors are paired with mass analyzers that have a focal plane. Scanning mass analyzers are less efficient than focal plane mass analyzers because focal plane mass analyzers offer increased sensitivity due to a multiplexing advantage. Of the various detectors available, there are two main types of ion detectors including Faraday cups and electron multipliers - both can be in point or array configurations. The Faraday cup utilizes conducting electrodes to directly measure ion charge (current) [21]. Despite its simplicity, stable gain and large dynamic range, its sensitivity is compromised due to the absence of internal amplification. Electron multipliers operate through a cascade process where incoming ions

produce secondary electrons, amplifying the ion signal. However, their gain can be unstable over time, affecting precision [21]. Despite being highly sensitive, electron multiplier array detectors suffer from low dynamic range, gain drift, and are difficult to operate in a magnetic field [21, 51]. So finally, Faraday cup detectors have large dynamic range and stable gain but they are not as sensitive as electron multipliers detectors.

The detector in a cycloidal mass spectrometer for planetary exploration requires large dynamic range, gain stability, and high sensitivity for isotope ratio measurements and must be an array to enable the computational sensing techniques of spatially coded apertures and a super-resolution described below in section 1.2.3 and section 1.3.2. Also, it must be able to operate in a magnetic field. All cycloidal instruments used in this work will employ the recently developed ion detector arrays based on a capacitive transimpedance amplifier (CTIA) fabricated with CMOS technology. These CTIA arrays have a dynamic range exceeding that of a Faraday cup (10^{11}) and sensitivity approaching that of a MCP (~ 5 ion detection limit). Furthermore, these detectors have a 100% fill factor, freedom from cross-talk between pixels, programmable gain, ability to operate in a magnetic field, sensitivity to both positive and negative charge, and a variety of other desirable characteristics [30, 52].

1.2.3 Computational Sensing and spatial aperture coding

Miniaturizing conventional sector mass spectrometers has always suffered from a resolution vs throughput trade-off because as the instrument size shrinks, the slit (positioned at the exit of the ion source [53]) has to shrink to maintain the instrument resolution which reduces throughput. Breaking this trade-off was made possible by replacing the single slit with an array of slits of different sizes called coded aperture.

Spatial aperture coding is a computational sensing technique that has been previously used in Optical [54, 55] and x-ray imaging [56]. Miniaturization of sector mass spectrometers was

successful over the past few years due to the application of spatial aperture coding that eliminated the historical resolution vs throughput trade-off [27, 57-59]. The total open area of the slits determines the throughput while the width of the smallest slit on the coded aperture determines the resolution of the instrument. We successfully demonstrated the increase of throughput without sacrificing resolution in different sector mass analyzers using aperture coding; a 90° magnetic sector mass analyzer [27] [59], a Mattauch-Herzog mass analyzer [58], and a cycloidal mass analyzer [57] all coupled with a position sensitive CTIA array detector. In fact, the perfect focusing property of the cycloidal mass analyzer is ideal for the application of computational sensing techniques, spatial aperture coding, to mass spectrometry. It enables a 1:1 image projection of the coded aperture on the detector for each m/z , generating a coded spectrum for a wide range of ions as illustrated in Figure 1.b. When replacing the single slit at the exit of an ion source in a cycloidal mass analyzer with a coded aperture, a 1:1 image of the slit pattern is projected on the detector for each mass to charge ratio.

The raw data provided by the array detector when using a coded aperture is called coded spectrum that has the same image of the aperture for each m/z . However, computational reconstruction leads to a conventional spectrum with only one peak representing each m/z . Computational reconstruction starts with the estimation of the system response function using a known compound. It is mainly the aperture image projected on the detector plane for a specific compound. Then a deconvolution is applied to the coded spectrum to dissociate the system response function from the spectrum [53].

1.3 Research objectives

1.3.1 Reducing spectral reconstruction artifacts in C-CAMMS

Previous work demonstrated that aperture coding combined with a position-sensitive array detector in a miniature cycloidal mass spectrometer was successful in providing high-

throughput, high-resolution measurements as presented in section 1.2.3. However, due to poor alignment and field non-uniformities, reconstruction artifacts were present. Recently, significant progress was made in eliminating most of the reconstruction artifacts, however, using computational reconstruction, artifacts were still observed at low mass (< 17 u). In this work, the objective is to implement two methods to significantly reduce the presence of artifacts in reconstructed data. First, we will employ a variable system response function across the mass range (10 – 110 u) instead of using a fixed function. Second, we will slightly modify the design by shifting the coded aperture slits relative to the center of the ionization volume to enable even illumination of the coded aperture slits as suggested in [60].

1.3.2 Implementation of super-resolution in mass spectrometry

As mentioned in section 1.1.3, higher resolution in fieldable mass spectrometers (MS) is desirable in space flight applications to enable resolving isobaric interferences at $m/z < 60$ u such as $\text{CO} - \text{N}_2 - \text{C}_2\text{H}_4$ at $m/z = 28$ u and $\text{CO}_2 - \text{C}_3\text{H}_8$ at $m/z = 44$ u. Resolution in portable cycloidal MS coupled with array detectors could be improved by reducing the slit width and/or by reducing the width of the detector pixels. However, these solutions are expensive and can result in reduced sensitivity. In this research, one of the main objectives is to demonstrate high-resolution spectral reconstruction in a cycloidal coded aperture miniature mass spectrometer (C-CAMMS) without changing the slit or detector pixel sizes using a class of signal processing techniques called super-resolution (SR).

Super-resolution imaging (also known as sub-pixel imaging) is a signal processing technique that estimates high resolution signals from under-sampled measurements. By combining multiple sets of diverse under-sampled measurements and using knowledge of how these sets are related on a finer scale one can reconstruct a spectrum with a finer resolution. Super-resolution techniques have been used in optical and proton magnetic resonance

spectroscopy to improve the resolution beyond the pixel size of the sensor achieving between 5-16x increase in resolution [61, 62].

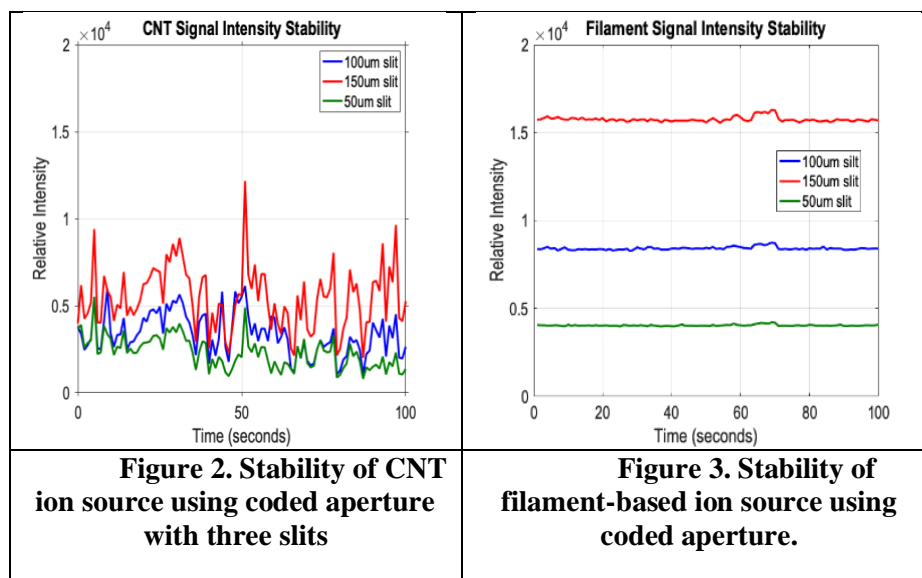
Steps to realize this objective are as follows: first develop a SR reconstruction algorithm using a sampling SR approach whereby a set of spatially shifted low-resolution measurements are reconstructed into a higher-resolution spectrum. This algorithm will be applied to experimental data collected using the C-CAMMS prototype. Second, the algorithm will be applied to synthetic data with additive noise, system response variation, and spatial shift nonuniformity to investigate experimental results, further understand the method limitations and pave the way towards improvement.

1.3.3 Field emission electron ionization

Ionization is a core element of MS. Typically electron ionization is the main method utilized in miniature MS designed for spaceflight applications through thermionic emission. A typical thermionic filament runs at 1500 K and consumes ~4W of power. Substituting thermionic emission with a field emission electron source is of a great interest for space applications because FE devices are compact and easy to integrate, consume less power and are robust to harsh environment. For instance, carbon nanotube field emission has attracted a lot of interest as a low power and low temperature replacement for thermionic filaments in electron ionization sources [63-65]. CNT field emission sources do not require any heating and consume only a few μW of power for comparable electron emission currents. Despite their potential advantages, CNT based ion sources suffer from fluctuating electron emission currents and are not as stable as thermionic filaments. Figure 2 and Figure 3 compare the stability of a CNT based electron ionization source with a coded aperture and a filament-based electron ionization source with the same coded aperture [66]. In the CNT source, not only does the signal intensity change, but the ratio of the intensities passing through each feature in the aperture code fluctuates. The reason for the

fluctuations in the CNT based ion source are two-fold. First, temporal fluctuations in the emission current from the CNTs is caused by changes in the work function due to adsorbed gases on the surface of the CNT. The work function can change by as much as 25% due to adsorbed gases on the surface of the CNTs causing a change in emitted current by an order of magnitude [67].

Second, the work function changes result in different tubes emitting across the CNT forest resulting in spatial variations in electron emission. In this research, several approaches adopted from the literature to improve the CNT field emission stability including encapsulation, patterning, and polishing will be investigated [68-70]. Furthermore, other FE based devices such as Pt nanowire arrays will be fabricated and tested to provide a stable FE electron source for spaceflight MS in case treatment fails to improve CNTs emission stability.



1.4 Dissertation outline

This research described in this dissertation is presented as follows:

Chapter 2 titled *enhancements for optimizing C-CAMMS performance* presents two methods introduced to reduce spectral reconstruction artifacts across the detectable mass range with the C-CAMMS instrument. The first method is based upon hardware design adjustments. The second method involves computational modifications.

Chapter 3 titled *a super-resolution proof of concept in a cycloidal coded aperture miniature mass spectrometer* demonstrates high-resolution spectral reconstruction in a cycloidal coded aperture miniature mass spectrometer (C-CAMMS) without changing the slit or detector pixel sizes using a class of signal processing techniques called super-resolution (SR).

Chapter 4 titled *field emission electron sources* reports work done to build a robust electron source for ionization based on field emission devices. Multiple techniques and treatments are included mainly centered around carbon nanotubes emitters and Pt nanowires emitters.

Chapter 5 summarizes scientific contributions and conclusions of the work presented in this dissertation and discusses limitations and future work orientation.

2. Enhancements for optimizing C-CAMMS reconstruction performance using spatially coded apertures

This chapter presents two strategies designed to minimize reconstruction artifacts across the entire mass range for the cycloidal coded aperture miniature mass spectrometer instrument, (C-CAMMS). This work is critical for future space flight applications which require a high level of accuracy especially when looking for precision isotope ratio measurements or separation of isobaric interferences. Therefore, eliminating any possible reconstruction artifacts caused by variations in the system response function or other hardware imperfections is critical [71]. The first approach focuses on computational modifications and the second approach involves adjustment on the coded aperture design. The introduction section 2.1 reviews previous work using spatially coded apertures and the cycloidal mass analyzer and discusses potential sources of reconstruction artifacts. The methods section 2.2 describes the implementation of both methods and the results section 2.3 presents improved reconstruction after implementing the modifications.

2.1 Introduction

Since the 1950s, spatial aperture coding has been used in optical spectroscopy to improve system throughput without sacrificing resolution [54, 72-74]. The use of spatial aperture coding entails replacing the traditional resolution-determining slit with a patterned array of slits with varying widths and computationally reconstructing the spectrum. Spatial aperture coding offers two main advantages: the Jacquinot advantage and the Fellgett advantage. The Jacquinot, or throughput advantage, is achieved because the array of slits increases the throughput of the spectrometer [75] while the Fellgett, or multiplex advantage, is achieved as the different signals from the array of slits combine to increase the signal-to-noise ratio [76]. Recently, spatial aperture coding has been applied to sector mass spectrometers in combination with position-sensitive array

detectors [53]. Similar to optical spectroscopy, spatial aperture coding in mass spectrometry consists of substituting the single slit at the exit of the ion source with an array of slits with a specific pattern. The use of aperture coding provides a solution to the historical resolution vs. throughput tradeoff in sector mass spectrometer (MS) miniaturization [57, 77]. Throughput increases of $> 10x$ without sacrificing resolution have been demonstrated using 90-degree [27, 59] and cycloidal mass analyzers [57]. Depending on the specific design required for different applications, aperture coding allows for miniaturization of the system without sacrificing resolution.

Cycloidal mass analyzers are an ideal choice for implementing spatial aperture coding due to their perfect focusing properties [50, 78]. After ions exit the ion source through the coded aperture slits, they travel in cycloidal paths towards the detector. For perfectly uniform fields, the position at which ions of a particular m/z reach the detector is linearly dependent on the m/z ratio, and a 1:1 image of the coded aperture is focused on the detector plane. As a result, computational reconstruction of the coded spectral data measured at the array detector is simplified because the coded aperture image projected across the detector plane does not exhibit distortion. Spectral reconstruction can be performed under the assumption of a shift-invariant instrument response function (system response function is constant as a function of the system parameters such as electric field, magnetic field, ion mass to charge ratio, and ion velocity), and only requires a simple deconvolution of the aperture image to reconstruct the mass spectrum [50, 53, 57, 77, 79, 80]. In contrast, 90-degree and Mattauch-Herzog mass analyzers generate a distorted image of the coded aperture at the detector plane and require a more complex reconstruction process [58]. However, reconstruction of experimental spectral data using a cycloidal mass analyzer with a shift-invariant system response can lead to reconstruction artifacts because nonidealities such as field nonuniformity, misalignment, and shallow depth of focus, can result in a system response

function that varies as a function of the system parameters [57]. Significant progress towards artifact-free reconstruction has been accomplished in the second generation cycloidal coded aperture mass spectrometer miniature prototype (C-CAMMS-MP) instrument by improving alignment between the detector and the mass analyzer focal plane, improving the electric field uniformity near the ion source, and reducing angular dispersion in the ion source [77]. However, as discussed in [77], C-CAMMS-MP still exhibits some reconstruction artifacts at low m/z due to a change in the system response below $m/z = 17$ u.

This chapter introduces two methods to achieve reconstruction with minimal artifacts over the entire mass range for the C-CAMMS-MP. The first method employs a system response function that varies as a function of m/z to perform reconstruction, similar to that used with the 90-degree sector [27, 59]. The second method is a design adjustment where the position of the slits on the S-11 coded aperture is shifted in relation to the center of the ionization volume to achieve uniform illumination of the aperture as a function of m/z . This results in a full image of the coded aperture at the detector and a reasonably uniform system response function across the entire mass range.

2.2 Methods

The data in this chapter are taken with two versions of the C-CAMMS-MP instrument as described in [77]. Both versions consist of a 0.3 T magnetic sector, an electric sector composed of 25 rectangular ring-shaped electrodes, a Neir-type electron ionization source, and a capacitive transimpedance amplifier (CTIA) array detector. The 0.3 T magnetic sector is the opposed dipole magnet described in [29]. The electric sector electrodes are arranged in an L-shaped box as displayed in Figure 4 from [77]. According to Equation 2, the electric sector electrodes are held at different potentials, where V_i is the potential on electrode i , E is the desired electric field, and $d = 84$ mm is the distance from the bottom electrode to the top electrode.

$$V_i = \left(\frac{i - 13}{25} \right) Ed \quad \text{Equation 2}$$

A printed circuit board (PCB) is attached to the outside of the electric sector which is connected to a Keithley 2636B 2-channel source measure unit. The PCB has a voltage divider comprised of 24 10 kΩ resistors placed between each electrode, allowing the application of potential gradient across the electric sector electrodes. Each channel of the Keithley 2636B supplies a voltage to one end of the voltage divider, i.e., V_1 or V_{25} . The middle electrode, 13, is held at 0 V. A Neir-type electron ionization source [81] is integrated into the center of the electric sector. It consists of a rectangular-shaped ion repeller that is positively biased to direct positive ions towards the ion source exit on the top of the ion repeller. The ion repeller has an open window on one of its short sides allowing electrons emitted by a thermionic filament to enter the ionization volume. Once ionized, ions enter the mass analyzer through an S-11 coded aperture at the exit of the ion source [53]. The aperture has three slits: 50 μm, 150 μm, and 100 μm, separated by 150 μm and 100 μm, respectively. C-CAMMS-MP uses a capacitive transimpedance amplifier (CTIA) array detector with 1704 12.5 μm-wide pixels, as described in [57]. The CTIA array detector is placed at the mass analyzer focal plane using a cavity in electrode 13 (the grounded middle electrode) on the arm of the L-shaped electric sector. The detector active area is positioned to detect ions hitting the focal plane between 10.5 mm and 31.8 mm from the ion source.

The data in Figure 4 is taken with the same instrument as described in [77]. The data in Figure 7 is taken with a version of the C-CAMMS-MP instrument with the following changes: (a) the aluminum electric sector electrodes are plated with a 12-25 μm of class 1 type V high-phosphorus nickel (10-14% Phosphorus) according to ASTM B733 followed by 0.25-0.5 μm of gold according to ASTM B488, instead of sputtered gold; (b) The ion repeller is attached with a Vespel plate positioned outside the electric sector instead of attaching the ion repeller to a PCB

inserted into the electric sector and; (c) the position of the coded aperture is shifted 500 μm relative to the centerline of the ion repeller, as shown in Figure 6.

Both versions of C-CAMMS-MP use a membrane inlet as described in [77]. The analyte consists of 100 ppm Toluene in dry air. For this study, the thermionic filament was biased at a potential of -40 V relative to the 30 V on the ion repeller to generate 70 eV electrons. The filament electron emission current was ~ 200 nA. Pressure inside the chamber was held at 2.5×10^{-5} Torr throughout the experiments. The electric field was varied from ~ 2.857 V/cm to ~ 11.905 V/cm, enabling different simultaneously detected mass ranges. For example, an electric field of 11.905 V/cm gives a mass range of 10 u to 35 u, and an electric field of 2.857 V/cm gives a mass range of 34 u to 113 u.

2.3 Results and discussion

2.3.1 Introduction

Figure 4 (a) and (b) show previously published raw coded data and spectral reconstructed data in the mass range of 10-40 u collected using C-CAMMS-MP [77]. Spectral reconstruction was performed by first using the aperture image for O_2^+ to estimate the system response function and then deconvolving the system response from the spectrum using a Lucy-Richardson deconvolution algorithm, as implemented by the *deconvlucy* function in MATLAB, with 10 iterations [82, 83]. As shown in Figure 4 (a) and (b), and discussed in [77], using the aperture image corresponding to the O_2^+ ions ($m/z = 32$ u) yields the widest m/z window, (17 to 100 u), for an artifact-free reconstruction. However, artifacts are observed below $m/z = 17$ u. These artifacts are a result of the change in the system response below $m/z = 17$ u. Figure 4 (a) illustrates this change. An ideal simulated coded spectrum (gray) is plotted behind the experimental coded spectrum (blue), showing the change from three peaks to two in the experimental data. Up to pixel number 400, or $m/z = 17$ u, all coded aperture images for different mass ratios clearly show

three peaks, as expected, because the S-11 coded aperture has three slits. However, above pixel number 400, to pixel number 1600, the coded aperture image loses the right peak corresponding to the 50 μm slit. The system response used for the reconstruction was estimated from the aperture image at $m/z = 32$ u to achieve the widest artifact free m/z window. The reconstructed data below $m/z = 17$ u has significant artifacts. Thus, while the image of the coded aperture below $m/z = 17$ u more accurately reflects the physical coded aperture, if the system response function from this low m/z region is utilized for the reconstruction, most of the spectrum (i.e., m/z between 17 u and 100 u) contains artifacts. By utilizing the system response at $m/z = 32$ u to reconstruct the spectrum, the artifacts are limited to $m/z < 17$ u. However, this approach is expected to impact the throughput (i.e., sensitivity) and possibly the resolution of the reconstructed spectrum.

The system response inconsistency with respect to m/z was primarily attributed to 1) differences in curvature of the ion trajectories as a function of m/z inside the ionization volume and 2) non-uniform electron emission causing a nonuniform illumination of the coded aperture slits due to the location of electron emission from the filament. Due to the presence of a magnetic field inside the ion source, the ion trajectories inside the ion source have a mass dependent radius of curvature, *i.e.*, the ions begin their cycloidal trajectory inside the ion source and strike the solid regions of the coded aperture instead of passing through the slits. If the electron emission is not from the center of the filament, it can exacerbate the effects of the ion curvature away from the coded aperture slits [77].

The present work described below provides two methods to decrease the artifacts, including one method that enables an image at the detector that more closely reflects the physical coded aperture for $m/z > 17$ u to further optimize performance.

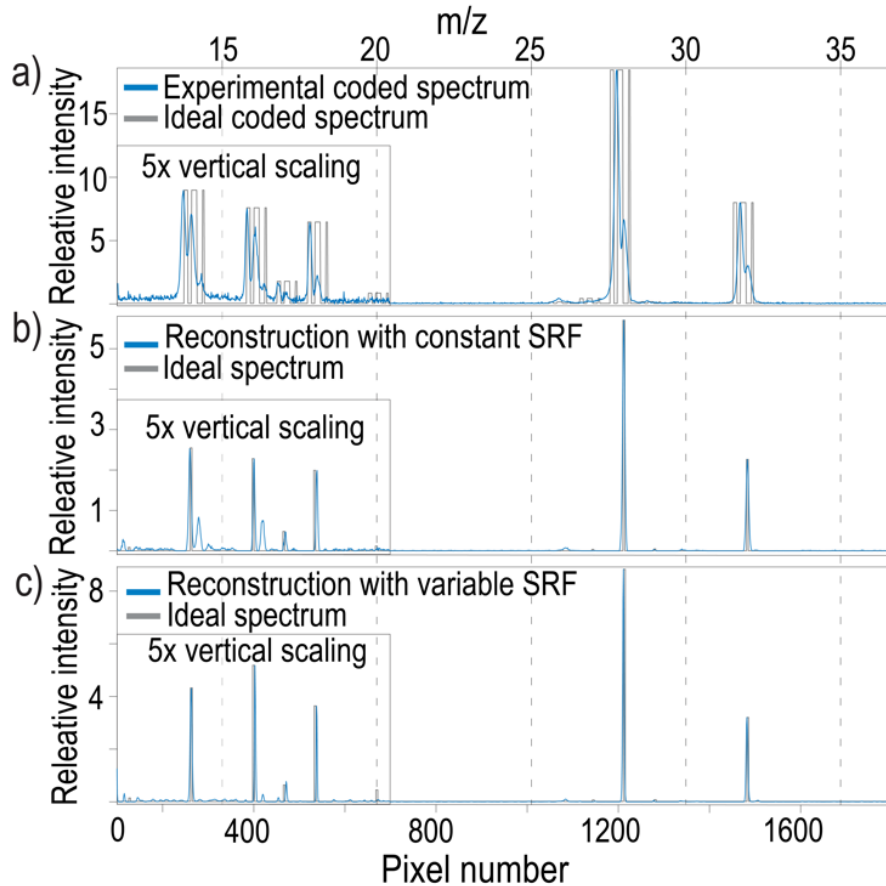


Figure 4: a) Experimental (blue) and simulated (gray) coded mass spectra of 100 ppm toluene in dry air for electric field = 1143 V/m acquired with the C-CAMMS-MP instrument. b) Reconstructed (blue) and ideal mass spectra (gray) of data displayed in (a) using MATLAB's *deconvlucy* predefined function with 10 iterations. c) reconstructed (blue) and ideal (gray) mass spectra using the new reconstruction approach considering system response variations. Experimental and simulated data from pixels 1 to 600 in ((a) and (b), and (c) are vertically scaled by a factor of 5 for better visualization. Each spectral plot is calibrated for m/z on the bottom horizontal axis, with the original pixel numbers provided on the top horizontal axis for (b) and (c). Panels (a) and (b) adapted with permission from Reference [77]. Copyright 2021, American Chemical Society.

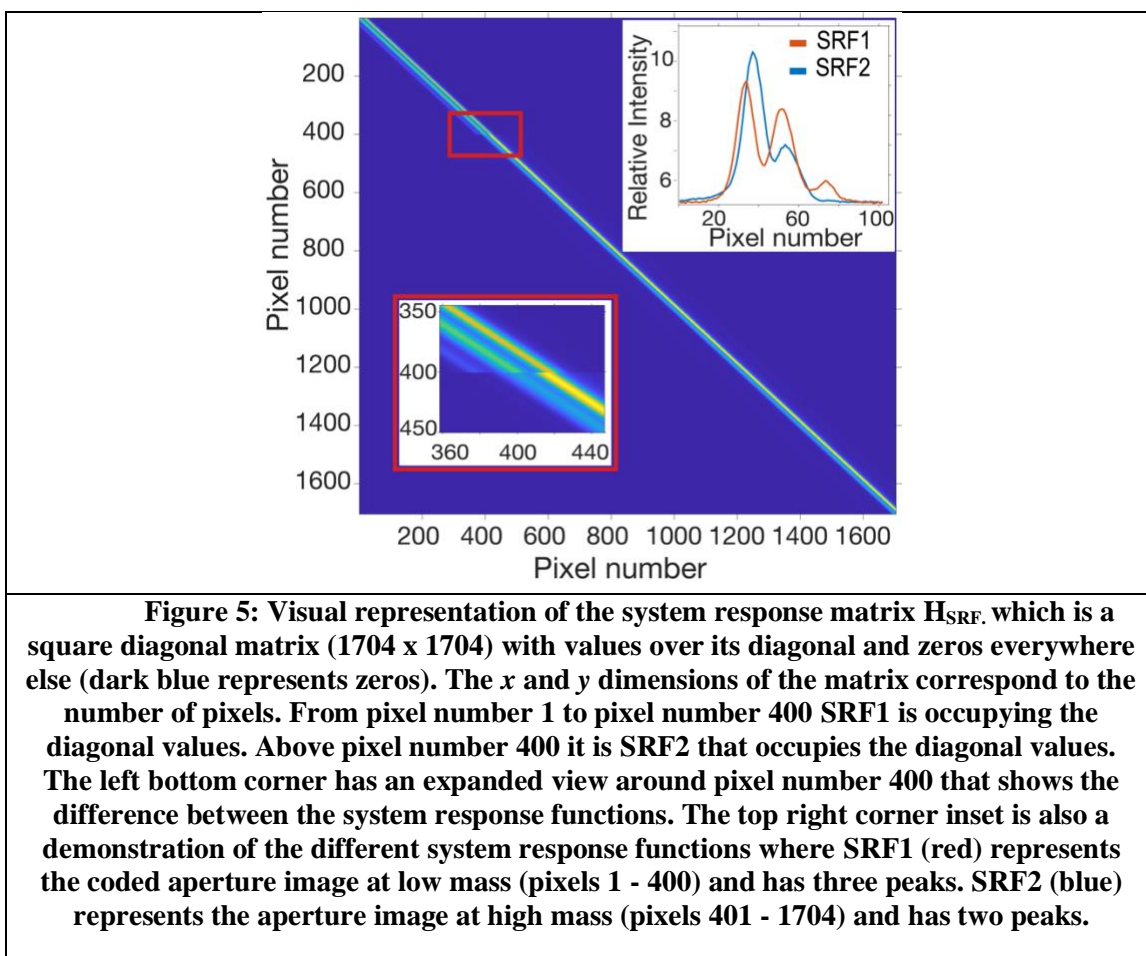
2.3.2 Reconstruction with a variable system response

The first approach to reduce artifacts incorporates system response differences for ions with $m/z > 17$ and $m/z < 17$. To execute this approach, we estimate two system response functions **SRF1** & **SRF2**. **SRF1** is the system response function for low mass (< 17 u) estimated using the peak at $m/z = 14$ from N^+ . **SRF2** corresponds to high mass (> 17 u) estimated using the O_2^+ at $m/z = 32$ u. Reconstruction is then performed as a mathematical solution to an inverse problem presented in Equation 3

$$(\mathbf{H}_{\text{SRF}} \cdot \mathbf{S}) + \mathbf{n} = \mathbf{M} \quad \text{Equation 3}$$

where \mathbf{M} is a vector containing the experimental measurement, \mathbf{S} is the ideal spectrum that we are trying to estimate, \mathbf{n} is the noise, and \mathbf{H}_{SRF} is the measurement matrix, also called the system response matrix that incorporates the physics and architecture of the instrument. \mathbf{H}_{SRF} is a square (1704 x 1704) matrix having the system response functions **SRF1** and **SRF2** across the matrix diagonal. The system response matrix \mathbf{H}_{SRF} is displayed in Figure 5 where **SRF1** occupies the diagonal values of the matrix corresponding to pixels (1 - 400) and **SRF2** occupies the rest of the diagonal values. **SRF1** and **SRF2** are both plotted on the top right corner of Figure 5 to show the variation in the coded aperture images for the different mass ranges.

Figure 4(c) shows reconstruction of the data in Figure 4(a) using the \mathbf{H}_{SRF} from Figure 5. Reconstruction using \mathbf{H}_{SRF} used a 2D implementation of the Lucy-Richardson deconvolution algorithm [27, 82, 83]. Figure 4(c) depicts reconstruction using this method of the data presented in Figure 4(a). Notice that reconstruction artifacts are significantly reduced in number and intensity (all remaining artifacts are below 6% of the peak height compared to 35% when using only one SRF) for the low mass range (< 17 u) compared to reconstruction with a constant SRF shown in Figure 4(b) which supports the utility of performing reconstruction with an m/z dependent system response matrix.



2.3.3 Reconstruction with spatially shifted coded aperture

While using an m/z dependent system response matrix enables reconstruction without artifacts, throughput is not the same for all m/z , requiring an extra step in calibration of intensities in the reconstructed spectra for quantitative analysis. Achieving uniform illumination of the coded aperture should result in a constant system response simplifying both reconstruction and spectral interpretation. To achieve uniform illumination of the coded aperture, we shifted the position of the coded aperture slits to compensate for the curvature of ions while inside the ion source caused by the magnetic field. Figure 6 shows a comparison of the ion trajectories through the coded aperture where the coded aperture slits are centered directly above the ion repeller vs. shifted

slits. A centered coded aperture does not allow higher mass ions to illuminate all three slits uniformly, as explained above, which results in a distorted aperture image for higher masses. This phenomenon is shown in Figure 6(a), where the peak corresponding to the narrowest slit of the aperture (50 μm slit) disappears from the spectrum. Figure 6(b) shows that when the slits are shifted towards the left side of the ion source, ions uniformly illuminate the coded aperture. In this case, the coded aperture image on the detector plane is representative of the S-11 geometry and constant across the entire mass range.

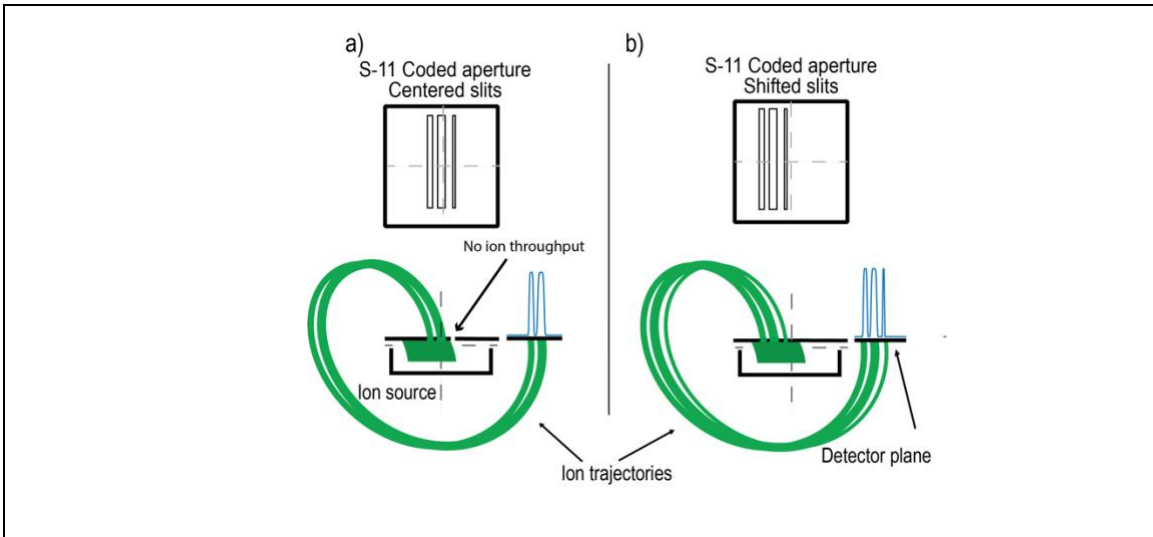
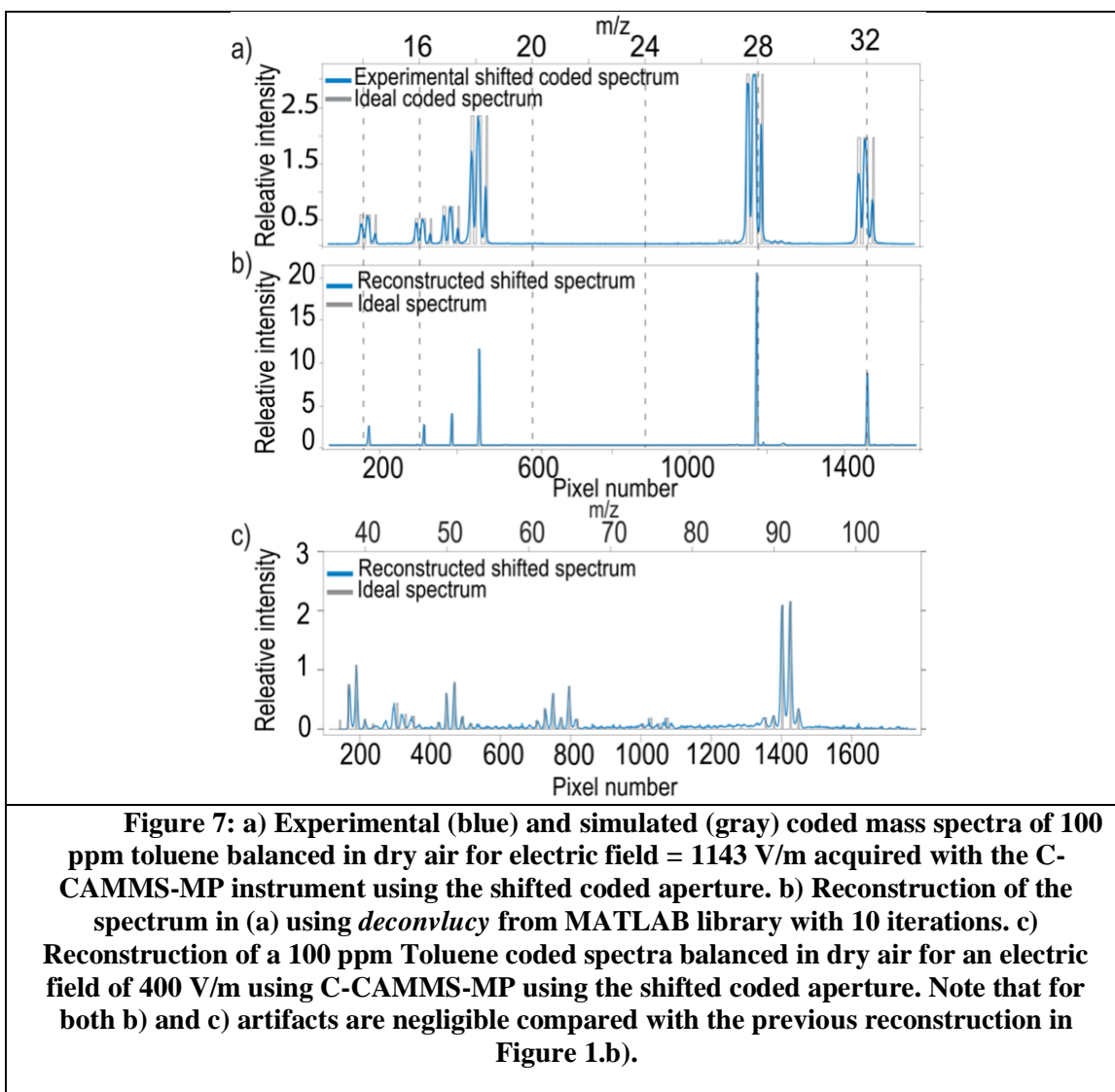


Figure 6: Schematic representation depicting the effect of shifting the coded aperture slits on the corresponding ion trajectories. a) The coded aperture slits centered directly above the ion source. The green curves represent the corresponding ion trajectories. Note that due to the curvature of the ions inside the ion source, no ions pass through the rightmost, 50 μm slit in the coded aperture, and the coded aperture image only has two peaks. b) The coded aperture slits are shifted away from the detector to the left of the ion source center. Here, ions pass through all three coded aperture slits, resulting in a coded aperture image that has three peaks of equal intensity.

Figure 7(a) shows a coded spectrum using C-CAMMS-MP with the shifted coded aperture. Note that the analyte composition did not vary between Figure 1(a) and Figure 7(a); however, it is clear that coded aperture images for $m/z = 28$ u and $m/z = 32$ u regained their third peaks after installing the shifted coded aperture slits. This result confirms the explanation of the cause behind the distortion of the coded aperture image on the detector plane for masses above 17 u. Implementing shifted coded aperture slits resulted in a more uniform system response function across the mass range and as a result, experimental spectra exhibit a consistent coded aperture image across the studied mass range, as presented in Figure 7(a).

Figure 7(b) shows reconstruction of the spectrum in Figure 7(a). The system response function for reconstruction was estimated from the O_2^+ peak at $m/z = 32$ u. Reconstruction was performed using the Lucy Richardson deconvolution as implemented in MATLAB with the *deconvlucy* function with 10 iterations. Reconstruction artifacts for low mass peaks ($m/z < 17$) in Figure 7(b) are negligible compared to those in Figure 1(b) where the system response varies due to curvature of the ions inside the ion source. Furthermore, as shown in Figure 7(c), using the shifted aperture, spectral reconstruction above $m/z = 32$ u remained free of artifacts.



2.4 Conclusion

In summary, cycloidal mass analyzers have unique focusing properties that lend themselves to facilitate reconstruction with a shift-invariant system response when used with spatially coded aperture. However, experimental cycloidal mass analyzer systems do not necessarily have a shift-invariant system response. For example, the C-CAMMS-MP prototype described previously has a system response that depends on m/z due to a mass dependent

curvature of ions in the ion source resulting in non-uniform illumination of the coded aperture [77]. This research presents two methods to reduce artifacts in the C-CAMMS-MP prototype. First, we applied an enhanced approach to estimate the system response by making the system response a function of m/z to compensate for the mass dependent curvature of the ions in the ion source. Second, we modified the S-11 coded aperture placement such that the coded aperture slits were shifted off-center above the ion source to achieve a uniform illumination of all three slits across the entire mass range. Results show a significant reduction of artifacts for both the mass range specific system response function method and the shifted coded aperture slits method. While the hardware modification is preferred as it maximizes throughput, simplifies reconstruction, and simplifies spectral calibration, both techniques can be applied to future instruments using spatially coded apertures in a cycloidal mass analyzer to limit artifacts in spectral reconstruction.

3. A Super-Resolution proof of concept in a cycloidal coded aperture miniature mass spectrometer

3.1 Introduction

Mass spectrometers (MS) are leading instruments in analytical chemistry [84]. Fieldable MS have proven useful in a variety of applications such as environmental monitoring [85-90], and airport security [91, 92]. Miniature space flight MS have also provided numerous advances in understanding of planetary science [71]. However, the resolution and sensitivity of fieldable MS is limited compared to laboratory instruments. Most fieldable MS have a resolution between 0.25 – 1 u [93]. Laboratory instruments can have resolutions of 0.001 u or better depending on the instrument configuration [94-96]. Furthermore, fieldable sector MS have a throughput vs resolution tradeoff [97]. To maintain resolution when miniaturizing a sector MS, the resolution-determining slit size at the exit of the ion source must be reduced, limiting throughput and sensitivity. Alternatively, to maintain throughput, the slit size must be increased, sacrificing resolution, and therefore the ability to differentiate between different mass-to-charge ratios (m/z). These limitations in resolution and sensitivity handicap the range of applications of fieldable MS, and fieldable sector MS in particular [97]. Spatial aperture coding is a solution to the resolution vs throughput tradeoff that was proven successful in various sector MS including a 90-degree sector [26, 27], Mattauch-Herzog [28], and cycloidal MS [30, 77].

Resolution in sector MS using a coded aperture and array detector is generally determined by the smallest slit (i.e., most narrow) in the coded aperture. Reducing slit width increases resolution. However, the smallest slit size is limited by fabrication techniques. The slit in portable sector instruments is generally fabricated using laser machining of metal foil and the slit size is limited by the aspect ratio of the hole and laser spot size. Thinner materials allow for smaller slits, but at expense of mechanical stability. Using a suitable deconvolution algorithm, the

resolution limit can be improved beyond the slit width to the width of the array detector pixel [98-100]. However, detector pixel size is also limited by fabrication techniques, and smaller detector pixels will reduce the number of ions hitting each pixel, degrading the signal to noise ratio, and increasing shot noise [98]. Therefore, ideally resolution needs to be increased without changing slit or detector pixel sizes.

In this chapter, we demonstrate super-resolution spectral reconstruction in sector MS using the C-CAMMS prototype previously built and tested [57], and a newer super-resolution cycloidal coded aperture miniature mass spectrometer (SR-CAMMS) prototype to enable increasing resolution without changing the slit or detector pixel sizes. Super-Resolution (SR) is a class of signal processing techniques used to achieve resolution beyond the native resolution of a system [98, 99, 101]. Sampling SR, where a higher resolution spectrum is reconstructed from a set of spatially shifted low-resolution measurements has been demonstrated to increase resolution up to 16x when applied in optical and proton magnetic resonance spectroscopy [99, 102]. The combination of a cycloidal mass analyzer coupled with an array detector in C-CAMMS and SR-CAMMS is an ideal system with which to apply the computational sensing techniques of aperture coding and sampling SR to maximize throughput and resolution in a miniature mass spectrometer due to the linear relationship between m/z , focus position, and electric field in cycloidal mass analyzers coupled with array detectors [78]. First, we developed a sampling SR spectral reconstruction algorithm for C-CAMMS by framing SR spectral reconstruction as a mathematical inverse problem. This SR spectral reconstruction algorithm can be applied to any spectroscopic instrument using a 1-D array detector. We then applied this reconstruction algorithm to data taken with the previously constructed C-CAMMS instrument [30, 66, 77, 103-105], demonstrating peaks with a FWHM of $\frac{3}{4}$ of a pixel with some reconstruction artifacts. To understand the origin of the reconstruction artifacts and the limitations of the SR technique, we studied the effects of

additive noise, system response variation, and spatial shift non-uniformity on reconstructions of synthetic data. Finally, we applied the SR algorithm to a new higher resolution SR-CAMMS prototype with a cooled detector that has improved system response stability and improved voltage shift uniformity.

3.2 SR problem definition and solution framework

The SR concept is summarized in Figure 8 as the combination of multiple low-resolution measurements shifted by a fraction of a pixel into a higher resolution estimation of the ideal spectrum. The following two sections frame SR as a mathematical inverse problem, and then discuss methods to solve the SR inverse problem to reconstruct a high-resolution estimate from a set of spatially shifted low-resolution measurements.

3.2.1 Super-resolution as an inverse problem

Measurements in analytical instruments with 1-D array detectors, such as a sector mass spectrometer or optical spectrometer, are related to the spectrum by Equation 4

$$(\mathbf{A} \cdot \mathbf{S}) + \mathbf{n} = \mathbf{M} \qquad \text{Equation 4}$$

where \mathbf{M} is a vector containing a measurement or set of measurements, \mathbf{S} is the ideal spectrum that we are trying to measure, \mathbf{n} is the noise, and \mathbf{A} is the system transfer matrix. The system transfer matrix \mathbf{A} incorporates the physics and architecture of the spectrometer and the measurement process, thereby mapping the input of the spectrometer to the measurements at the detector. Equation 4 is referred to as the forward problem. Making an estimate of the ideal spectrum from a measurement or set of measurements requires solving the inverse problem: knowing \mathbf{M} and \mathbf{A} , estimating \mathbf{S} . Solving this inverse problem is referred to as spectral reconstruction.

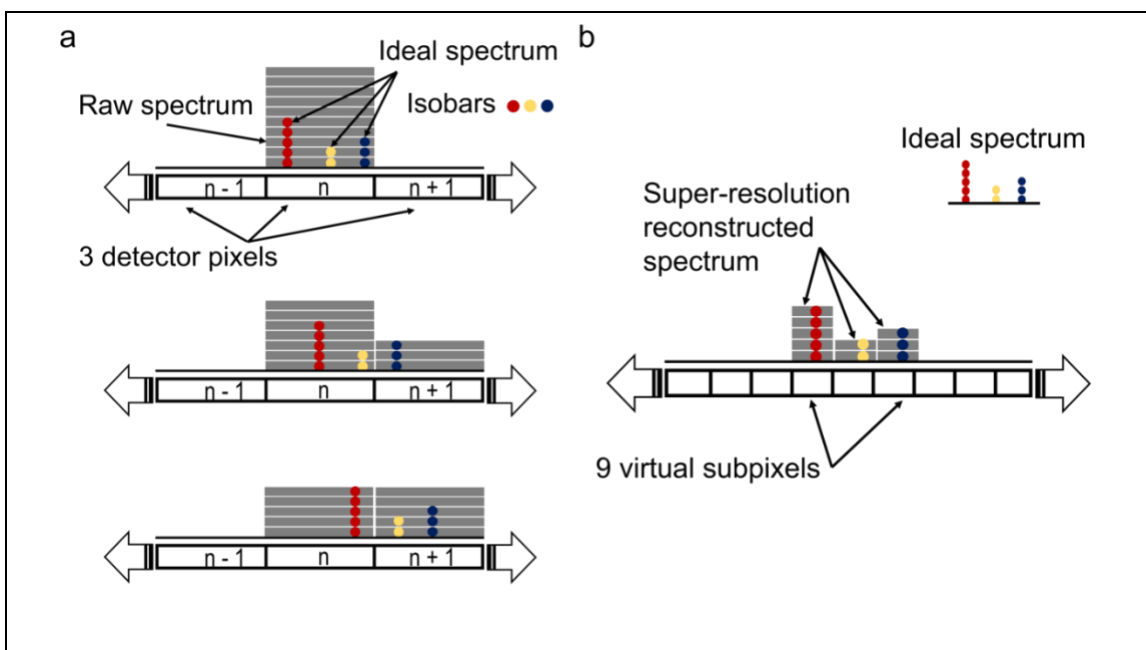


Figure 8: Schematic of super-resolution concept achieving 3x resolution improvement. a. Simulated three raw spectra shifted by a third of a pixel each. Supposing that three isobars represented by the red, yellow and blue ions of the ideal spectrum lay all at the pixel number n. Consequently, we collect a single peak from the detector. The gray bars in a stack represent the total number of ions hitting a given pixel. b. Using all three shifted raw spectra as an input to the super-resolution reconstruction method, a high-resolution spectrum can be reconstructed where all three peaks of the ideal spectrum can be visible and isobars can be resolved. Each physical pixel from the detector pixels is virtually split into three subpixels, which makes a total of 9 sub-pixels, which is responsible for the higher-resolution reconstruction.

A mass spectrum is ideally a collection of delta functions with different intensities located at different m/z . However, real spectral peaks have finite widths due to the physics and architecture of the system and the measurement process. Many sector MS instrument designs attempt to generate the ideal spectrum without needing to solve an inverse problem by placing a narrow slit at the entrance of the spectrometer. In this case, the transfer matrix \mathbf{A} is an identity matrix and the solution to the inverse problem is a simple calibration of m/z to position on the detector. However, a single narrow slit reduces the throughput and sensitivity of the instrument.

In an instrument with a coded aperture like C-CAMMS [26, 27], the transfer matrix \mathbf{A} contains off-diagonal elements representative of multiplexing. In a cycloidal mass analyzer like the one used in C-CAMMS, the unique perfect focusing properties produce a 1:1 image of the coded aperture at the detector plane. As a result, the transfer matrix \mathbf{A} is a Toeplitz matrix having the system response function (**SRF**), essentially the image of the coded aperture, across the matrix diagonal. In this case we refer to the matrix \mathbf{A} as the system response matrix, \mathbf{H}_{SRF} and a reasonable estimate for the solution to the inverse problem can be obtained from a simple deconvolution of the coded aperture image from the measurement [60]. In other mass spectrometer configurations like the 90-degree sector and the Mattauch-Herzog with a coded aperture, the \mathbf{H}_{SRF} is not a Toeplitz matrix, requiring a more complex process to solve the inverse problem [28, 106].

In SR, where multiple subpixel shifted measurements are collected (Figure 8), the transfer matrix \mathbf{A} is a combination of a system response matrix \mathbf{H}_{SRF} , and a shifting matrix representing the subpixel shifts, $\mathbf{H}_{\text{shift}}$. A model of the SR forward problem is summarized in a block diagram, Figure 9. Consider a 1-D planar array detector having p physical pixels of width w , and an ideal spectrum \mathbf{S} as the input to the instrument. SR computationally divides each pixel of the p detector physical pixels into q virtual subpixels resulting, after reconstruction, in an estimated high-resolution spectrum $\hat{\mathbf{S}}$ having a total number of pixels ($p \times q$). Enabling this high-resolution reconstruction requires acquiring q low-resolution measurements \mathbf{m}_1 to \mathbf{m}_q which are spatially shifted from one another by w/q . For each low-resolution measurement \mathbf{m}_i the ideal spectrum is altered by the instrument response \mathbf{H}_{IRF} and the noise \mathbf{n} . The shifting matrix $\mathbf{H}_{\text{shift}}$ is a square $(p \times q) \times (p \times q)$ sparse matrix that mathematically represents the multiple low-resolution spectra \mathbf{m}_i spatial shifts. Then, all q low-resolution measurements are organized into a single measurements vector \mathbf{M} . Finally, Equation 4, can be rewritten to fully summarize the

mathematical formulation of the SR forward problem where \mathbf{n} represents random additive noise and \mathbf{A} is the transfer matrix resulting from the multiplication of $\mathbf{H}_{\text{shift}}$ by \mathbf{H}_{IRF} (Equation 5).

Solving the inverse problem of Equation 5 enables an estimate $\hat{\mathbf{S}}$ of the ideal spectrum \mathbf{S} .

$$(\mathbf{A} \cdot \mathbf{S}) + \mathbf{n} = (\mathbf{H}_{\text{Shift}} \cdot \mathbf{H}_{\text{IRF}} \cdot \mathbf{S}) + \mathbf{n} = \mathbf{M} \quad \text{Equation 5}$$

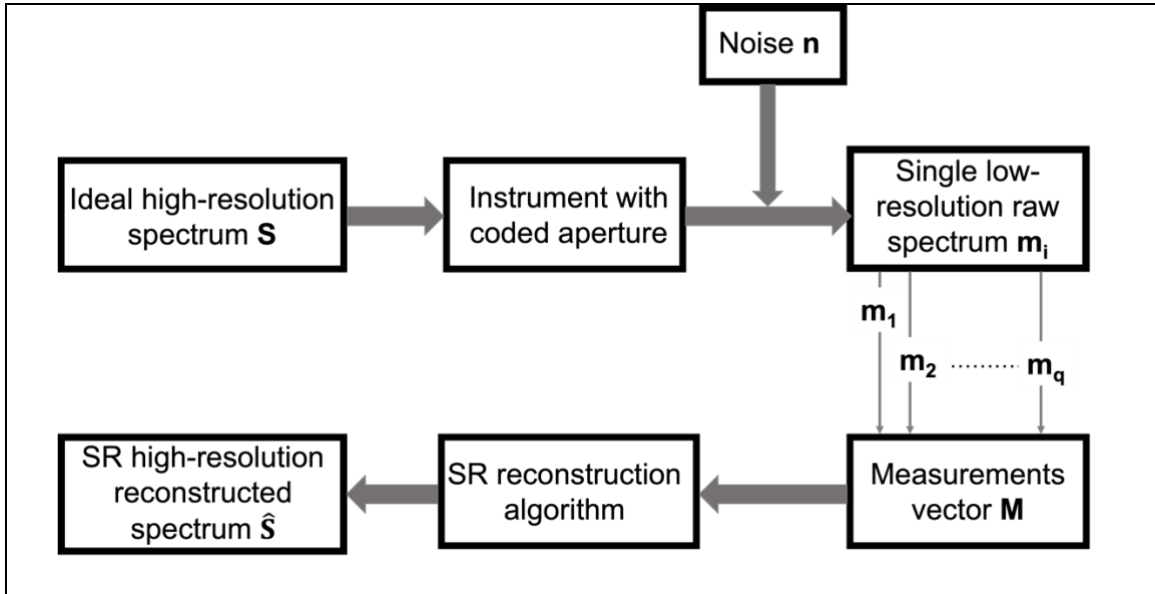


Figure 9. Super-resolution reconstruction steps simplified diagram. We consider an ideal high-resolution spectrum \mathbf{S} as the input to the instrument (mass analyzer). In order to reconstruct a high-resolution estimation of \mathbf{S} , we collect q shifted spectra m_1 to m_q that will be organized into a measurement vector \mathbf{M} . The latter is the input to the SR reconstruction algorithm to finally produce a high-resolution estimation of \mathbf{S} , $\hat{\mathbf{S}}$.

3.2.2 SR reconstruction: solving the SR inverse problem

Several approaches can be used to reconstruct subpixel shifted spectra into a higher resolution estimate of the actual spectrum. Section 3.2.2.1 reviews previous approaches to SR spectral reconstruction with a 1-D array detector and provides justification for framing SR reconstruction with C-CAMMS as an inverse problem. Section 3.2.2.2 presents the characteristics of the SR transfer matrix \mathbf{A} of Equation 5, establishing the need for regularized numerical

methods to solve the SR inverse problem. Finally, section 3.2.2.3 introduces the regularized numerical methods used in this chapter to solve the SR inverse problem.

3.2.2.1 Previous work on SR with a 1-D array detector

As mentioned in the introduction, SR has been used in signal processing, optical imaging, and spectroscopy [107, 108]. SR was implemented in optical spectroscopy with a 1-D detector using a dithering technique [107-109] where the high-resolution spectral reconstruction does not rely on solving an inverse problem. In the dithering technique, the measurements are organized per pixel instead of per shifted measurement as described above. The dithering technique also assumes that reconstruction error (difference between the estimate of the ideal spectrum and the ideal spectrum) is periodic [107-109]. Based on this assumption, the reconstruction error is then eliminated using a low-pass filter. However, experimental measurements do not generally have periodic error due to random white noise. Furthermore, frequency domain low-pass filtering may not be suitable when trying to recover isobars and/or isotopes with large differences in relative intensity because of potential loss of information in the filtered noise. Finally, when working with a system that employs a coded aperture instead of a single slit, SR reconstruction using the dithering technique requires an extra step of deconvolution of the coded aperture image from the filtered result that could potentially add numerical error into the reconstructed estimate. Therefore, for this chapter, we have decided to pursue a SR reconstruction using an inverse problem approach.

3.2.2.2 Characteristics of the SR transfer matrix

In general, approaches to solving an inverse problem such as that in Equation 5 are determined by the properties of the transfer matrix \mathbf{A} [110]. Multiple solving techniques have been developed depending on whether the inverse problem is well-posed or ill-posed. A linear problem is well-posed according to Hadamard's definition when its solution satisfies three

conditions: 1) existence, 2) uniqueness, and 3) stability [111]. While existence and uniqueness can easily be satisfied, stability usually fails to be satisfied because, depending on the properties of the transfer matrix \mathbf{A} , a small perturbation in the measurements vector \mathbf{M} can translate into large perturbations in the estimate, $\hat{\mathbf{S}}$ [112]. For example, Equation 5 can be rewritten by representing the measurements vector \mathbf{M} as the sum of an exact measurements vector $\mathbf{M}_{\text{exact}}$ plus noise (Equation 6).

$$\mathbf{A} \cdot \mathbf{S} = \mathbf{M}_{\text{exact}} + \mathbf{n} = \mathbf{M} \quad \text{Equation 6}$$

Using Equation 6, the estimate of the ideal spectrum $\hat{\mathbf{S}}$, can then be expressed as the sum of the inverse of \mathbf{A} times the exact measurements vector plus the inverse of \mathbf{A} times the noise (Equation 7). Furthermore, since the inverse of \mathbf{A} times the exact measurements vector is the ideal spectrum, \mathbf{S} , $\hat{\mathbf{S}}$ is the ideal spectrum plus the inverse of \mathbf{A} times the noise (Equation 7).

$$\hat{\mathbf{S}} = \mathbf{A}^{-1} \cdot \mathbf{M}_{\text{exact}} + \mathbf{A}^{-1} \cdot \mathbf{n} = \mathbf{S} + \mathbf{A}^{-1} \cdot \mathbf{n} \quad \text{Equation 7}$$

Using Equation 7, the norm of the error between exact solution \mathbf{S} and approximated solution $\hat{\mathbf{S}}$ can be written as:

$$\|\hat{\mathbf{S}} - \mathbf{S}\| = \|\mathbf{A}^{-1} \cdot \mathbf{n}\| \leq \|\mathbf{A}^{-1}\| \|\mathbf{n}\| \quad \text{Equation 8}$$

Furthermore, from Equation 6, the norm of an exact measurements vector is less than or equal to the norm of \mathbf{A} multiplied by the norm of \mathbf{S} (Equation 9)

$$\|\mathbf{M}_{\text{exact}}\| \leq \|\mathbf{A}\| \|\mathbf{S}\| \quad \text{Equation 9}$$

Combining Equation 8 and Equation 9, Equation 10 expresses the relative error between the exact solution \mathbf{S} and the estimated solution $\hat{\mathbf{S}}$ as a function of the condition number of the matrix \mathbf{A} , $K(\mathbf{A}) = \|\mathbf{A}\| \|\mathbf{A}^{-1}\|$.

$$\frac{\|\hat{\mathbf{S}} - \mathbf{S}\|}{\|\mathbf{S}\|} \leq \|\mathbf{A}\| \|\mathbf{A}^{-1}\| \frac{\|\mathbf{n}\|}{\|\mathbf{M}_{\text{exact}}\|} = K(\mathbf{A}) \frac{\|\mathbf{n}\|}{\|\mathbf{M}_{\text{exact}}\|} \quad \text{Equation 10}$$

Therefore, for $\hat{\mathbf{S}}$ to be a good estimation of \mathbf{S} , the norm of the error must be small and the right-hand side term of the inequality of Equation 10 has to be small. $K(\mathbf{A})$ can be calculated by dividing the largest singular value by the smallest singular value of the singular values decomposition of \mathbf{A} . In the case of a large condition number ($\gg 1$), meaning that \mathbf{A} is ill-conditioned, the error norm is not bound and the solution to this inverse problem is unstable. For the transfer matrix \mathbf{A} in SR that combines a shifting matrix and system response matrix, the condition number is $\gg 1$. Thus, to process the inversion for SR, a numerical regularization method is required such that a small change in \mathbf{M} does not cause a large relative error in $\hat{\mathbf{S}}$ [113].

3.2.2.3 SR reconstruction approach used in this research

To solve Equation 5, numerical regularized methods are required because of the ill-posed nature of our inverse problem [114-116]. In this chapter, we chose to estimate the solution to the inverse problem using least squares (LS) minimization. (Equation 11) [117]:

$$\min (\|\mathbf{A} \cdot \hat{\mathbf{S}} - \mathbf{M}\|^2) \quad \text{Equation 11}$$

Several methods including Pseudo-inverse [113], Tikhonov regularization [118], and iterative methods such as non-negative least squares (NNLS) [119] and iterative conjugate gradient non-negative least squares (CGLS) [120] can be used to solve this LS minimization problem. The following paragraphs briefly describe these methods and justify our choice of NNLS and CGLS for the SR inverse problem.

The Pseudo-inverse of \mathbf{A} provides an optimal solution ($\hat{\mathbf{S}}_{\text{pseudo}}$) to this LS problem (Equation 12).

$$\hat{\mathbf{S}}_{\text{pseudo}} = ((\mathbf{A}^T \cdot \mathbf{A})^{-1} \cdot \mathbf{A}^T \cdot \mathbf{M}) \quad \text{Equation 12}$$

This solution is considered optimal because it is an unbiased solution. However, this solution is very unstable due to the ill-posedness, making the Pseudo-inverse solution useless in practice [121]. Introducing bias into the solution can compensate for the ill-posedness of the inverse problem. In this case, the minimization LS problem in Equation 11 becomes Equation 13 [122]:

$$\min (\| \mathbf{A} \cdot \hat{\mathbf{S}} - \mathbf{M} \|^2 + \| \mathbf{L} \cdot \hat{\mathbf{S}} \|^2) \quad \text{Equation 13}$$

where \mathbf{L} is a regularizer matrix. Often, $\mathbf{L} = \lambda \mathbf{I}$, where \mathbf{I} is the identity matrix, and λ is the regularization parameter. Using Equation 13, the regularized solution ($\hat{\mathbf{S}}_{\text{reg}}$) can be written as:

$$\hat{\mathbf{S}}_{\text{reg}} = (\mathbf{A}^T \cdot \mathbf{A} + \lambda^2 \mathbf{I})^{-1} \cdot \mathbf{A}^T \cdot \mathbf{M} \quad \text{Equation 14}$$

The choice of \mathbf{L} depends on the algorithm used to solve the inverse problem. The Tikhonov algorithm, a widely used method to solve inverse problems, solves for $\hat{\mathbf{S}}_{\text{reg}}$ [117, 123] by finding an optimum regularization parameter λ . One method to find an optimum λ is to plot an L-curve, or norm of the error as the difference between the estimated solution and the exact solution versus the regularization parameter λ [124]. The optimum λ gives the smallest error norm, usually it is positioned at the corner of the L-curve. However, in many cases, including that of SR with C-CAMMS, the L-curve does not have an ‘L’ shape making the choice of λ prohibitively difficult. Additional limitations of the L-curve method are discussed in reference [125]. Finally, Tikhonov-like methods compensate for the ill-posedness of the problem by introducing a small bias that sanctions small singular values, since values close to zero are responsible for the ill-posedness. So, penalizing them seems to be a reasonable approach to solution. Nevertheless, important information can be buried in these small values.

Iterative methods such as NNLS and CGLS offer an advantage over Tikhonov-like methods because they do not sanction small singular values. Instead, they apply an iterative method directly on the $\| \mathbf{A} \cdot \hat{\mathbf{S}} - \mathbf{M} \|^2$ term of Equation 11, terminating the iterations when semi-convergence is achieved, but before reaching asymptotic convergence to an unbiased, but

unstable, LS solution. In these iterative methods (NNLS, CGLS), the iteration number plays the role of the regularization parameter. In this chapter we use both NNLS and CGLS, although many different methods could be used [113, 119, 121, 122]. The NNLS algorithm [119] assumes that the data has white additive noise and that the solution to the problem must be non-negative. To realize this solving method, a built-in MATLAB function that implements the algorithm described in ref. [119] was used. The NNLS method can be sensitive to the problem size. However, for the experimental data presented in this chapter, problem size is not an issue because our problem is considered relatively small. The second method explored is an iterative Conjugate Gradient nonnegative Least Squares algorithm (CGLS) [120, 126]. This method provides an iterative flexible conjugate gradient least squares solution after semi-convergence is achieved as described in ref. [126], meaning that iterations end when a “good” approximation is reached before the noise significantly distorts the solution. The underlying assumptions of this method are that the input data is assumed to have white Gaussian noise and that the provided solution must be non-negative. The algorithm is based upon the `IRnnfcgls` function from IR toolbox described in ref. [126]. This method is mostly used for very large problems (2D & 3D problems). Both NNLS and CGLS are used as an independent check on the results, and to generalize the method for larger problem sizes if needed in the future. However, only NNLS results will be shown in the results section as NNLS and CGLS results are similar. CGLS results are shown in Figure 34, Figure 35, Figure 36, and Figure 37 in appendix A.

3.3 Results and discussion

3.3.1 Experimental results using C-CAMMS

To test the SR reconstruction algorithm presented above, we used a cycloidal coded aperture miniature mass spectrometer (C-CAMMS) [60], acquired measurements with a $\frac{1}{2}$ pixel shift to generate a super-resolution spectral reconstruction near $m/z = 28$ u, and compared the

FWHM at $m/z = 28$ u of the super-resolution spectrum with a low-resolution reconstruction obtained by deconvolving the aperture image from the coded spectrum.

The C-CAMMS instrument used is the same as that described in [60], with a few minor changes. Briefly, C-CAMMS consists of a 0.3 T opposed dipole permanent magnet magnetic sector [29], with an electric sector composed of 25 rectangular ring-shaped electrodes arranged in an L-shaped box. Each electrode is held at a different potential according to Equation 15 where V_i is the potential on electrode i , E is the desired electric field, and $d = 84$ mm is the distance from the bottom electrode to the top electrode.

$$V_i = \left(\frac{i - 13}{25} \right) Ed \quad \text{Equation 15}$$

The potentials are applied using a voltage divider consisting of 24 10 k Ω resistors placed between each electrode using a PC Board attached to the electric sector and connected to a Keithley 2636B 2 channel source measure unit. One channel of the Keithley 2636B supplies the voltage V_1 to one end of the voltage divider, while the other channel of the Keithley 2636B supplies the voltage V_{25} to the other end of the voltage divider. The middle electrode 13 is held at 0 V. A capacitive transimpedance amplifier (CTIA) array detector with 1704 12.5 μm wide pixels is placed in a cavity in the grounded middle electrode (electrode 13) at the corner of the L-shaped box, extending between 10.5 and 31.8 mm from the ion source coded aperture center. The ion source in C-CAMMS is a Neir-type electron ionization source [81] integrated into the geometric center of the electric sector and contains an S-11 coded aperture [53] with slits of 50 μm , 150 μm , and 100 μm that are separated by 150 μm and 100 μm , respectively. Key differences between the C-CAMMS instrument used here and that described in [60] include: (i) plating the aluminum electric sector electrodes in gold with a high-phosphorus nickel adhesion layer instead of sputtering with gold, (ii) a 500 μm shift of the coded aperture above the ion repeller as suggested by [60] to improve coded aperture imaging, and (iii) attachment of the ion repeller inside the ion

source with a vespel plate positioned outside the electric sector instead of attaching the ion repeller to a PC Board inserted into the electric sector. For the experimental data described here, we measured lab air at a pressure of 2.5×10^{-5} Torr using a membrane inlet as described in [60]. The thermionic filament was biased at a potential of -40 V relative to the 30 V on the ion repeller to generate 70 eV electrons. The filament electron emission current was ~200 nA.

SR requires a set of spatially shifted spectral measurements. In a cycloidal mass analyzer a set of spatially shifted measurements can be realized by adjusting electric and/or magnetic fields according to Equation 16 that describes the positions a_k that ions of mass to charge ratio m_k/z_k hit the detector plane relative to the ion source exit, where E is the electric field and B is the magnetic field [103].

$$a_k = \frac{2\pi E}{B^2} \frac{m_k}{z_k} \quad \text{Equation 16}$$

Since C-CAMMS employs a permanent magnet-based magnetic field, we adjust the electric field to produce a set of spatially shifted spectral measurements. The electric field can be adjusted by changing the negative and positive voltages V_1 and V_{25} applied to the voltage divider with the Keithley 2636B. To calculate the change in voltage needed to achieve a sub-pixel shift in position, we differentiate Equations 12 and 13 with respect to E , and combined them, solving for the change in voltage, ΔV_i . The result in Equation 17, where Δa is the shift distance, indicates that the calculation depends on the m_k where the resolution is to be increased. Therefore, analyzing super-resolution data with C-CAMMS requires focusing on a small range of m/z , rather than the whole spectrum.

$$\Delta V_i = \frac{\Delta a z_k B^2 d}{m_k 2\pi} \left(\frac{i - 13}{25} \right) \quad \text{Equation 17}$$

For this proof-of-concept data with C-CAMMS, we chose to look at $m/z = 28$ u for N_2^+ ions. In C-CAMMS, using an electric field $E = 833.3$ V/m ($V_1 = -35$ V, and $V_{25} = +35$ V), $m/z = 28$ u will hit the detector at $a = 16.9$ mm (Equation 16). In the voltage range of ± 20 -200 V, the Keithley 2636B has a programming resolution of 5 mV, an accuracy of 0.02% of the reading + 50 mV, or ± 58 mV, and a typical noise of ± 2 mV. For a $\frac{1}{2}$ pixel shift, ($\Delta a = 6.25$ μm), which theoretically should produce peaks with a FWHM of $\frac{1}{2}$ pixel, or 6.25 μm after reconstruction, Equation 17 indicates a voltage shift of 12.4 mV is required, which is at the limit of the Keithley 2636B capabilities. Therefore, we took several measurements with a 10 mV shift, plotted the data, and used peak fitting to choose a set of measurements with the required $\frac{1}{2}$ pixel shift. After shifted data acquisition, data are trimmed to focus on the N_2^+ and O_2^+ peaks of the mass spectrum (using 350 pixels out of the 1704 detector pixels) and arranged into a measurements vector as described in Figure 9.

Figure 10 compares a raw coded spectrum, a low-resolution estimate of the spectrum obtained by deconvolution of the aperture image, and a SR reconstruction using the shifted measurements and a NNLS reconstruction method. An ideal coded spectrum is also displayed in gray behind the raw coded spectrum that represents perfect mapping of the S-11 coded aperture on the detector using air data from the NIST Chemistry WebBook [127]. Note that the ideal coded spectrum does not perfectly match the raw coded spectrum, which can be explained by nonuniformity of the electrical and magnetic fields [53, 57, 60, 66]. For the low-resolution reconstruction, we followed the procedure in Vyas et al. [60] by first using the aperture image for O_2^+ ion to estimate the system response, and then deconvolving the system response from the spectrum using the Lucy-Richardson deconvolution algorithm with 10 iterations [82, 83]. For the SR reconstruction, the \mathbf{H}_{SRF} was generated by estimating the system response using the aperture image at O_2^+ and placing it along the diagonal of the matrix, and the $\mathbf{H}_{\text{shift}}$ matrix assumes an

exactly $\frac{1}{2}$ pixel shift. For the low-resolution reconstruction, Figure 10 b) shows that the FWHM of N_2^+ peak is 5 pixels (equivalent to $62.5 \mu\text{m}$ or 0.088 u) with no reconstruction artifacts, similar to our previous work [30, 60]. Increasing the number of iterations in the Lucy-Richardson deconvolution algorithm, 100 iterations for example, reduces the peak width to $27.5 \mu\text{m}$, close to the width of 2 pixels. However, increasing the number of iterations to more than 10 in the Lucy-Richardson algorithm generates a significant number of artifacts as shown in Figure 38 of appendix A. Combining the two $\frac{1}{2}$ pixel shifted measurements with the SR algorithm yields a FWHM for the N_2^+ peak of 1.5 subpixels (equivalent to $9.3 \mu\text{m}$, or 0.013 u). A 1.5 subpixel FWHM is equivalent to $\frac{3}{4}$ of a pixel, validating the ability of SR reconstruction algorithm as presented in section 3.2 to achieve subpixel resolution, and is 6.6 x narrower than FWHM of the same peak when reconstructed using the deconvolution algorithm used in our previous work [82, 83]. Note, as described above, the applied voltage shift is specific to the N_2^+ peak and will not be applicable to the entire mass spectrum. For O_2^+ , the required voltage change for $\frac{1}{2}$ pixel shift is 10.9 mV . The FWHM for O_2^+ after SR reconstruction is similar to that of N_2^+ . Based on results presented in the synthetic data section on uncertainty in the sub-pixel shift, the difference in shift required for N_2^+ and O_2^+ is not significant, so the resolution improvement observed for O_2^+ is also valid.

While we observe a significant improvement in resolution using the SR technique, low intensity (up to 20% of the N_2^+ peak height) reconstruction artifacts are observed to the right and left of the N_2^+ peak in Figure 10 c), while no artifacts are observed for O_2^+ . Three factors that could result in these artifacts are the presence of noise in the measurements, error in estimation of the system response function, and uncertainty in the amount of shift between the measurements. As shown in Section 3.2.2.2, and Equation 8, noise introduces error in the estimation of the ideal spectrum. Furthermore, this reconstruction algorithm assumes that the system response is shift

invariant across the detector. For an ideal cycloidal mass analyzer with perfectly uniform fields, the system response will be shift invariant. However, C-CAMMS has both electric and magnetic field inhomogeneities, which could result in small changes in the system response as a function of m/z and result in reconstruction artifacts. It is likely that no artifacts are observed for O_2^+ because the aperture image for O_2^+ was used to generate \mathbf{H}_{SRF} . Finally, as discussed above, the $\frac{1}{2}$ pixel shift used requires a voltage change near the limit of the Keithley 2636B capabilities and peak fitting was used to choose measurements with the desired $\frac{1}{2}$ pixel shift. Uncertainty in the amount of shift could result in reconstruction artifacts.

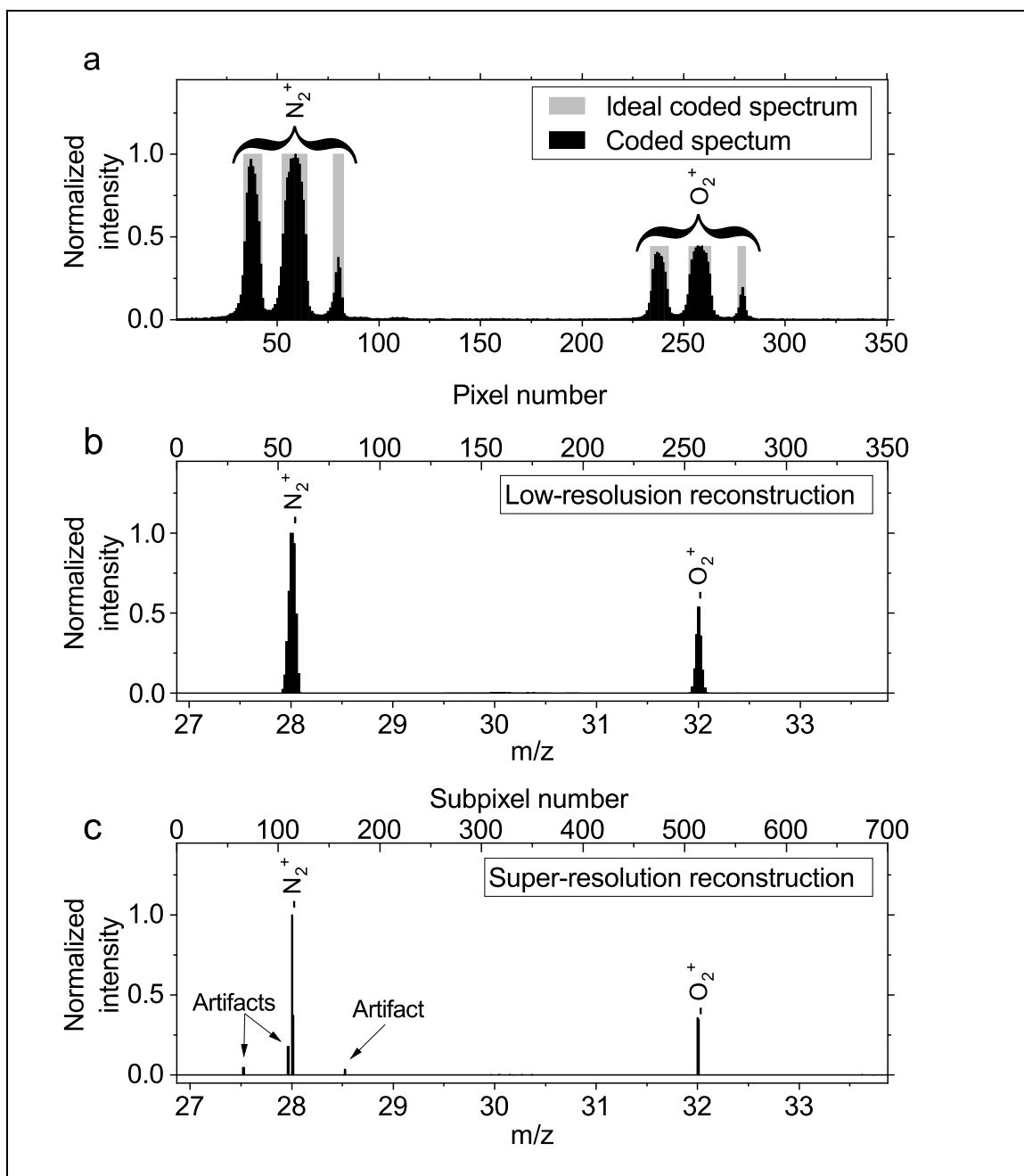


Figure 10. a. Coded mass spectrum of air. For ions of each m/z , a sequence of 3 peaks appears at the detector. b. Richardson-Lucy low-resolution reconstruction. Here the image of the coded aperture is deconvolved from the spectrum, increasing throughput, but maintaining the resolution of the smallest feature in the coded aperture. No sub-pixel shifting is involved. c. Non-negative least squares super-resolution reconstruction incorporating a $\frac{1}{2}$ pixel shift. Small reconstruction artifacts are observed to the right and left of the N_2^+ peak.

3.3.2 Synthetic study using simulated spectra

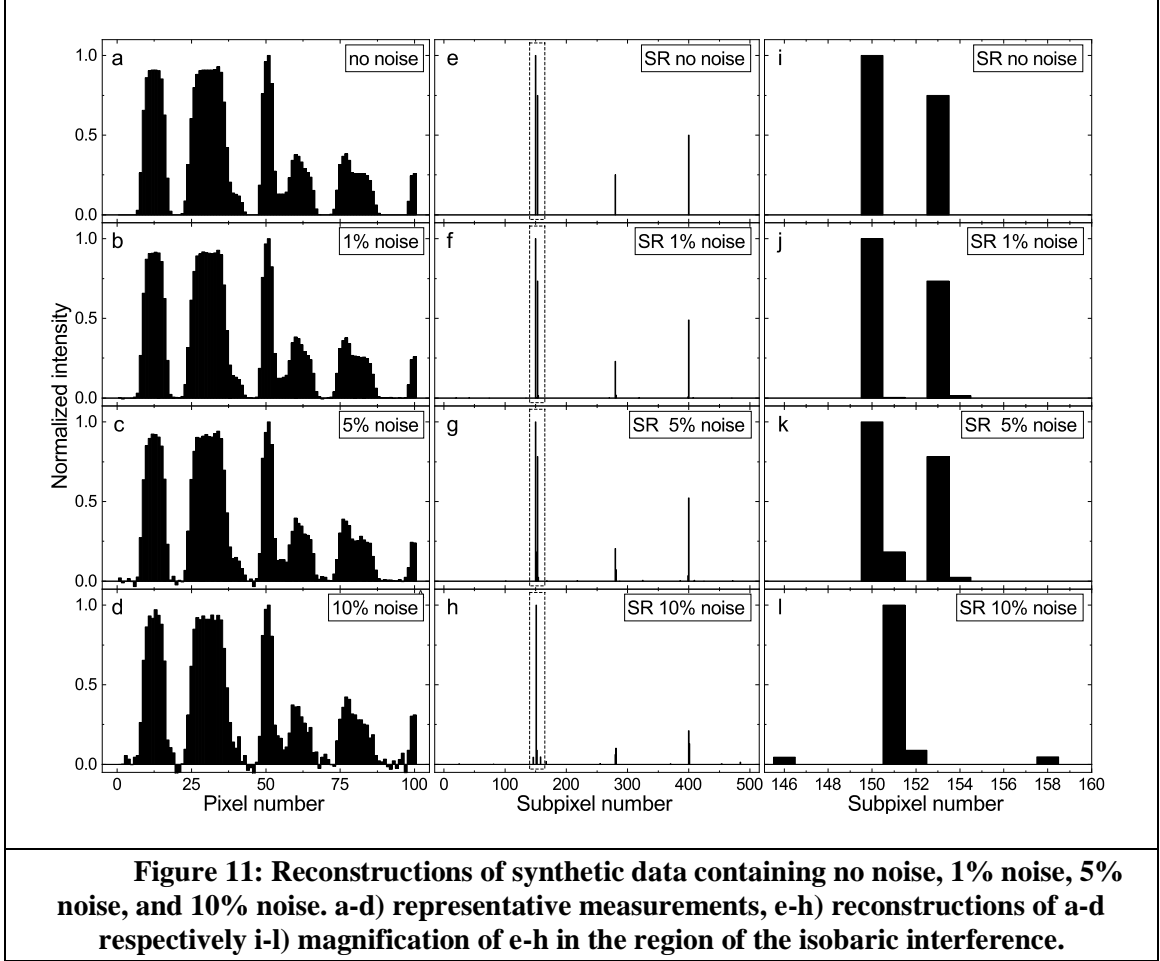
This section presents a study of the effects of noise, uncertainty in the spectral shift, and system response variation on the quality of SR reconstruction using synthetic data to further investigate the origin of the reconstruction artifacts in experimental results and investigate the potential limitations of the SR reconstruction algorithm used in this work. The synthetic study steps are summarized in Figure 39 of appendix A.

To study the effects of noise, uncertainty in the spectral shift, and system response variation on the quality of reconstruction, we start with a target ideal spectrum \mathbf{S} , an unperturbed system response matrix \mathbf{H}_{SRF} , and an unperturbed shifting matrix $\mathbf{H}_{\text{shift}}$. For each potential source of artifacts, the unperturbed transfer matrix $\mathbf{A} = \mathbf{H}_{\text{shift}} \times \mathbf{H}_{\text{SRF}}$ is used to perform the reconstruction, while the measurements are perturbed by the addition of noise \mathbf{n} or generated using a perturbed shift matrix $\mathbf{H}'_{\text{shift}}$ or a perturbed system response matrix \mathbf{H}'_{SRF} . For the ideal spectrum \mathbf{S} , we assume $p = 100$ pixels divided by $q = 5$ subpixels. Hence, the ideal spectrum has a total 500 subpixels. Four delta functions with different intensities are placed at subpixel numbers 150, 153, 280, and 400. The peaks at 150 and 153 are representative of isobars. The unperturbed system response matrix \mathbf{H}_{SRF} is an S-11 coded aperture simulated using 3 super-Gaussians [128] placed along the matrix diagonal. Inputs to the super-Gaussian MATLAB function are as follows: X , FWHM, PE, PC, PM, and center where X is the x-axis vector, FWHM is 40 subpixels for the 100 μm slit, 60 subpixels for the 150 μm slit and 20 subpixels for the 50 μm slit, PE = 1 is the pulse energy, PC = 0 is the chirp parameter, PM = 3 is the pulse order (determines the shape of the flat top gaussian), and center is the center of each peak [128]. The unperturbed shifting matrix $\mathbf{H}_{\text{shift}}$ is generated assuming a 1/5-pixel shift. To evaluate the reconstruction with perturbed measurements, we focus on three aspects: ability to resolve the isobars at subpixels 150 and 153, peak position, and presence of artifacts. As a quantitative

evaluation metric, the root mean squared error (*RMSE*) was calculated for each level of perturbation within each investigation.

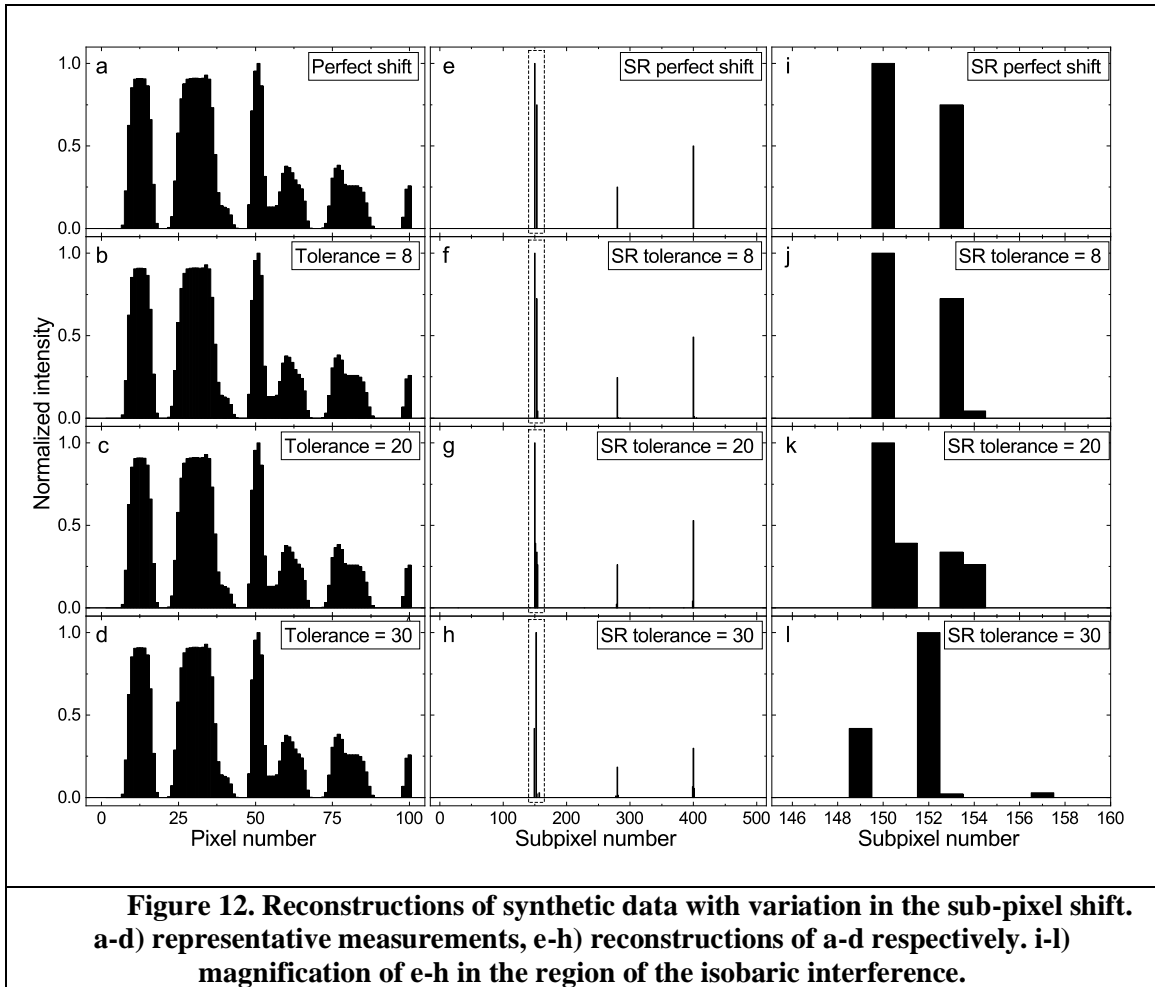
$$RMSE = \sqrt{\frac{\sum(\hat{\mathbf{S}} - \mathbf{S})^2}{p \cdot q}} \quad \text{Equation 18}$$

To investigate the effects of noise on the SR reconstruction, white gaussian noise was added to the measurements vector generated using an unperturbed transfer matrix: $\mathbf{M} + \mathbf{n} = \mathbf{M}_n$. \mathbf{M}_n is then used as the input to the reconstruction algorithm. Multiple noise levels were tested - from 0% (no noise) to 50% of the highest intensity peak in the measurements vector \mathbf{M} . Results are shown in Figure 11. Figure 11(a-d) show representative measurements \mathbf{m}_i from the measurement vector with 0%, 1%, 5% and 10% noise, respectively. Figure 11(e-h) show the results of the SR reconstruction using the unperturbed transfer matrix and Figure 11(i-l) display the same results as Figure 11(e-h), but zoomed in near the isobars at pixels 150 and 153. *RMSE* vs noise level is shown in Figure 14 a) where each point is the mean of 100 iterations for a particular noise level. As expected, artifacts increase with increasing noise level. For noise at 5% or less, the isobaric species near pixel 150 can still be resolved and appear at the correct position with the correct intensity. However, at noise of greater than 10%, the isobars can no longer be resolved, and the peaks no longer appear at the correct position. The noise experimentally observed with C-CAMMS is significantly lower than 5%, indicating that noise is likely not a significant cause of the artifacts in the experimental data. However, in future experiments with different analytes at low concentrations, noise may be a significant factor in SR reconstruction quality.



To investigate the effects of uncertainty in the subpixel shift on SR reconstruction quality, measurements were generated using an unperturbed system response matrix and a perturbed shift matrix, while reconstructions of the perturbed measurements employed unperturbed system response and shift matrices. To generate a series of measurements with uncertainty in the spectra shift, we constructed a higher resolution ideal spectrum \mathbf{S} by subdividing each subpixel further into $r = 30$ sub-subpixels. We then generated a perturbed shift matrix $\mathbf{H}'_{\text{shift}}$ for the 5 measurements by allowing a random variation in sub-subpixel shift of $r \pm t$, where t is the tolerance or range of sub-subpixel shift variation allowed, ranging from 0 to r . The 5 perturbed measurements are generated using the perturbed shift matrix $\mathbf{H}'_{\text{shift}}$ and unperturbed

system response matrix \mathbf{H}_{SRF} . Figure 12(a-d) show representative measurements \mathbf{m}_i with a tolerance $t = 0, 8, 20,$ and $30,$ respectively. Figure 12(e-h) show the results of the SR reconstruction using the unperturbed transfer matrix and Figure 12(i-l) display the same results as Figure 12(e-h) but zoomed in near the isobars at pixels 150 and 153. RMSE vs shift tolerance is shown in Figure 14 c) where each point is the average of 50 simulations for a particular tolerance. As expected, increasing the shift uncertainty reduces the quality of reconstruction. Up to a tolerance of ± 8 sub-subpixels, the peak position, intensity, and width are similar to the ideal spectrum and the isobars are easily resolved. For a tolerance of 20, the isobars appear resolved, but the relative intensity and peak width are different than the ideal spectrum reducing confidence in the reconstruction results at $t = 20$. Around tolerance 30, artifacts start to increase all over the reconstructed spectrum. Since the shift in the experimental data was determined using peak fitting, it is unlikely that shift uncertainty is a significant contributor to the artifacts observed in the experimental data. However, given the voltage change is near the limits of the source measure unit, if peak fitting were not used to validate the sub-pixel shift, the uncertainty in subpixel shift would be a significant cause of reconstruction artifacts. Furthermore, for subpixel shifts of less than $\frac{1}{2}$ pixel, peak fitting may not provide an accurate measure of the shift.



Finally, to investigate the effects of system response variation on the SR reconstruction quality, measurements are generated using a perturbed system response matrix \mathbf{H}'_{SRF} and unperturbed shift matrix, while reconstruction uses an unperturbed system response matrix \mathbf{H}_{SRF} and unperturbed shift matrix. To perturb the system response matrix, the FWHM of each super-Gaussian in the simulated S-11 coded aperture is increased from 0-40%. Figure 13(a-d) show representative measurements \mathbf{m}_i with 0, 1, 10, and 30% change in the super-Gaussian FWHM. Figure 13(e-h) show the results of the SR reconstruction using the unperturbed transfer matrix and Figure 13(i-l) display the same results as Figure 11(e-h) but zoomed in near the isobars at

pixels 150 and 153. RMSE vs noise level is shown in Figure 14 c). Again, as expected, increasing the mismatch between the perturbed and unperturbed system response decreases the quality of SR reconstruction. Artifacts increased in both intensity and number as the perturbation increased. The widths of the peaks at pixels 150 and 153 also increased. Below 10% perturbation, the isobars were resolved and appeared at the correct position. However, at greater than 10% perturbation the isobars were no longer resolved. In the experimental data, no reconstruction artifacts were observed near the O_2^+ as the O_2^+ aperture image was used to generate the system response matrix. However, artifacts were observed at N_2^+ . To help understand if the artifacts in the experimental data are primarily due to system response variations between N_2^+ and O_2^+ , we calculated the RMSE between the normalized aperture image at N_2^+ and O_2^+ and compared to the synthetic data results in Figure 14 c). The RMSE between the normalized aperture image at N_2^+ and O_2^+ in the experimental data is 0.08. From Figure 14 c), a RMSE between an exact **SRF** and a 15% perturbed **SRF** is approximately 0.08. As discussed above for a **SRF** perturbation of 10% and above, significant artifacts are observed, confirming that the artifacts observed in the experimental data are most likely a result of the mismatch between the **SRF** at N_2^+ and O_2^+ .

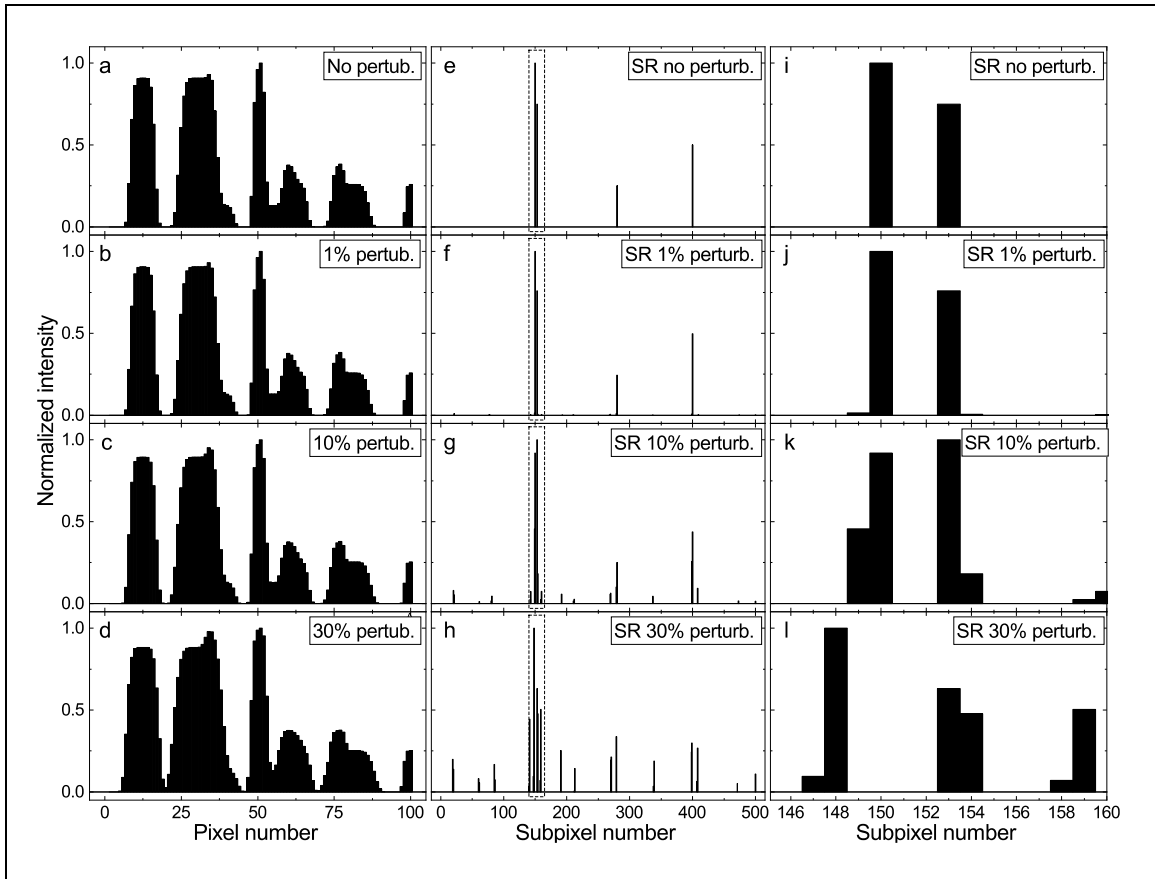


Figure 13. Reconstructions of synthetic data with a mismatch in the system response. a-d) representative measurements, e-h) reconstructions of a-d respectively. i-l) magnification of e-h in the region of the isobaric interference.

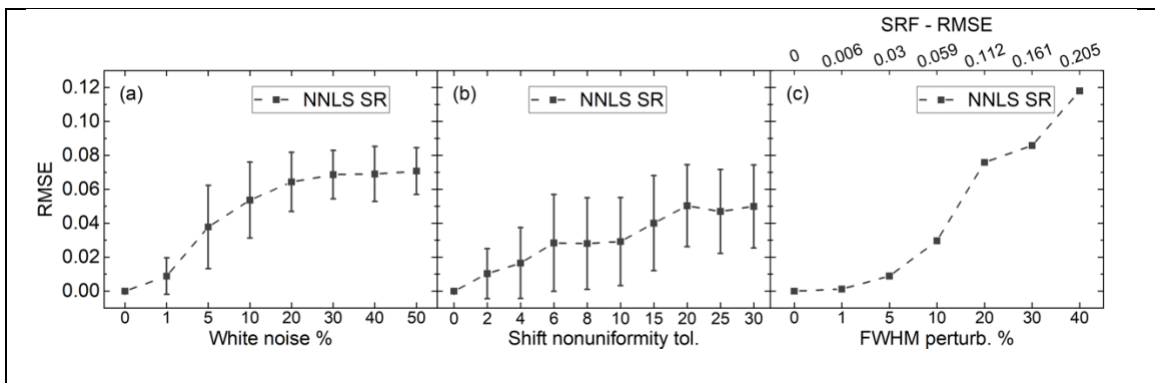


Figure 14. Plot of root mean square error between the ideal spectrum and reconstructed spectrum for different amounts of noise, uncertainty in the subpixel shift and perturbation in the system response function.

3.3.3 SR-CAMMS isobaric separation of N₂ and CO

Figure 15 shows a cross section view of our most recent cycloidal prototype SR-CAMMS. SR-CAMMS was built to fulfill requirements for spaceflight applications including:

- Detect ions with m/z up to 500 u
- Measure stable isotope ratios with a precision of $\pm 1\%$
- Distinguish between isobars at low mass ($m/z < 60$)

The design includes a thermoelectric device to cool the detector to $\sim -30\text{C}$. The electric sector electrodes are fabricated in 6061 aluminum, and then plated with gold using a high phosphorus nickel adhesion layer. Aluminum was used for the electric sector electrodes as it is non-magnetic. Plating aluminum in gold required an adhesion layer as gold does not stick to aluminum. Nickel, which is typically used as an adhesion layer between aluminum and gold, has a high magnetic permeability. However, a phosphorus content of $>9\%$ eliminates most of the magnetic permeability of nickel.

SR-CAMMS ion source is embedded inside the electric sector. The ion repeller, electron repeller, and electron anodes are all machined from 6061 aluminum and plated in gold using a similar high phosphorus nickel adhesion layer. The coded apertures are laser cut from $50\ \mu\text{m}$ thick molybdenum sheets. Similar to aluminum, molybdenum forms a surface oxide and collects charge if not coated in gold. To coat the molybdenum coded apertures in gold, we sputtered a thin TiN adhesion layer, followed by a 200 nm gold layer using electron evaporation. Figure 16 shows the full assembly of SR-CAMMS electric sector.

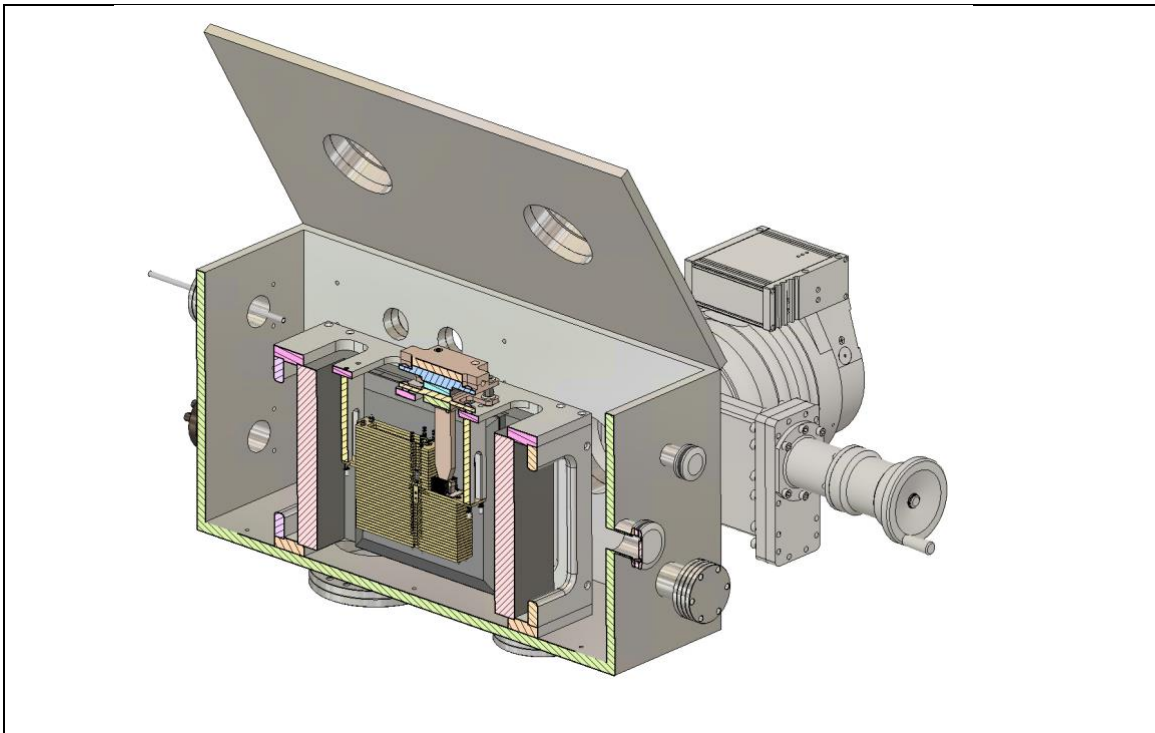


Figure 15. CAD model cross-section of the complete SR-CAMMS prototype.

In collaboration with Electron Energy Corporation, we designed an H-shaped magnet assembly that in simulation produces a field of 0.3725 T with a uniformity of 0.03%. The magnet after assembly had a magnetic field of 0.34283 ± 0.00009 T.

Finally, there are three primary differences between SR-CAMMS and C-CAMMS that impact the instrument performance. First, the distance between the edge of the detector and the center of the ion source in SR-CAMMS is 20 instead of 11 mm in C-CAMMS leading to higher mass resolution before applying the SR algorithm to SR-CAMMS (0.05 u instead of 0.08 u). Second, measurements with SR-CAMMS were performed using improved voltage sources allowing for higher precision voltage shifts. SR-CAMMS is using the 2461 SMU Keithley model. Third, the coded apertures in SR-CAMMS are laser cut in thin Molybdenum then covered with a thin layer of gold to reduce charging effects on the aperture surface that can directly affect the

system response function by making the coded aperture image not uniform across the detected mass range.

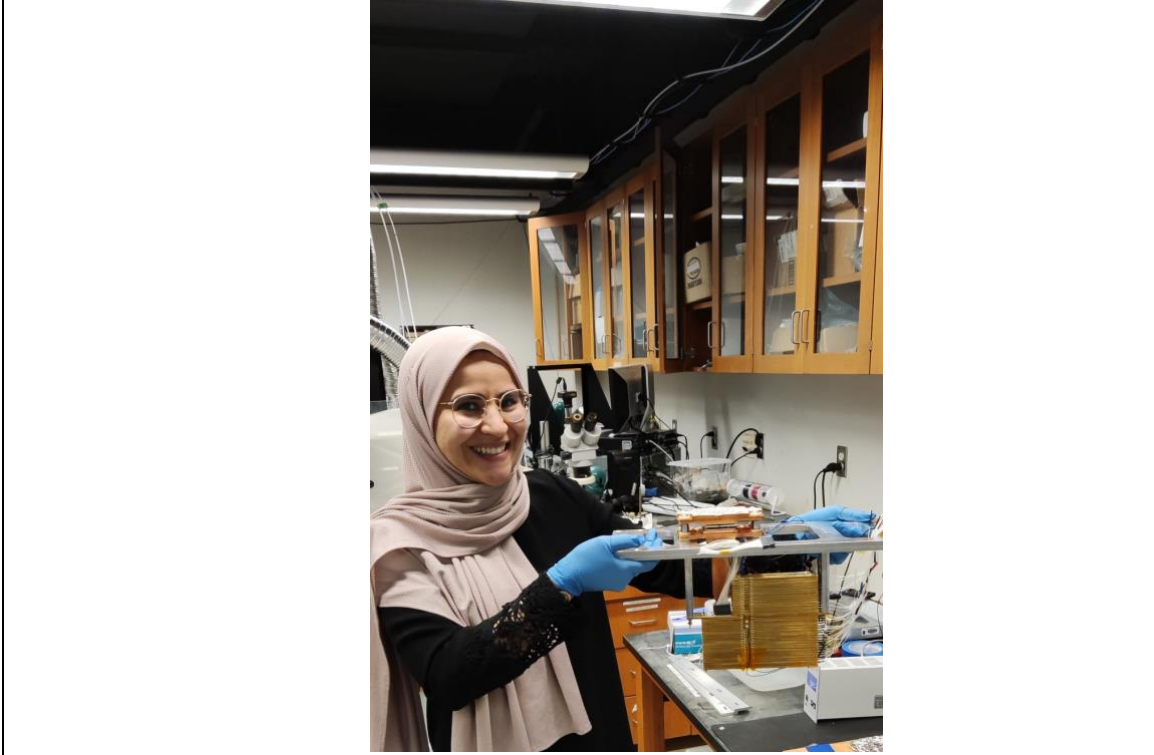


Figure 16. Photograph of graduate student Tanouir Aloui holding the fully assembled SR-CAMMS electric sector.

To test the ability of SR-CAMMS to separate isobaric species at $m/z < 60$, we introduced a mixture of 10% CO with 90% N_2 into the system through a 75 μm inner diameter 0.5 m long capillary inlet. The pressure in the vacuum system was approximately 4×10^{-6} Torr during the experiments. The electron ionization current was set to 5 μA , the detector was cooled to -30C. As described in section 3.2.2.3, a series of shifted, lower resolution spectra were combined to reconstruct a higher resolution spectrum.

The monoisotopic masses of CO and N_2 are 27.995 and 28.006 u respectively. With the SR-CAMMS instrument configured with an electric field of 2069.5 V/m, CO ions and N_2 ions

will intersect the mass analyzer focal plane and detector at 27.191 mm and 27.201 mm respectively, approximately 10 μm apart. As the detector pixels are 12.5 μm wide these ions will not be resolved in a conventional measurement. Thus, a set of 1/3 pixel shifts was used to accomplish a super resolution reconstruction and resolve the CO and N₂. Figure 17 compares a 1/3 pixel shift super-resolution reconstruction for a mixture of 10% CO and 90% N₂ with reconstruction of pure N₂. Figure 17 A and B show spectra before reconstruction. The magnified image in B shows a small shoulder on the low mass side which is likely a contribution from the 10% CO. There also appears to be a shoulder on the high mass side – this shoulder appears in both spectra and is likely due to a slightly different gain or voltage offset of this pixel. Figure 17.C shows a Richardson-Lucy deconvolution reconstruction (no subpixel shifts involved in this method as described in reference [129]) using a pure N₂ spectrum as the system response taken about 20 min before the 1/3 pixel shifted data for CO and N₂. The resolution improves vs data before reconstruction in B, but not enough to resolve the isobars. There is still a low mass shoulder on the spectrum containing 10% CO. Upon 1/3 subpixel reconstruction (Figure 17.D), the peak in the spectrum containing CO separates into a small peak to the left of $m/z = 28$ corresponding to CO and a larger peak at $m/z = 28$ corresponding to N₂, while the spectrum containing pure N₂ exhibits only 1 peak. These data indicate the ability of SR-CAMMS to resolve isobaric interferences at low mass using our super-resolution algorithm.

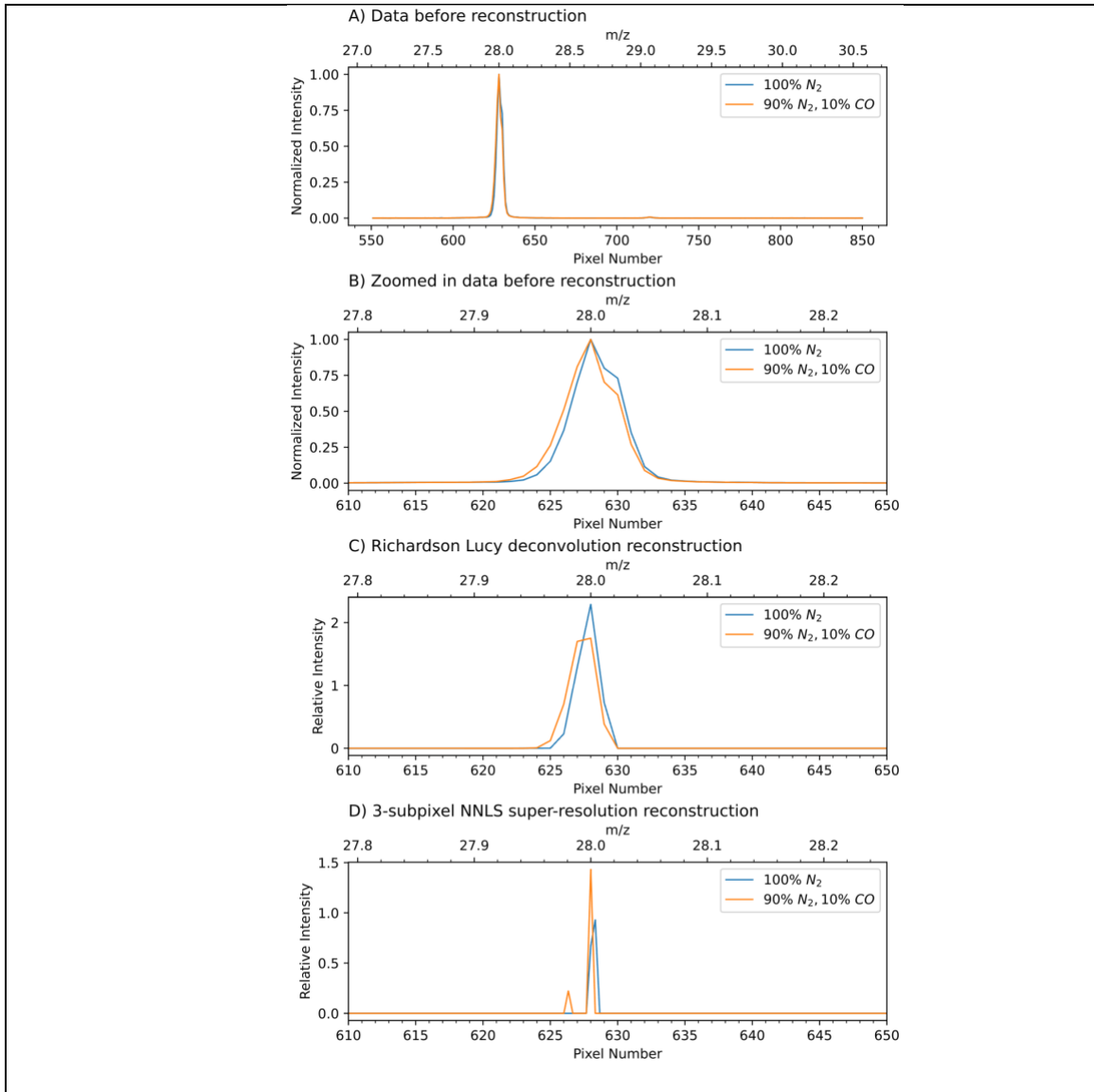


Figure 17 Data for 100% N₂ (blue) and a mixture of 10% CO and 90% N₂ (orange). A) Data before reconstruction. B) Data before reconstruction zoomed in. C) Reconstruction using an earlier N₂ spectrum to estimate the system response and a Richardson Lucy deconvolution algorithm. D) 3-subpixel NNLS super-resolution reconstruction.

3.4 Summary and conclusions

In summary, this chapter demonstrates super-resolution spectral reconstruction in C-CAMMS and SR-CAMMS using spatially shifted low resolution measurements and a

reconstruction algorithm based on solving an inverse problem with regularized techniques. Using two $\frac{1}{2}$ pixel shifted spectra at the $m/z = 28$ u peak for N_2^+ , the SR algorithm developed here resulted in a $\frac{3}{4}$ pixel FWHM at $m/z = 28$ u, demonstrating sub-pixel resolution, and a resolution of 6x better than previous spectral reconstruction with C-CAMMS. However, reconstruction resulted in some small artifacts that were investigated further using synthetic measurements with noise, variation in subpixel shift, and variation in system response function. Results with synthetic data indicate that the system response variation appears to be the most likely cause of the artifacts in the experimental data. Using higher precision voltage sources to enable smaller spectral shifts and cooling the detector resulted in potential resolution of CO and N_2 isobars when applying a $\frac{1}{3}$ of a pixel shift SR reconstruction algorithm to SR-CAMMS. This result needs to be confirmed through additional measurements in order to eliminate any doubts about the separated peaks being artifacts or real isobars. Future work will be directed towards improving the SR-CAMMS system such as establishing a robust calibration method, improving the uniformity of the electric field and enhancing the fabrication of the coded apertures to avoid charging issues.

4. Field emission electron sources

4.1 Introduction

4.1.1 Motivations

Mass spectrometers remain the foremost in situ technique for analyzing planetary materials [3-5]. Their application directly addresses key questions concerning the origins of the solar system, the prerequisites for life, and the mechanics of solar systems. These topics are central to the themes highlighted in the 2013-2022 Decadal Survey of planetary science research [1, 130]. Mass spectrometers of interest in this work and many space exploration applications require an electron source to create the ions that are identified in the mass analyzer, thereby motivating the work reported in this chapter.

High-current electron emitters are of interest for many applications, including vacuum electronics, display technologies, ion sources, and free electron lasers [1–3]. Also, Field Emission (FE) based electron sources are of a high interest for space flight applications compared to thermionic electron sources for many reasons. First, power consumption is critical for space flight applications because of the difficulty in providing energy to systems while on a space mission. Thermionic sources require heating a cathode to high temperatures to emit electrons, consuming significant power. FE sources can operate at much lower power levels since they do not require heating, which is critical for space missions where power supply can be limited, and energy efficiency is paramount. Second, FE sources, especially those based on robust materials like CNTs, can have long operational lifetimes with minimal degradation, which is ideal for prolonged space missions. In contrast, the constant heating and cooling cycles of thermionic sources can lead to reduced lifetimes and durability due to cathode material degradation. Third, reducing payload weight is always a top priority in space flight due to the high cost associated

with launching additional weight thus FE sources are advantageous because they are lighter and smaller than traditional thermionic sources.

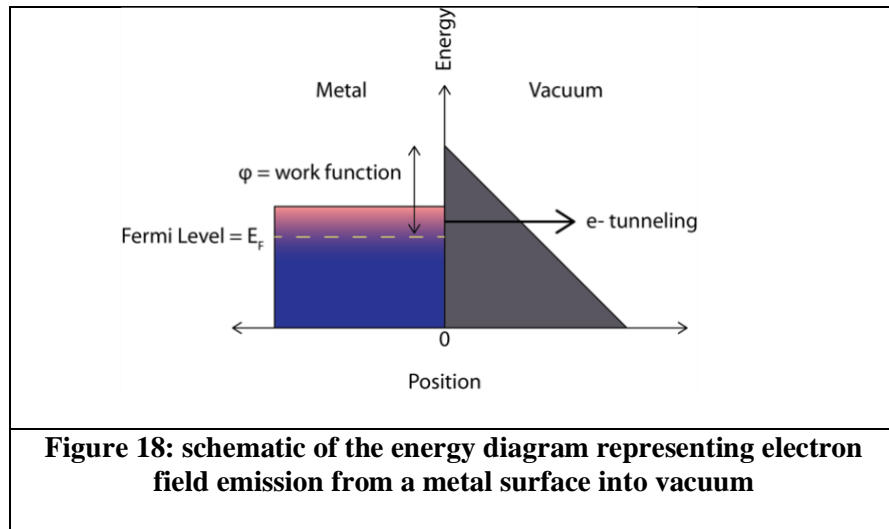
In addition to those primary benefits, there are several other properties that can be beneficial under some circumstances. FE sources can be turned on and off rapidly, unlike thermionic sources which require time to heat up and cool down producing significant amount of heat that needs to be dissipated. This can be crucial for certain space applications requiring quick response times. Furthermore, space missions often expose equipment to extreme conditions. FE sources, particularly those based on CNTs, have shown resilience to various environmental stresses which can be advantageous in space applications [131]. Finally, the high temperatures associated with thermionic sources can present safety and integration challenges, particularly if they are in proximity to sensitive instruments or systems. Field emission sources, operating at much lower temperatures, can mitigate such concerns.

In summary, the inherent advantages of field emission electron sources in terms of power efficiency, size, weight, operational flexibility, and resilience to space environments make them an attractive choice for space flight applications over traditional thermionic sources. Along with these advantages of FE electron sources come challenges mainly because state-of-the-art electron field emission devices suffer from a high turn-on macroscopic field, low macroscopic current density, short lifetime, and poor emission stability [4,5]. Electron field emission requires a strong electric field at the surface of a conductor, and lowering the applied voltage required for emission is desirable. Geometric effects can enhance the electric field at a surface, so a field emitter often takes the form of a sharpened tip or an inherently sharp material like a carbon nanotube [1–5]. Since extracting high current from an individual emitter tip can result in deformation or destruction of the tip [4], arrays of field emitter tips are typically used to obtain high total current. However, potentially damaging current can still occur when the spatial density of tips is low or if

the tips are non-uniform. Tip non-uniformity results in higher emission from sharper or taller tips, emission non-uniformity across the array, and non-linear scaling of emission current with array area [5].

In this chapter, carbon nanotube electron field emission array devices as well as electrodeposited Pt nanowires array field emission devices are fabricated and characterized as an alternative to thermionic electron emission implemented in our C-CAMMS MS prototype. Different methods that attempted to reduce emission instability in CNT based FE devices will also be discussed.

4.1.2 Theoretical background and definitions



Field emission is a quantum mechanical tunneling phenomenon where electrons escape from a metal or semiconductor surface into the vacuum, due to the application of a strong external electric field. This electron emission occurs when the external field significantly reduces the height of the energy barrier for electrons at the surface, allowing them to tunnel through the barrier as described in Figure 18. Field emission is highly dependent on the work function of the

emitter material, the strength of the applied external electric field, and the shape/ sharpness of the emitting surface.

The Fowler-Nordheim (FN) field emission theory was introduced as early as 1928 [132] to describe field emission from a planar surface, laying the groundwork for the modern band theory of metals. The initial equation that described field emission was based on assumptions regarding the nature of the tunneling barrier, leading to inaccurate predictions of the emission current density. Subsequently, Murphy and Good [133] introduced corrections to this initial equation, proposing a planar image-rounded tunneling barrier model (often referred to as the Schottky-Nordheim model). This revised model is grounded in more accurate physics and offers a more precise prediction of the local emission current density. Over the years, the FN-based field emission equation has been subjected to several modifications, and Equation 19 presents one reduced form used in this work to acquire qualitative information about experimental results. It describes the current density J as a function of the local field F and work function ϕ [134, 135].

$$J \propto \frac{F^2}{f} \exp\left(\frac{-\nu_{FB} f^{3/2}}{F}\right) \quad \text{Equation 19}$$

Where ν_{FB} is the barrier-form correction factor.

It is important to note that all these variations of equations are based on models that assume smooth surfaces. They do not account for atomic-level effects. This lack of a realistic model makes it challenging to use these equations to describe field emission from intricate surfaces, such as a Carbon Nanotube (CNT) forest.

4.2 Carbon Nanotube based field emission electron sources

Field emission electron sources using carbon nanotubes (CNTs) have attracted interest as a low power replacement over thermionic electron sources in miniature mass spectrometry

applications [136-140]. CNT-based sources consume less power, have longer lifetimes, demonstrate higher current densities, and exhibit the ability to be pulsed on and off frequently over their thermionic source counterparts in fieldable mass spectrometry applications including flight mass spectrometers [63, 141-143]. Despite the performance advantages, commercial availability of CNT-based field emission devices has been limited because of noise in the electron emission [135, 144].

The FN Equation 19 that describes field emission from a planar surface provides insights into the cause of noise in field emission from carbon nanotubes [145]. Since the emission current is an exponential function of F and $\phi^{3/2}$, small changes in either local field or work function could result in large changes in emitted current. According to de Jonge et al., most of the fluctuations/noise in emission current can be attributed to changes in local work function at the CNT tips caused by adsorption and desorption of residual gases in the vacuum chamber [146]. Conversely, multiple studies have discussed that the CNTs with f defects are more resistant to current-induced dislocation and less adsorbate deposition, and thus offer stable electron field emission [147-150].

This section reports methods and results of CNTs FE device fabrication and treatment following the method described in [146] in order to reduce the effect of adsorbates on FE performance. Patterned CNTs were encapsulated in a polymer matrix to reduce the work function variations in CNTs field emitters caused by adsorbates. By doing so, it was expected that field emission stability may be enhanced.

4.2.1 Methods

4.2.1.1 Device fabrication process

A photomask was designed to pattern the CNT growth catalyst on the substrate. N-type conductive 6-inches silicon wafers with the orientation $\langle 100 \rangle$ and a very low resistivity around 1

Ω/cm were used as substrates for CNTs FE devices to decrease series resistance and thus enhance field emission. Each row of the photomask has 10 (1 cm x 1 cm) chips where a single chip has a 500 x 500 array of dots. A combination of dot-diameters and spacing between the dots were chosen to be able to find the best pattern that provides a uniform deposition of the iron catalyst. The photolithography tool available at Duke's cleanroom facility has a theoretical resolution of 2 microns. Thus, the photomask was designed to have dots with diameters of both 3- and 2-microns with a spacing that varied from 4 to 9 microns. After running lithography tests using the designed copper on glass photomask, a layer of 5 nm thick Iron catalyst was deposited using an electron beam evaporation tool available in Duke's cleanroom (model Kurt Lesker PVD 75).

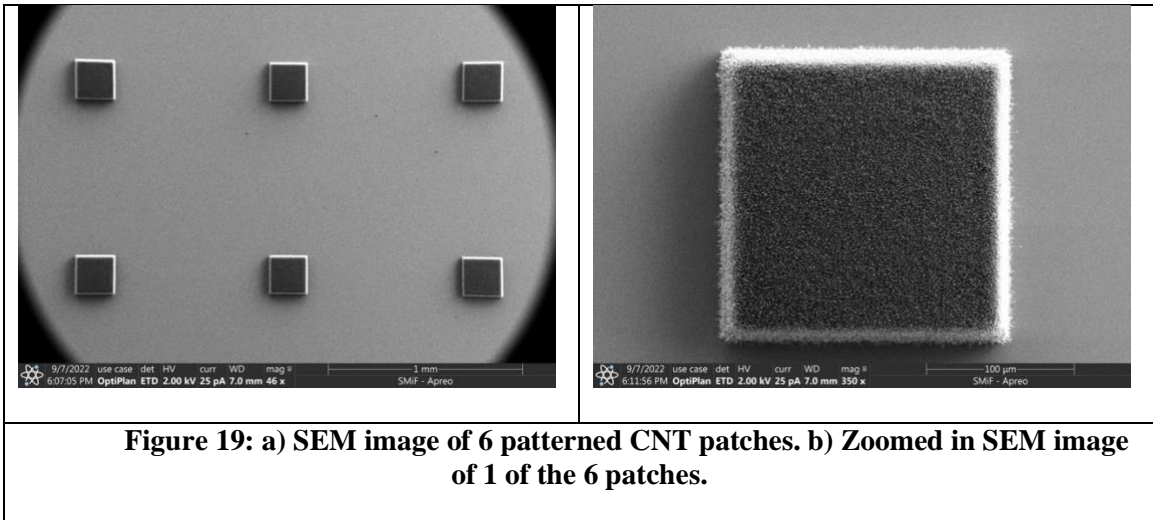
4.2.1.2 CNT growth

The CNTs were grown with a custom 915 MHz microwave plasma enhanced chemical vapor deposition system.[151, 152] One of the main advantages of using PECVD for CNT growth is the ability for many stable carbon-containing species to be created in the plasma[153]. The magnetron generates a standing electromagnetic wave in the chamber which excites and ionizes the gases in the chamber. In addition, the electric field in the plasma is thought to be responsible for the vertical alignment of the CNTs [154]. In order to preserve growth conditions inside the chamber, a seasoning run is performed without a substrate before deposition to ensure repeatability.

The substrate is firstly heated to the required temperature. Then, the gases are introduced until the required pressure for growth is reached. After the growth time ends, the reactor power, heater and gas flow are turned off and the chamber is evacuated. The chamber should cool down to less than 200°C before venting in order to reduce the possibility of having a chemical reaction of the CNTs with the air gases.

To achieve CNT growth, a pretreatment and growth phase are utilized. The pretreatment phase first starts by evacuating the system to 50 mTorr. The substrate is then heated to about 850 °C in 100 sccm of ammonia. The operating pressure was then increased to 21 Torr with a plasma power of 2.1 kW. Under these conditions a glow discharge can be observed from the ammonia plasma that is created. This pretreatment of 2 to 5 min is performed to transform the iron catalyst film into nanoparticles to serve as nucleation sites for the nanotubes.

The growth phase then consists of introducing methane to achieve following ratio: NH₃|CH₄: 50|150 sccm. The growth time was set to 180 s for the desired CNT length is around 20 μm. Typically, CNT growth began within 5-10 seconds after the introduction of methane. The ammonia dilutes the methane and provides additional hydrogen species during the growth phase to minimize the deposition of amorphous carbon on the substrate [155]. Figure 19 a) and b) show SEM images of patterned CNT arrays after growth.



4.2.1.3 Encapsulation treatment

Patterned CNTs samples were encapsulated in a polymer matrix in order to reduce the work function variations in CNTs field emitters due to adsorbates. Polymethyl methacrylate (PMMA) was chosen as the polymer material for encapsulation since it has been shown in the literature that PMMA-CNT matrices are stable electron field emitters [67, 156]. The CNTs sample was covered in PMMA/IPA 1:2 ratio) for 24 hours then left to dry in a cleanroom environment for 24 hours and finally baked at 90 degrees for 120 s in order to cure the PMMA. Figure 20 shows SEM images of an as grown CNT forest vs an encapsulated forest.

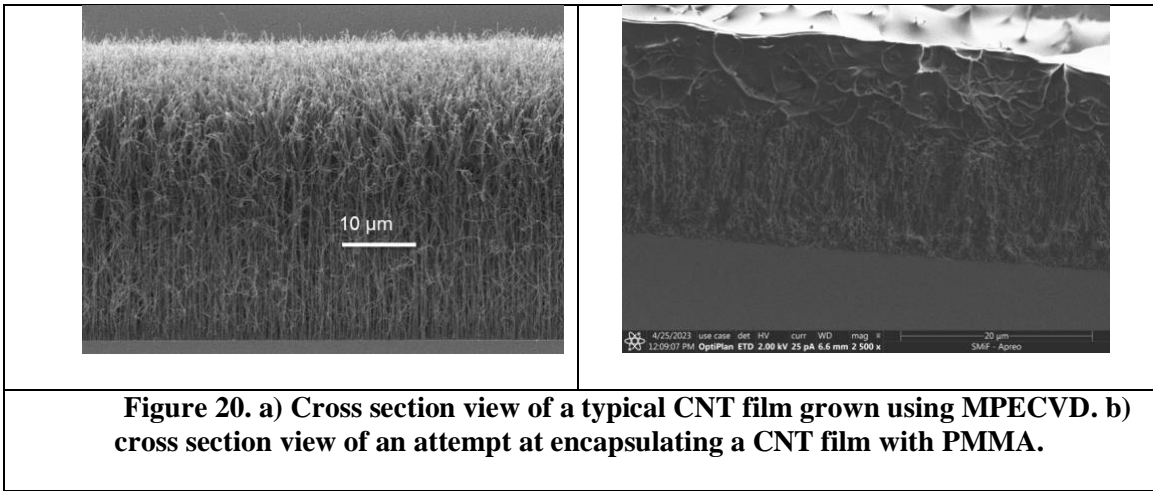


Figure 20. a) Cross section view of a typical CNT film grown using MPECVD. b) cross section view of an attempt at encapsulating a CNT film with PMMA.

The PMMA film thickness varied between 60 μm and 20 μm as measured using a Bruker Dektak 150 Profilometer. The morphologies of the samples were examined with SEM imaging after 200 nm of Gold was evaporated on top of the samples to avoid charging because the PMMA matrix is not conductive.

After encapsulation, the Trion Phantom II Oxide/Nitride/Polymer Reactive Ion Etcher provided in Duke's SMIF clean room facility was utilized to perform O_2 plasma etching for 120 s using a preset recipe for polymer etching. Only the duration of the process was moderated to achieve ~ 10 μm etching off the top of the CNTs/PMMA matrix. Etching the top of the CNTs forest was necessary to expose the tips and provide a relatively uniform heights of the emitting tubes.

4.2.2 Results and discussion

SEM characterization of as grown CNTs and encapsulated CNTs was performed to provide benchmarks for reproducibility of surface morphology during growth of the carbon nanostructures, and for morphological changes brought on by field emission measurements. Current-voltage (IV) measurements were utilized to estimate the nominal emission current density (emission current per unit emitter array area) and turn-on field. Also, measurements of

emission current over time provided a qualitative estimation of noise in the emission. Frequency characteristics of the emission current were investigated using fast Fourier transformation (FFT) of the data. Using the FFT analysis, normalized spectral density of the emission current was determined, fitted to the entire frequency range, and integrated to obtain a quantitative measure of percentage of noise in emission current for both as grown CNTs and encapsulated CNTs.

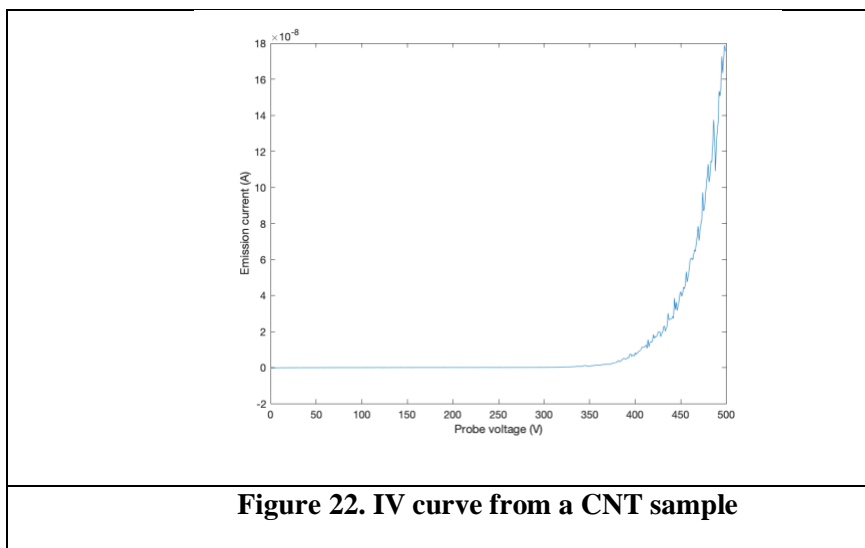
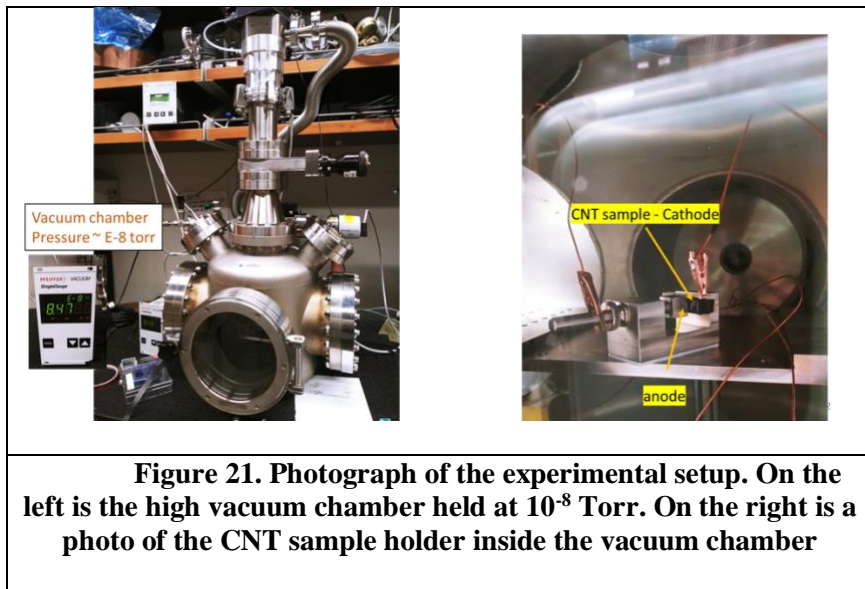
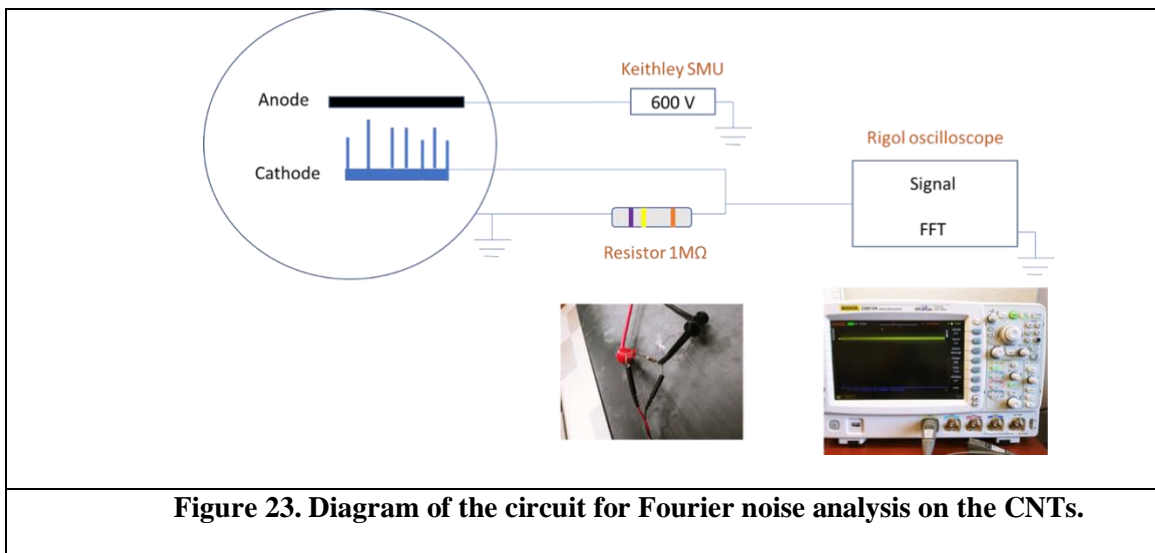


Figure 21 shows photographs of the FE testing experimental setup. Figure 22 shows a typical IV curve from a blanket coated CNT sample where the exponential behavior indicates field emission from the CNTs. In addition to IV measurements dynamic lifetime tests were performed under high vacuum levels $\sim 10^{-7}$ torr where the device is biased at the appropriate voltages for emission (usually around 300 V for ~ 0.5 mm gap distance). Emitted current is measured vs time. Lifetime tests are typically run for 1h but can be maintained for several hours and monitored until a shortage occurs.



To perform Fourier noise analysis, a resistor was added in series with the cathode. We then connected an oscilloscope in parallel to the resistor to measure the change in voltage across the resistor due to fluctuations in the CNT emission current. The oscilloscope then plots the Fourier transform of the voltage signal. Figure 23 shows a schematic of the circuit used to conduct the Fourier noise analysis on the CNTs and Figure 24 shows a plot of the root mean square voltage (U_{rms}) across the resistor as a function of frequency.

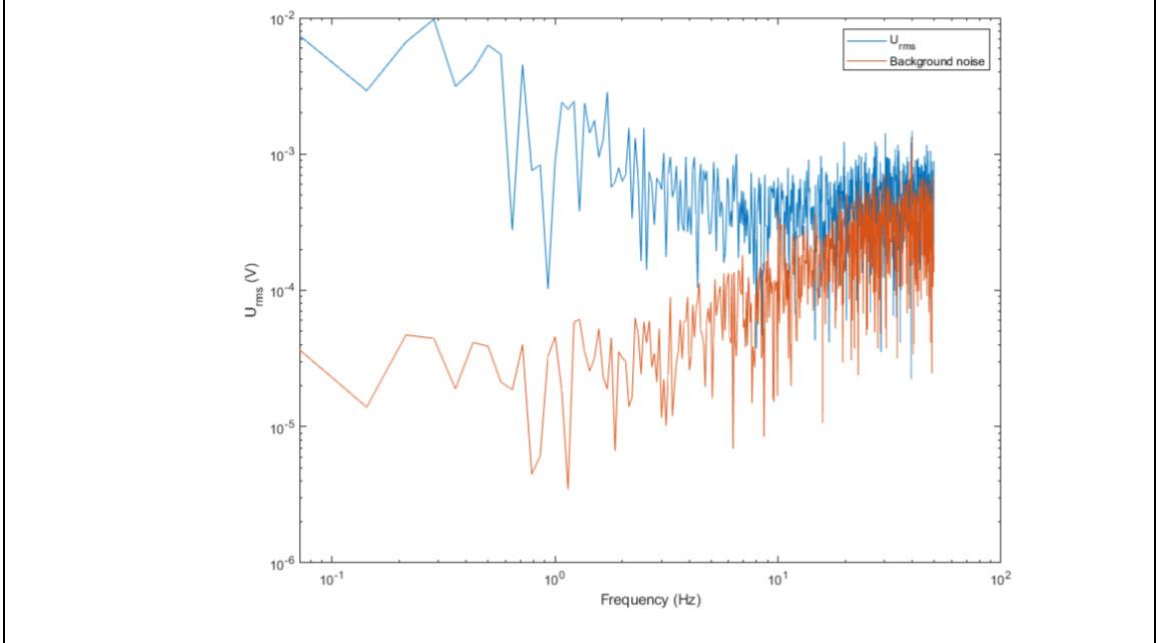


Figure 24. Fourier transform of the root mean square voltage across the resistor (U_{rms}) for a CNT field emitter (blue) and background noise without field emission.

To analyze the data in Figure 24, we first subtract the background noise from U_{rms} and then convert to normalized spectral density, $S(f)$:

$$S(f) = \frac{\Delta I^2}{I_{av}^2 \Delta f} \quad \text{Equation 20}$$

Where $\Delta I = U_{rms}/R$, R is the resistance (1 M Ω), I_{av} is the average emission current, and Δf is the measurement frequency bandwidth (here 0.07 Hz). To determine the characteristics of the noise, we then fit the resulting spectral density to the function:

$$S(f) = \frac{a}{f^\alpha} + \frac{2e}{I_{av}} \quad \text{Equation 21}$$

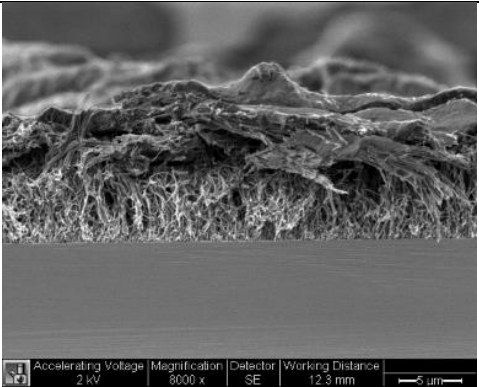
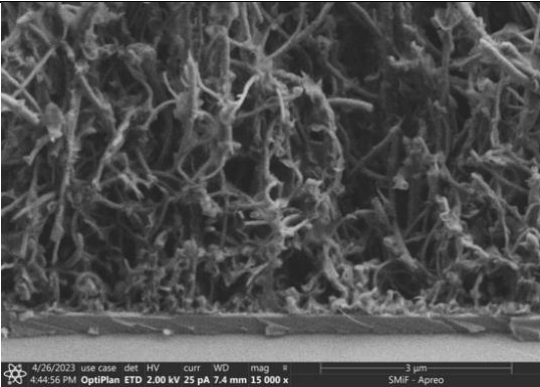
Where a and α are fit parameters, f is the frequency, e is the electron charge and I_{av} is the average current. The term $\frac{2e}{I_{av}}$ is the shot noise limit – or lowest noise possible. Previous studies indicate that if the noise in field emission current is primarily due to absorbing and desorbing

gases, α is close to 1, representing pink or flicker type noise [67, 157, 158]. When b approaches 0, the noise is just shot noise with no frequency characteristics. If b is greater than 1, other processes in addition to adsorption and desorption of gases are likely contributing to the noise.

Figure 23 summarizes the Fourier noise analysis experimental setup of the CNT field emission where the anode is held at 600 V and the emitted current is recorded using an oscilloscope. Collected data is then analyzed using a MATLAB code as follows; first the FFT of the measured emitted current is calculated to represent the signal in the frequency domain. Second, the power spectral density (PSD) is calculated and the $1/f^\alpha$ behavior of the noise in the frequency domain is confirmed. In previous research studies, when the PDS of a signal exhibits a $1/f^\alpha$ behavior the noise can be attributed to various processes involving ion bombardment induced adsorption/desorption of residual gas molecules inside the vacuum chamber and/or generation/recombination of charge carriers in the mid gap states or at surface states of the CNTs. Empirically, the distinction between these two processes can be made through examination of the slope of the PDS vs Frequency plots. When α is above 1.5, the noise is mostly caused by adsorption/desorption of molecules and the noise is a pink or flicker type noise [67, 157, 158]. However, if α is between 0.5 and 1.5 then it is most likely that noise is attributed to generation/recombination of charge carriers. Our hypothesis was that we will observe an α near 1.5 for bare CNTs and an $\alpha < 1.5$ for encapsulated CNTs assuming the encapsulation prevents gases from adsorbing and desorbing on the CNTs.

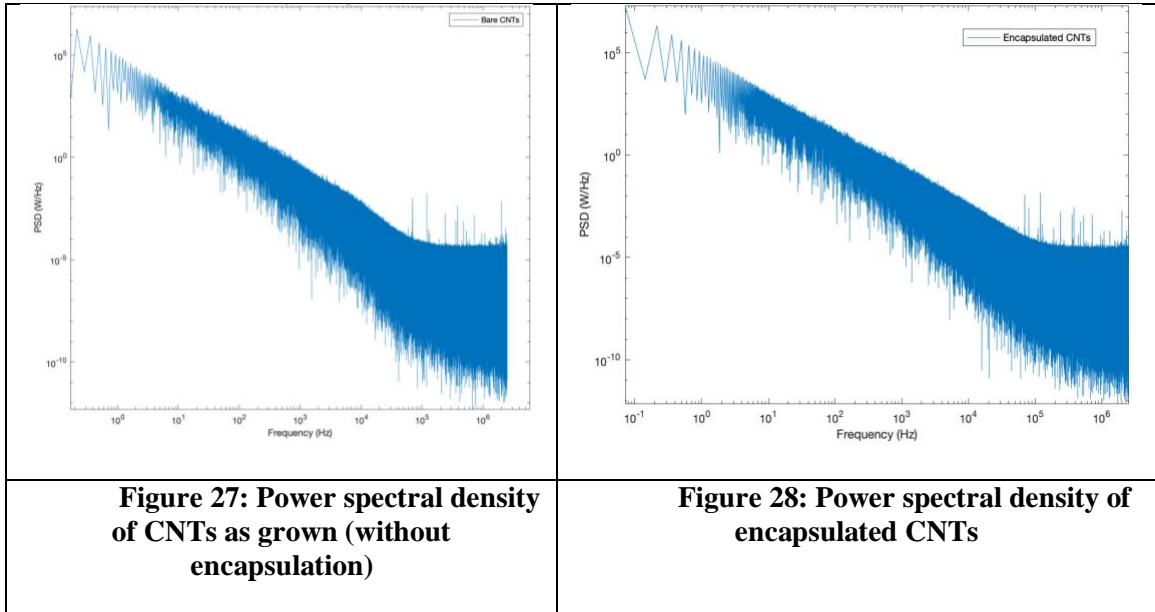
Experimentally, as shown in Figure 27 & Figure 28, there is no significant variation in the slopes of the PSD vs Frequency plots for encapsulated and bare CNTs samples. Both plots have an $\alpha \sim 1.5$ which indicates that encapsulation did not affect emission noise indicating that it did not reduce adsorption/desorption of residual gas molecules. This result can be explained by the discontinuity of the PMMA/CNTs matrix after RIE applied to eliminate the excess polymer

and expose the CNTs tips, thus similar dynamic emission variations occurred for both samples (encapsulated and bare CNTs). Note that encapsulation attempts included different experimental conditions. The first attempt used a PMMA/IPA mixture as described in section 4.2.1.3. Figure 25 shows encapsulation results after using PMMA diluted in IPA clearly showing that the polymer did not penetrate the CNT forest and formed a layer at the top of the array. Second, PMMA was diluted using its developer MIBK with a 2:1 ratio. Figure 26 shows an improvement of the polymer penetration into the CNT forest. However, the following RIE polishing step was not successful because it resulted in a non-uniform polymer/CNT matrix surface that ended in the same unstable emission behavior as the non-encapsulated CNTs.

	
<p>Figure 25. Attempts at encapsulating a CNT film. The PMMA does not penetrate the CNT film and is mostly sitting on the top of the CNTs.</p>	<p>Figure 26. Encapsulation using PMMA diluted in its developer MIBK with a 2:1 ratio.</p>

Suggested future work with the CNTs includes coating of the CNTs with a few monolayers of material such as TiO_2 or Al_2O_3 with atomic layer deposition (ALD). This technique will also cover the exposed tip and may prevent adsorption and desorption of gases. Besides CNTs field

emitters that present challenges, other types of microfabricated FE devices were explored, mainly electrodeposited nanowires arrays that are discussed in the following Section 4.3.



4.3 Electron emission from an electrodeposited metal nanowire array

Given the noise issues inherent in CNT field emitters and the difficulty of encapsulating CNTs in a polymer, other approaches to field emission are of interest for ion source applications. For example, electrodeposited nanowire arrays (ENA) investigated herein, have the potential to address several issues with field emission using a scalable, cost-effective process. The fabrication process produces nanometer-scale wires with inherently large electric field enhancement at the tip, resulting in a low turn-on macroscopic field. Also, ENA devices can achieve high spatial density of emitter tips, thereby increasing the macroscopic current density of an array without increasing the emission current per tip. The high density of tips enable lower current per tip is required to achieve a given total emission current, enabling operation farther from the high-

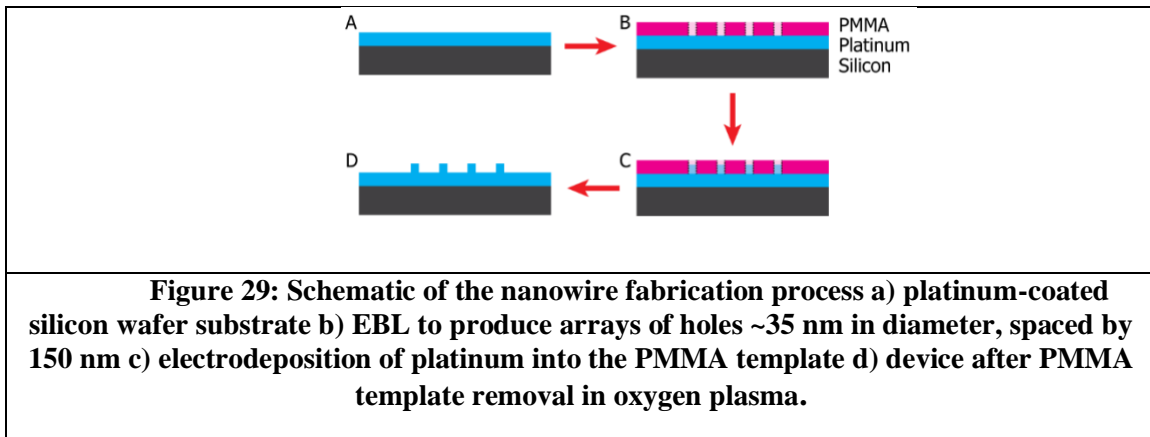
current regime where the tips could be damaged⁴. Finally, the ENA can potentially mitigate nonuniform current and damage due to tip shape variation because templated electrodeposition produces uniform nanowires^{6,7}.

The objectives of this work were to fabricate a high spatial density array of metallic nanowires and demonstrate high macroscopic current density electron emission from this array. We developed a templated electrodeposition process to create the device structure. Herein, we describe our fabrication process using electron beam lithography (EBL) to create a polymer template followed by electrodeposition of platinum into the template and characterization of the array's morphology and electron emission performance.

4.3.1 Experimental procedure

We fabricated platinum nanowire arrays using the process illustrated in Figure 29. Electron beam evaporation was used to deposit 25 nm Ti, followed by 100 nm Pt onto an undoped silicon wafer substrate. MicroChem 950 PMMA A2 electron resist was spin-coated onto the metallized substrate using static casting, 500 rpm/s ramp speed and spinning at 500 rpm for 5 seconds, then 1000 rpm/s ramp speed and spinning at 3000 rpm for 45 seconds. Spin-coated films were baked at 180 °C on a hot plate for 3 minutes. An Elionix ELS-7500 EX E-Beam Lithography System was used to expose the PMMA films. The PMMA resist was developed in 1:3 MIBK:IPA for 10 minutes, then rinsed in IPA for 5 minutes. The film thickness was measured to be ~70 nm using a Bruker Dektak 150 profilometer.

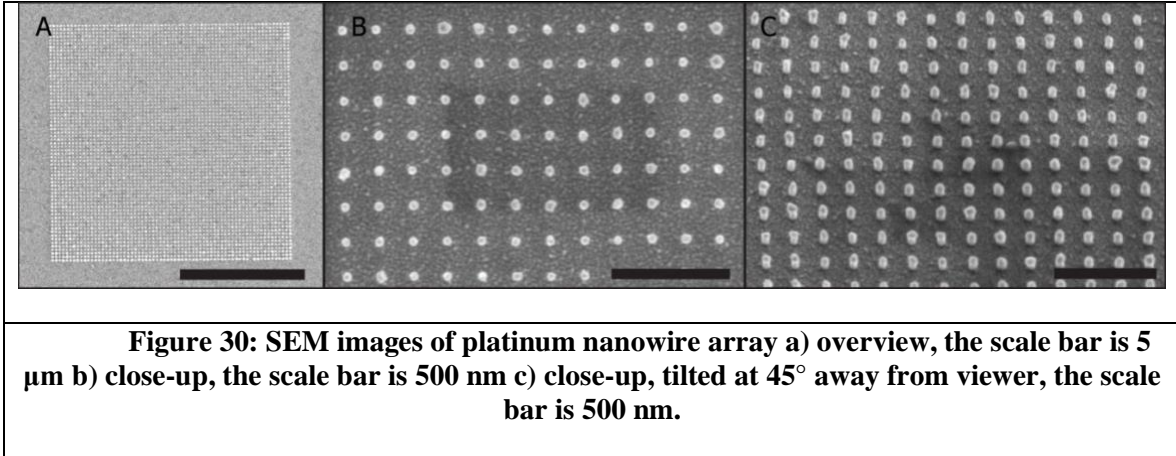
EBL was chosen in order to provide flexibility in the tip pitch, diameter, and height that could be fabricated. Optimal tip array properties (diameter, pitch, height) determined using EBL could then be fabricated via another more cost-effective method. Nanoimprint lithography and block copolymer lithography are both much more scalable and affordable than EBL.



To ensure that the bottoms of patterned holes in the PMMA template were clear of resist, the films were processed in an oxygen plasma etch for 5 seconds using 50 sccm O₂, 15 W RIE power, 10 mTorr pressure, and 0 W ICP power in a Trion Technology Phantom II reactive ion etcher. Platinum nanowires were created by partially filling the holes in the PMMA template using electrodeposition. The electrodeposition solution contained 75% water by volume, 25% methanol by volume, 0.1 M NaCl, and 0.001 M H₂PtCl₆. The H₂PtCl₆ was added to the solution five minutes before electrodeposition and allowed to mix thoroughly.

The sample was mounted in the electrodeposition solution using a custom-built fixture. Electrodeposition was performed while continuously mixing the solution with a magnetic stir bar. The working electrode potential was measured using an Ag/AgCl reference electrode, and a platinum wire was used as a counter electrode. The sample was allowed to dwell in the solution for two minutes before electrodeposition. A BioLogic SP-300 potentiostat was used to apply -0.3 V vs. Ag/AgCl to the working electrode in 16 cycles of 1 second on, followed by 10 seconds at open circuit voltage, resulting in platinum deposition into the holes in the PMMA template. After electrodeposition, the template was removed using an oxygen plasma etch for 5 minutes at 100 W plasma power, and 6×10^{-1} mbar pressure in an Emitech K-1050X plasma asher. The SEM images

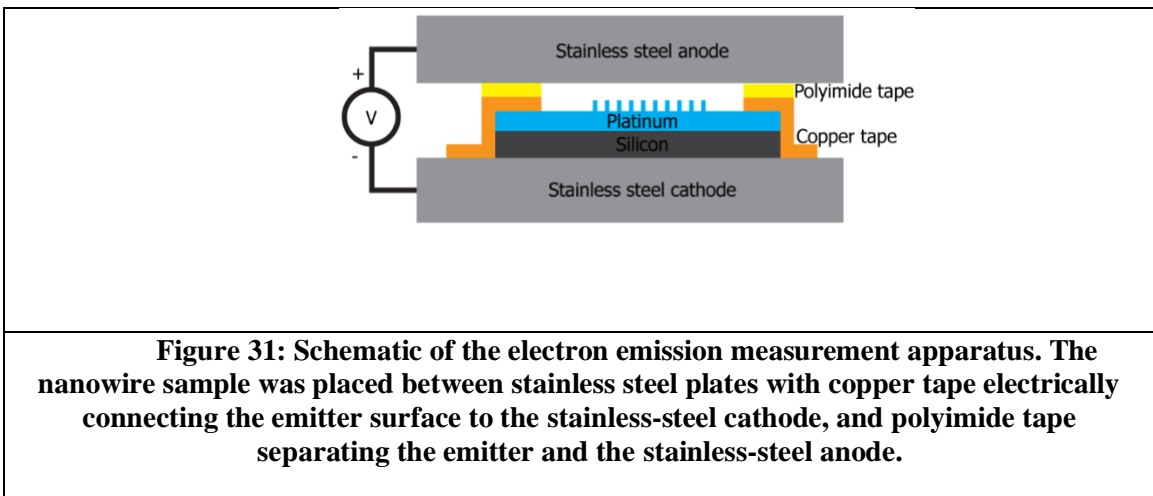
in Figure 30 show the morphology of the resulting nanowires. The array has a square grid configuration with a nanowire pitch of 150 nm in both dimensions. Using SEM measurements and Fiji image processing software⁸, we calculated the wires to be ~35 nm in diameter and ~60 nm in height.



The chosen dimensions were a compromise between an estimate of what would perform well and what could be successfully fabricated. Maximizing the field enhancement factor at the emitter tips requires small diameter, large pitch, and sufficient length to minimize the influence of the surface. Harris et al have investigated screening effects in arrays, particularly the effect on the field enhancement factor [9,10]. Additional length is expected to have diminishing returns after a point. Smaller diameter tubes are more challenging to fabricate and are more fragile. Smaller pitch should increase current density but could increase field screening at the tips and reduce field enhancement factor if reduced too far.

The emission performance of the platinum nanowire array was measured in a vacuum chamber operating between 1×10^{-6} and 1×10^{-7} Torr. The experimental configuration is illustrated in Figure 31. The platinum nanowire cathode was mounted on a stainless-steel plate and a second

stainless steel plate comprised the anode. The platinum surface of the nanowire array sample was electrically connected to the stainless-steel cathode plate using copper tape. Polyimide tape was placed over the copper tape to serve as an insulating spacer between anode plate and platinum nanowire cathode. The anode to cathode distance was equal to the combined thickness of the polyimide and copper tapes and was measured with a micrometer to be $\sim 150 \mu\text{m}$. Steel wires were spot-welded to the anode and cathode stainless steel plates to enable electrical contact to the electrodes. Two Keithley 2410 source-measure-units were used to apply controlled voltages to anode and cathode and to measure the current emitted from the cathode and collected by the anode.



Current-voltage measurements were performed by measuring the electron emission current collected by the anode while the voltage on the anode was varied between 0 and 1000 V and the cathode was held at 0 V. The anode voltage was limited if the measured current exceeded $2 \mu\text{A}$ (i.e. compliance limit was set to $2 \mu\text{A}$) in order to prevent damage to the emitter nanowires. The applied voltage was swept from low to high, then high to low, 5 times in each direction. The average and standard deviation of the electron emission current measurements was calculated.

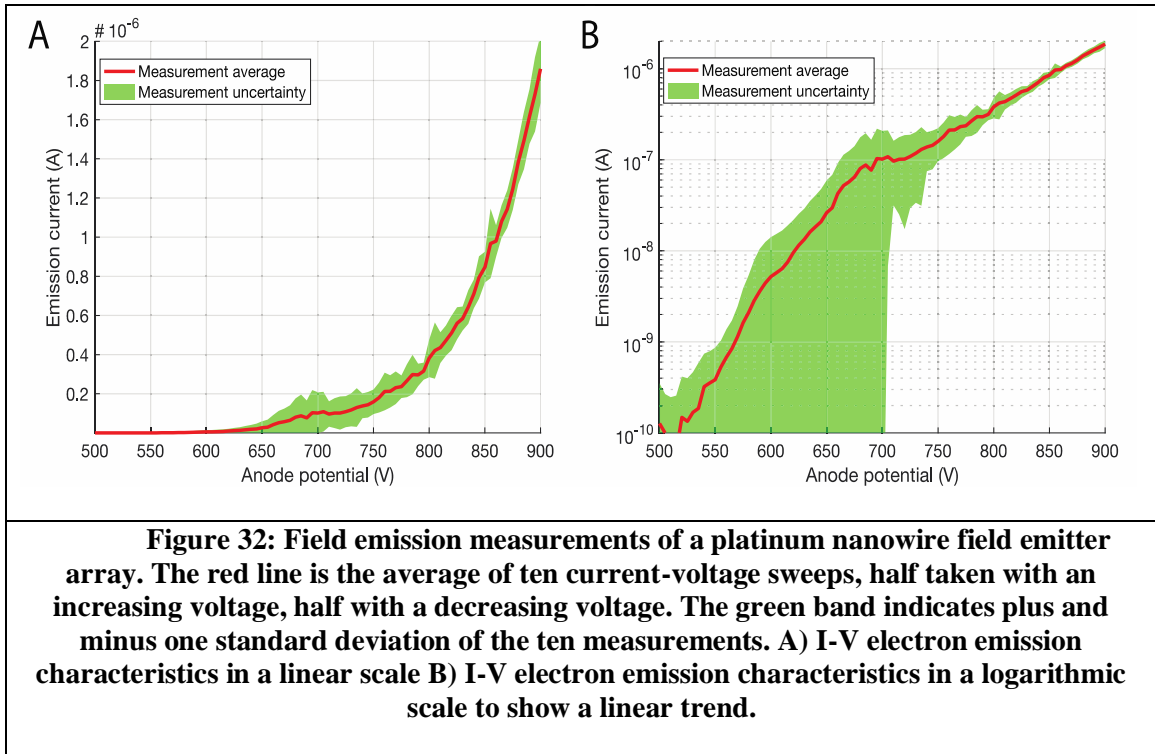
Constant voltage electron emission measurements were performed by measuring the electron emission current collected by the anode while applying 700 V to the anode and holding the cathode at 0 V. The anode voltage was adjusted toward zero by the source-measure unit if the electron emission current exceeded 2 μA , i.e., the compliance limit was set to 2 μA .

Constant current electron emission measurements were performed by applying a voltage to the anode that resulted in 2 μA emission current, i.e., the source-measure unit was set to source 2 μA . The voltage required to source this emission current was measured and recorded.

4.3.2 Results and discussion

4.3.2.1 Current-voltage measurement

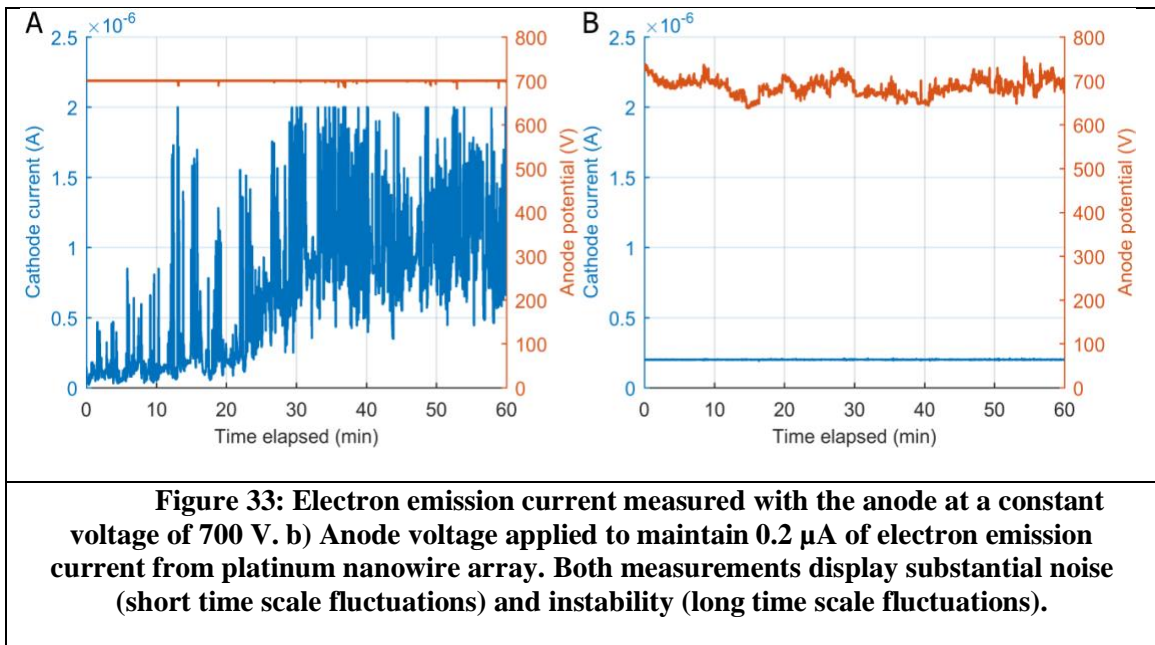
We measured the electron emission behavior as a function of applied voltage, as shown in Figure 32. The device emitted 1 nA at an applied voltage of 565 V, resulting in an approximate turn-on macroscopic field of 4.35 V/ μm . At the highest applied voltage, 900 V, the macroscopic current density was 2 A/ cm^2 . SEM images acquired after electron emission testing show that the nanowires appear undamaged by the tests. The measurement average, measurement uncertainty. The exponential nature of the data suggests field emission. However, additional experiments beyond the scope of this study would be required to fit this data to an emission model given the complications of existing models discussed previously.



4.3.2.2 Stability measurement

Some applications, *e.g.* coded aperture mass spectrometer ion sources, require a very stable, low-noise electron field emission source [20]. Here, we define instability as emission current change that occurs on a time scale of minutes and longer, and we define noise as emission current change that occurs on a time scale of seconds and shorter. Constant voltage Figure 33.A and constant current Figure 32.B measurements were performed on a typical as-prepared sample. No conditioning was performed prior to testing. For the constant voltage test, shown in Figure 32.A, we measured substantial noise in the emission current. One method to mitigate emission current change in a practical system is to alter the applied voltage to maintain constant emission current. This mode of operation is shown in Figure 33.A, where we supplied and measured the voltage required to maintain 0.2 μA of emission current. Active modulation of the voltage applied to the cathode did produce a constant emission current, but both the constant voltage and constant

current measurements exhibit substantial noise and instability in the measured current and the measured voltage, respectively. This finding is unsurprising since electron field emission noise has previously been found to be strongly influenced by the background gas pressure [21]. At pressures above 5×10^{-9} Torr, significant emission current noise and drift can be expected from all types of field emitters due to adsorbates and surface migration of atoms [21]. These measurements underscore the observation that the use of field emission in conditions other than ultra-high vacuum is extremely challenging. Mitigating the phenomena responsible for emission noise would likely facilitate the application of field emission electron sources in practical devices, particularly those which require background gas loads such as the aforementioned ion sources in mass spectrometers.



4.4 Summary and conclusions

In summary, we fabricated and tested two different types of electron field emission devices, one based on CNTs arrays and one based on electrodeposited Pt nanowires that is a novel material and structure for electron emission. PECVD grown CNT arrays presented an unstable dynamic emission behavior. We applied an encapsulation method to embed the CNTs in a polymer PMMA matrix and eliminate the effect of adsorbates on the CNTs tips. The encapsulation process showed progress towards a high-quality encapsulation but did not enhance the emission behavior of these devices that lead us to explore the Pt nanowires. These electrodeposited nanowire field emitter arrays showed lower turn-on macroscopic field than gated tip arrays, possess higher emitter density than gated tip arrays, and displayed higher emission macroscopic current density than carbon nanotube arrays. Further, we were able to extract a constant electron emission current from this device by actively modulating the voltage applied to the cathode. It is likely that substantial performance improvement is possible with additional development of this proof-of-concept structure. For example, incorporating an integrated gate electrode with the platinum nanowires would improve the turn-on macroscopic field and would allow higher macroscopic current density by mitigating electric field screening due to adjacent nanowires. Also, replacing EBL with nanoimprint lithography and replacing platinum with an alternative material such as silver or nickel would lower the manufacturing cost. These findings lead us to conclude that templated electrodeposition of metallic nanowire arrays is a promising approach for producing high performance electron emission devices.

5. Conclusions and future perspectives

This research investigated several mass spectrometry technologies for spaceflight applications, supporting the cross-cutting themes of planetary science research as described in the National Research Council's 2013-2022 Decadal survey [1-5]. In particular, these technologies are ultimately expected to enable better understanding of solar system beginnings, assist in the search for the requirements for life beyond earth, and help us understand the workings of solar systems. This work targeted three objectives including; (1) reducing spectral reconstruction artifacts in cycloidal coded aperture miniature mass spectrometer, (2) implementing super-resolution in mass spectrometry and (3) developing field emission based electron sources for electron ionization in mass spectrometer applications. Each objective provided a significant advance towards development of a mass spectrometer with ideal characteristics for planetary exploration, and also identified opportunities for further development.

5.1 Spatially coded apertures (Chapter 2)

Spatially coded apertures enable increasing throughput and sensitivity without changing the size or resolution of an instrument – highly desirable characteristics for a space flight instrument. Cycloidal mass analyzers have unique focusing properties that, combined with spatially aperture coding, enable reconstruction with a shift-invariant system response. However, experimentally cycloidal mass analyzer systems do not have shift-invariant system response functions. For instance, the system response function in our C-CAMMS-MP prototype described in chapter 2 depends on m/z . The m/z dependence is a result of the non-uniform illumination of the coded aperture due to an early curvature of ions inside the ion source [77]. This issue of a non-uniform system response function led to reconstruction artifacts in experimental data that needed to be addressed. In chapter 2, two methods to reduce artifacts in the C-CAMMS-MP prototype were designed and demonstrated. First, the system response function was estimated for

different m/z instead of using the same estimation to reconstruct the full mass range. Second, to assure a uniform illumination of the S-11 coded aperture slits, the slits were shifted off-center above the ionization volume. Both methods were successful in significantly reducing reconstruction artifacts. Note that the hardware modification is favored because it maximizes throughput, simplifies reconstruction, and simplifies spectral calibration. Finally, both techniques are valid for future instruments using spatially coded apertures in a cycloidal mass analyzer to reduce spectral reconstruction artifacts.

For Future work, I suggest developing a robust system response calibration method, perhaps using AI to train a neural network with a reasonable number of experimental data sets. Furthermore, improving the uniformity of the electric field, and enhancing the fabrication of the coded apertures to avoid charging issues, which is critical for the system response stability, will help ensure that the system response function does not change as a function of time.

5.2 Super-resolution reconstruction (chapter 3)

Chapter 3 represents the core of this research where super-resolution was demonstrated in two instrument prototypes, C-CAMMS and SR-CAMMS. This method employs spatially shifted low resolution measurements and a reconstruction inverse problem solving algorithm with regularized techniques. Sub-pixel resolution, and 6x better resolution than previous spectral reconstruction with C-CAMMS were demonstrated with the super resolution algorithm developed and applied using two $\frac{1}{2}$ pixel shifted experimental spectra at the $m/z = 28$ u peak for N_2^+ . Reconstruction resulted in a $\frac{3}{4}$ pixel FWHM at $m/z = 28$ u. However, some small artifacts were noticed after reconstruction that led to a comprehensive synthetic study to investigate the potential source of artifacts using synthetic measurements with noise, variation in subpixel shift, and variation in system response function. According to the synthetic study results the most likely cause of artifacts is variation in the system response function estimation.

One of the primary achievements of this work was the preliminary resolution CO and N₂ isobars. This was accomplished by applying a 1/3 of a pixel shift SR reconstruction algorithm to SR-CAMMS using higher precision voltage sources to enable smaller spectral shifts and cooling the detector. This result should be confirmed through additional measurements to eliminate any doubts about the results due to possible artifacts in the spectra.

Based on the preliminary synthetic study comparing super resolution combined with aperture coding vs super resolution implemented with a single slit, resolution improvement is higher when SR is combined with aperture coding. For future work, I suggest performing additional computational testing and experimental data collection to validate this hypothesis. Furthermore, the SR algorithm developed in chapter 3 can be improved by studying other regularization methods such as iterative methods listed in ref. [126]. Finally, the SR algorithm currently requires precise knowledge of the size of the spectra shift. This is quite difficult to measure in practice. Therefore, I suggest developing an algorithm that does not require precise knowledge of the size of the spectral shift and tolerates a small measurement error.

5.3 Field emission electron sources (Chapter 4)

Chapter 4 was the most challenging because of the complexity that comes with nanofabrication and experimental testing of field emission devices. Two different types of electron field emission devices were fabricated and tested, one based on CNT arrays and one based on electrodeposited Pt nanowire arrays. The dynamic emission behavior of CNT arrays grown via PECVD was found to be unstable due to adsorbates on top of the CNTs. To mitigate the effects of adsorbates at the tips of the CNTs, I embedded the CNTs within a PMMA polymer matrix. Although encapsulation quality improved after adjusting the experimental procedure, it failed to improve the emission characteristics, prompting an investigation into Pt nanowires.

Arrays of field emitters fabricated from electrodeposited nanowires outperformed gated tip arrays by requiring a lower turn-on macroscopic field, providing a higher emitter density, and achieving greater macroscopic current density than the carbon nanotube arrays. By applying active modulation to the cathode voltage, we succeeded in deriving a steady electron emission current from these devices. Given the recent stage of this proof-of-concept structure, there is a strong potential for enhancing performance. Integration of a gate electrode with the platinum nanowires, for instance, could further reduce the macroscopic turn-on field and enable an increase in macroscopic current density by countering electric field screening from neighboring nanowires. Moreover, the transition from electron beam lithography to nanoimprint lithography and the substitution of platinum with more cost-effective materials like silver or nickel could significantly reduce production expenses. This research thus supports the view that the templated electrodeposition of metallic nanowire arrays holds considerable promise for the fabrication of high-performance electron field emission devices.

Other directions are possible to address noisy field emission. Other carbon nanostructures ranging from nano-sheets, edge-textured highly oriented pyrolytic graphite (HOPG_E), activated carbon, bamboo CNTs, and graphenated CNTs (gCNTs) have been examined in literature for field emission applications as an alternative to aligned CNTs [159-163]. Because of their higher aspect ratio, aligned-gCNTs are good candidates for use as field electron emission sources for increased field enhancement at the tips and an increased edge density providing more field emission sites [137, 164, 165]. Graphenated CNTs are hybrid carbon nanostructures having layers of graphene foliates protruding from the sidewalls of vertically oriented MWCNT forests [166-168]. There is a lack of literature studying FE noise performance of gCNTs compared to aligned MWCNTs, thus this is a fruitful direction from future research.

In theory, graphenated carbon nanotubes (gCNTs) may display a noisier emission current due to a higher edge density that provides more emission sites, as compared to their non-graphenated multi-walled carbon nanotube (MWCNT) counterparts covering an identical surface area. Insights from the literature on gCNTs suggest a possible hypothesis regarding the noise in emission current of these hybrid carbon nanostructures. A relative increase in the D/G ratio in gCNTs, indicated by Raman spectroscopy, is a result of defects in the graphene foliates [163, 169]. Graphenated CNTs may have more stable FE behavior than aligned CNTs or the opposite. Both hypotheses can find supporting arguments from the literature, therefore a comprehensive comparison between both devices will help us advance the knowledge towards a more stable FE from CNTs nanostructures.

In addition to exploring gCNTs, the encapsulation treatment examined in this work should continue with new procedures. For example, coating the CNTs arrays with a thin film of alumina should be attempted before embedding the structure in the polymer matrix. This is expected to improve coverage uniformity and ease the polishing step.

Appendix A

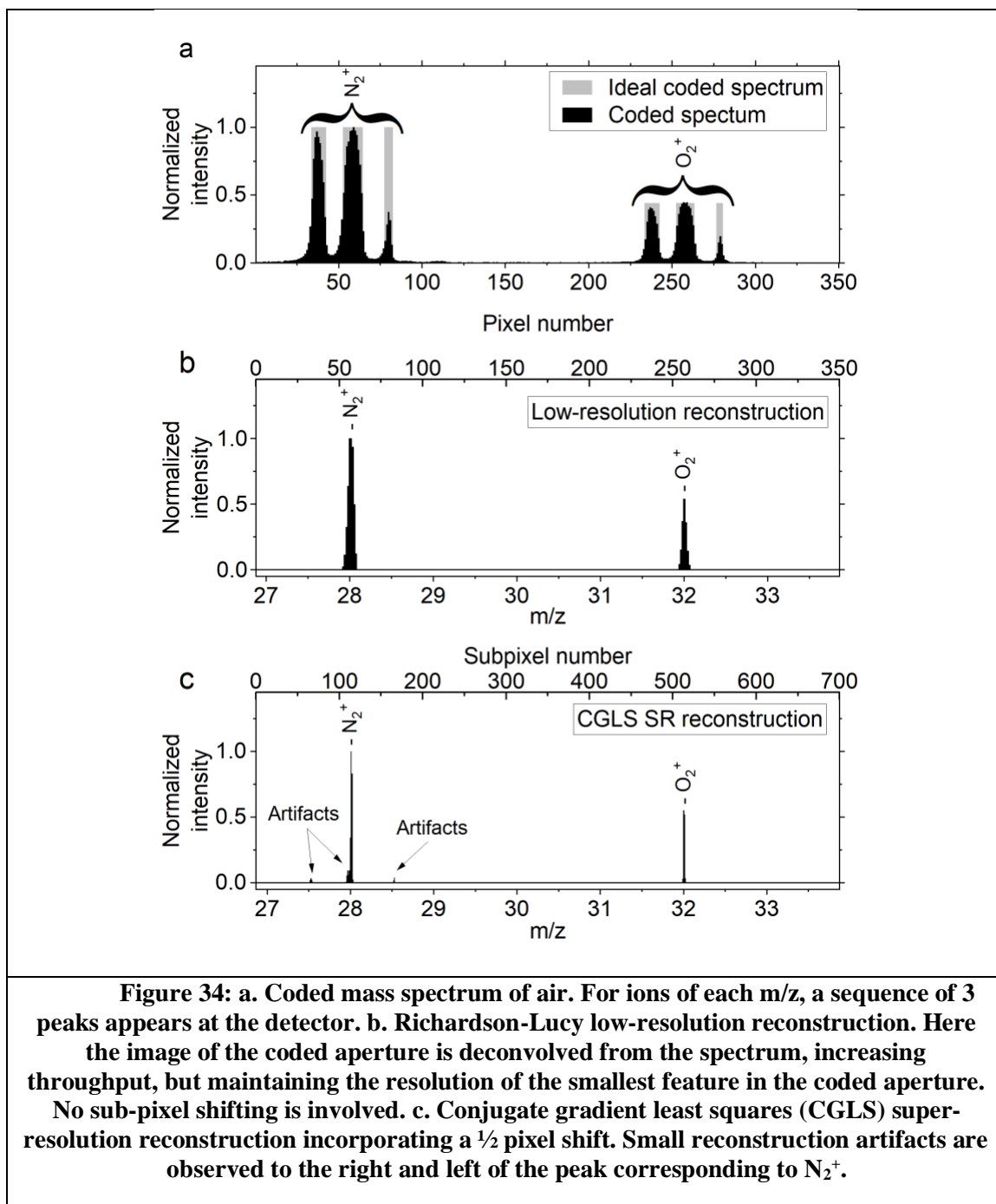


Figure 34: a. Coded mass spectrum of air. For ions of each m/z , a sequence of 3 peaks appears at the detector. b. Richardson-Lucy low-resolution reconstruction. Here the image of the coded aperture is deconvolved from the spectrum, increasing throughput, but maintaining the resolution of the smallest feature in the coded aperture. No sub-pixel shifting is involved. c. Conjugate gradient least squares (CGLS) super-resolution reconstruction incorporating a $\frac{1}{2}$ pixel shift. Small reconstruction artifacts are observed to the right and left of the peak corresponding to N_2^+ .

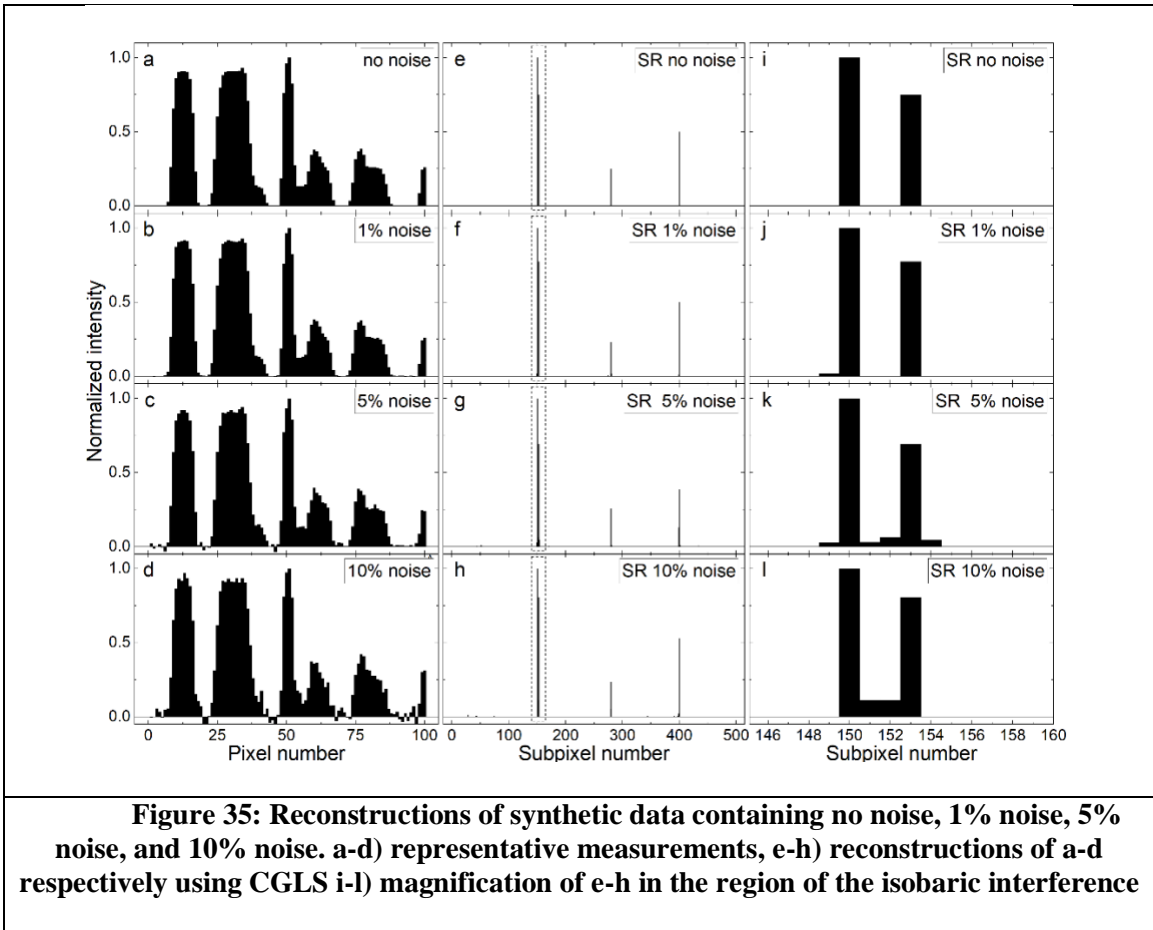


Figure 35: Reconstructions of synthetic data containing no noise, 1% noise, 5% noise, and 10% noise. a-d) representative measurements, e-h) reconstructions of a-d respectively using CGLS i-l) magnification of e-h in the region of the isobaric interference

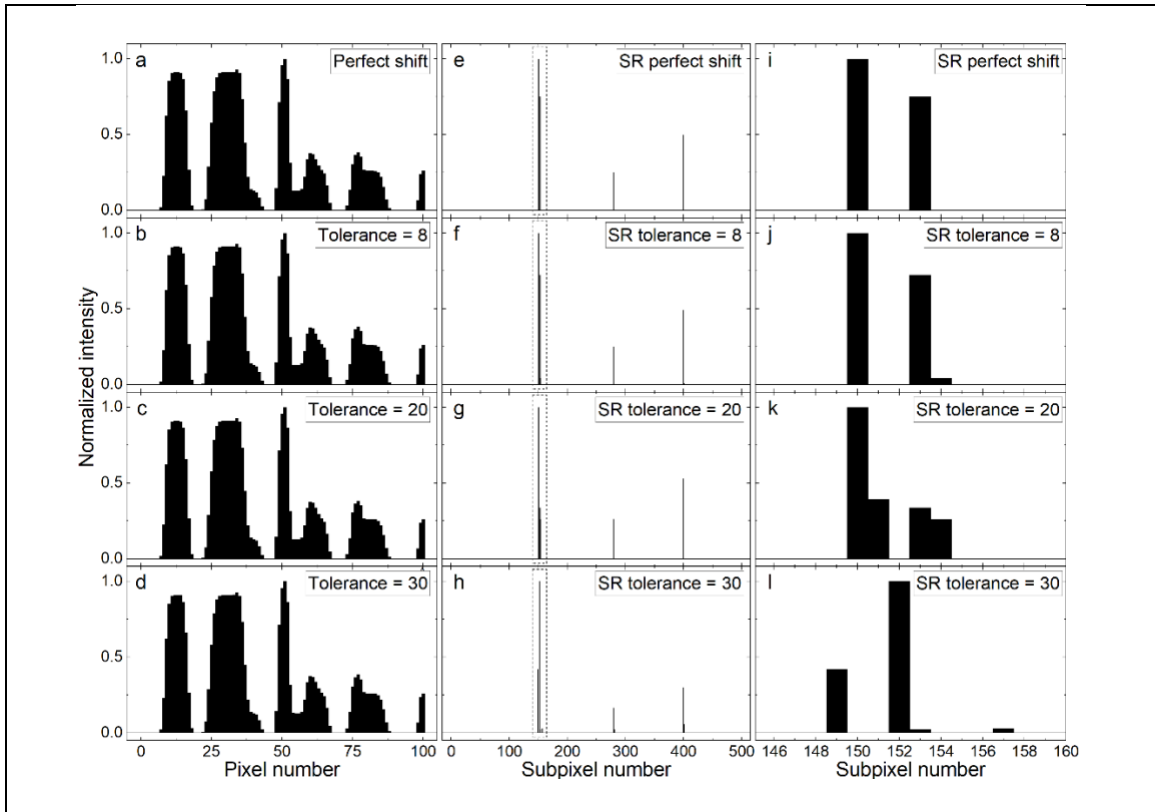
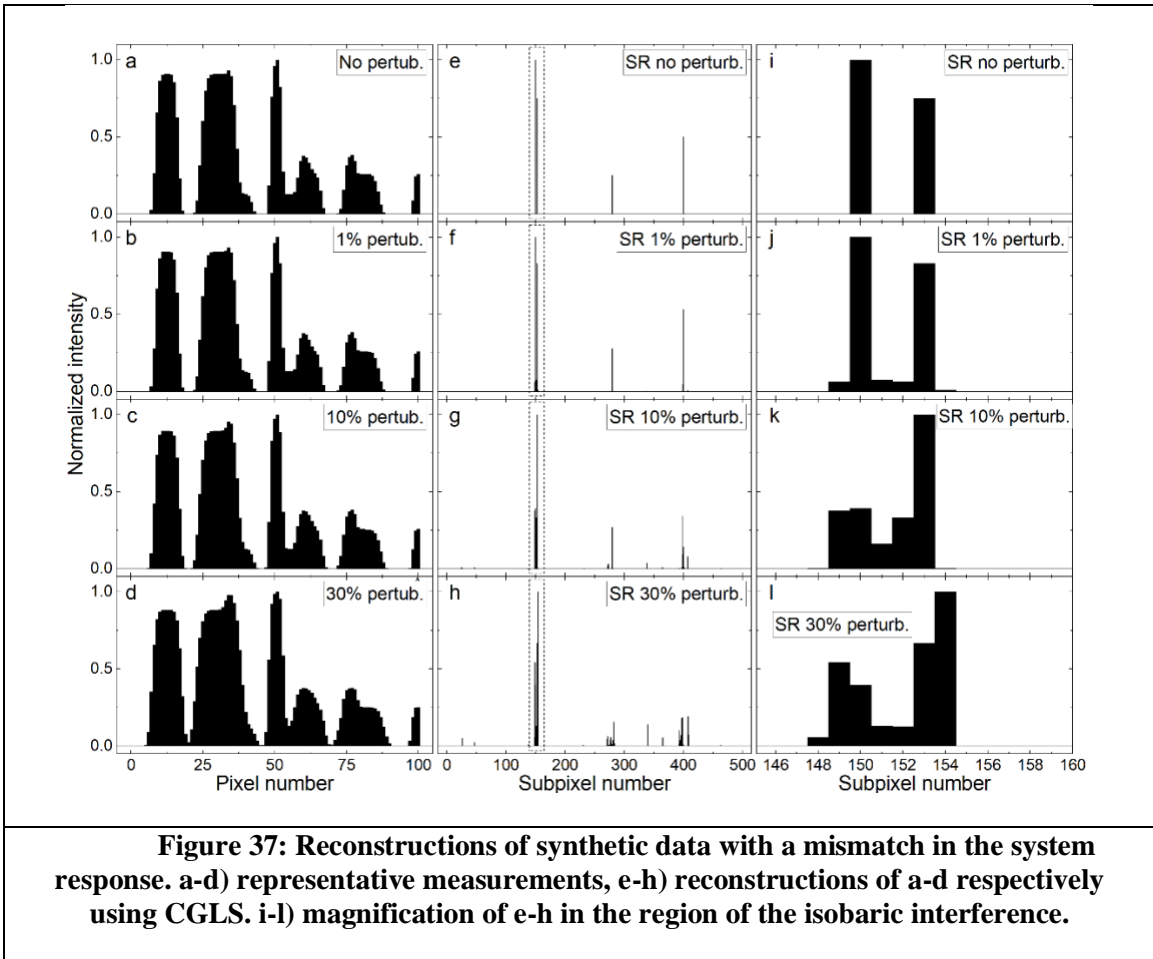


Figure 36: Reconstructions of synthetic data with variation in the sub-pixel shift. a-d) representative measurements, e-h) reconstructions of a-d respectively using CGLS. i-l) magnification of e-h in the region of the isobaric interference.



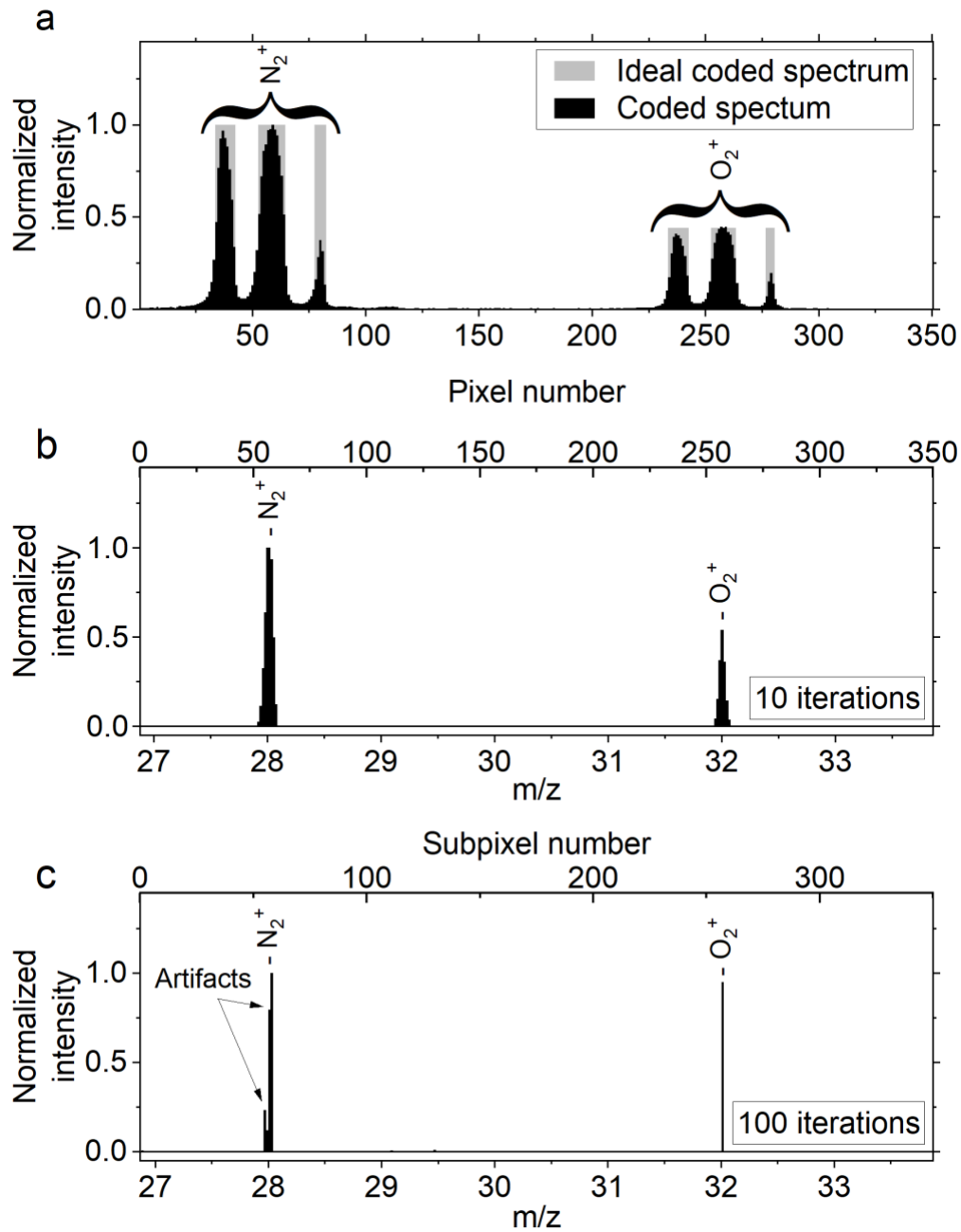


Figure 38: a. Coded mass spectrum of air. A sequence of 3 peaks appears at the detector for ions of each m/z . b. Richardson-Lucy low-resolution reconstruction using 10 iterations. c. Richardson-Lucy low-resolution reconstruction using 100 iterations. Increasing the number of iterations results in more artifacts and inaccurate peak intensities.

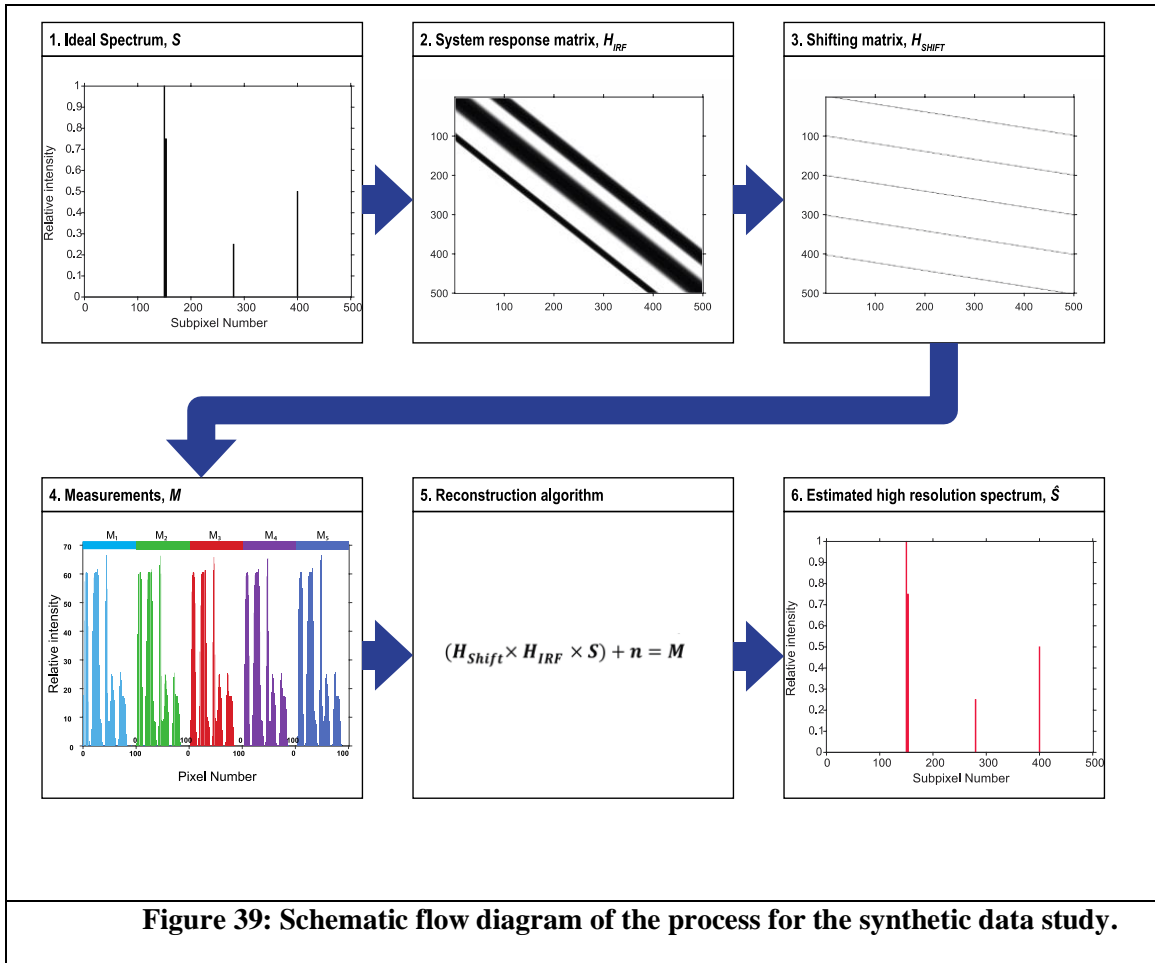


Figure 39: Schematic flow diagram of the process for the synthetic data study.

References

1. *Vision and Voyages for Planetary Science in the Decade 2013-2022*. 2011, Washington, DC: The National Academies Press.
2. NASA, *2014 Science Plan*.
3. Palmer, P.T. and T.F. Limero, *Mass spectrometry in the U.S. space program: past, present, and future*. Journal of the American Society for Mass Spectrometry, 2001. **12**(6): p. 656-675.
4. Karouia, F., K. Peyvan, and A. Pohorille, *Toward biotechnology in space: High-throughput instruments for in situ biological research beyond Earth*. Biotechnology Advances, 2017. **35**(7): p. 905-932.
5. Johnson, P.V., L.W. Beegle, and I. Kanik, *Mass Spectrometry in Solar System Exploration*, in *Mass Spectrometry Handbook*, M.S. Lee, Editor. 2012, John Wiley & Sons, Inc.: New York. p. 391-405.
6. Niemann, H., et al., *The abundances of constituents of Titan's atmosphere from the GCMS instrument on the Huygens probe*. Nature, 2005. **438**(7069): p. 779-784.
7. Mahaffy, P.R., et al., *The sample analysis at Mars investigation and instrument suite*. Space Science Reviews, 2012. **170**: p. 401-478.
8. Altwegg, K., et al., *Prebiotic chemicals—amino acid and phosphorus—in the coma of comet 67P/Churyumov-Gerasimenko*. Science advances, 2016. **2**(5): p. e1600285.
9. James, J.T. and A. Macatangay. *Carbon dioxide-Our common" Enemy"*. in *SAMAP Submarine Air Monitoring Air Purification Conference*. 2009.
10. Anderson, D.M., et al., *Mass spectrometric analysis of organic compounds, water and volatile constituents in the atmosphere and surface of Mars: The Viking Mars Lander*. Icarus, 1972. **16**(1): p. 111-138.
11. Biemann, K., *Test results on the Viking gas chromatograph-mass spectrometer experiment*. Origins of life, 1974. **5**(3): p. 417-430.
12. Biemann, K., et al., *The search for organic substances and inorganic volatile compounds in the surface of Mars*. Journal of Geophysical Research, 1977. **82**(28): p. 4641-4658.
13. Leshin, L.A., et al., *Volatile, Isotope, and Organic Analysis of Martian Fines with the Mars Curiosity Rover*. Science, 2013. **341**(6153).
14. Muccio, Z. and G.P. Jackson, *Isotope ratio mass spectrometry*. Analyst, 2009. **134**(2): p. 213-222.

15. Li, X., et al., *Mars Organic Molecule Analyzer (MOMA) laser desorption/ionization source design and performance characterization*. International Journal of Mass Spectrometry, 2017. **422**: p. 177-187.
16. esa, *The 'rebirth' of ESA's ExoMars Rosalind Franklin mission*. 2023.
17. Muccio, Z. and G. Jackson, *Isotope Ratio Mass Spectrometry*. The Analyst, 2009. **134**: p. 213-22.
18. Fred, G., et al., *The Mars Organic Molecule Analyzer (MOMA) Instrument: Characterization of Organic Material in Martian Sediments*. Astrobiology, 2017. **17**(6-7): p. 655-685.
19. Schwartz, J.C., M.W. Senko, and J.E. Syka, *A two-dimensional quadrupole ion trap mass spectrometer*. Journal of the American society for mass spectrometry, 2002. **13**(6): p. 659-669.
20. Brockwell, T.G., et al. *The mass spectrometer for planetary exploration (MASPEX)*. in *2016 IEEE Aerospace Conference*. 2016.
21. Koppelaar, D.W., et al., *MS Detectors*. Analytical Chemistry, 2005. **77**(21): p. 418 A-427 A.
22. Zhao, W., *Tianwen-1 and China's Mars exploration program*. National Science Review, 2021. **8**(2): p. nwaa285.
23. Witze, A., *A month on Mars: what NASA's Perseverance rover has found so far*. Nature, 2021. **591**(7851): p. 509-511.
24. Hoegg, E.D., et al., *Preliminary Figures of Merit for Isotope Ratio Measurements: The Liquid Sampling-Atmospheric Pressure Glow Discharge Microplasma Ionization Source Coupled to an Orbitrap Mass Analyzer*. Journal of The American Society for Mass Spectrometry, 2016. **27**(8): p. 1393-1403.
25. Amsden, J.J., et al., *Coded apertures in mass spectrometry*. Annual Review of Analytical Chemistry, 2017. **10**: p. 141-156.
26. Russell, Z.E., et al., *Two-dimensional aperture coding for magnetic sector mass spectrometry*. Journal of the American Society for Mass Spectrometry, 2015. **26**(2): p. 248-256.
27. Chen, E.X., et al., *Order of Magnitude Signal Gain in Magnetic Sector Mass Spectrometry Via Aperture Coding*. Journal of the American Society for Mass Spectrometry, 2015. **26**(9): p. 1633-1640.
28. Russell, Z.E., et al., *Compatibility of spatially coded apertures with a miniature Mattauch-Herzog mass spectrograph*. Journal of The American Society for Mass Spectrometry, 2016. **27**(4): p. 578-84.

29. Landry, D.M.W., et al., *Effects of Magnetic and Electric Field Uniformity on Coded Aperture Imaging Quality in a Cycloidal Mass Analyzer*. J Am Soc Mass Spectrom, 2018. **29**(2): p. 352-359.
30. Amsden, J.J., et al., *Proof of Concept Coded Aperture Miniature Mass Spectrometer Using a Cycloidal Sector Mass Analyzer, a Carbon Nanotube (CNT) Field Emission Electron Ionization Source, and an Array Detector*. J Am Soc Mass Spectrom, 2018. **29**(2): p. 360-372.
31. Nier, A.O. and M.B. McElroy, *Composition and structure of Mars' Upper atmosphere: Results from the neutral mass spectrometers on Viking 1 and 2*. Journal of Geophysical Research, 1977. **82**(28): p. 4341-4349.
32. Rushneck, D.R., et al., *Viking gas chromatograph–mass spectrometer*. Review of Scientific Instruments, 1978. **49**(6): p. 817-834.
33. Niemann, H.B., et al., *Pioneer Venus Orbiter Neutral Gas Mass Spectrometer Experiment*. IEEE Transactions on Geoscience and Remote Sensing, 1980. **GE-18**(1): p. 60-65.
34. Taylor, H.A., et al., *Bennett Ion Mass Spectrometers on the Pioneer Venus Bus And Orbiter*. IEEE Transactions on Geoscience and Remote Sensing, 1980. **GE-18**(1): p. 44-49.
35. Hoffman, J.H., R.R. Hodges, and K.D. Duerksen, *Pioneer Venus Large Probe Neutral Mass-Spectrometer*. Journal of Vacuum Science & Technology, 1979. **16**(2): p. 692-694.
36. Reinhard, R., *The Giotto encounter with comet Halley*. Nature, 1986. **321**: p. 313.
37. Balsiger, H., et al., *The ion mass spectrometer on Giotto*. Journal of Physics E: Scientific Instruments, 1987. **20**(6): p. 759.
38. Harpold, D., et al., *Galileo Probe Mass Spectrometer experiment*. Space Science Reviews, 1992. **60**: p. 111-142.
39. Waite, J.H., et al., *The Cassini Ion and Neutral Mass Spectrometer (INMS) Investigation*. Space Science Reviews, 2004. **114**(1): p. 113-231.
40. Niemann, H.B., et al., *The Gas Chromatograph Mass Spectrometer for the Huygens Probe*. Space Science Reviews, 2002. **104**(1): p. 553-591.
41. Young, D.T., et al., *Plasma Experiment for Planetary Exploration (PEPE)*. Space Science Reviews, 2007. **129**(4): p. 327-357.
42. Balsiger, H., et al., *Rosina – Rosetta Orbiter Spectrometer for Ion and Neutral Analysis*. Space Science Reviews, 2007. **128**(1): p. 745-801.

43. Goesmann, F., et al., *Cosac, The Cometary Sampling and Composition Experiment on Philae*. Space Science Reviews, 2007. **128**(1): p. 257-280.
44. Wright, I.P., et al., *Ptolemy – an Instrument to Measure Stable Isotopic Ratios of Key Volatiles on a Cometary Nucleus*. Space Science Reviews, 2007. **128**(1): p. 363-381.
45. Hoffman, J.H., R.C. Chaney, and H. Hammack, *Phoenix Mars Mission—The Thermal Evolved Gas Analyzer*. Journal of the American Society for Mass Spectrometry, 2008. **19**(10): p. 1377-1383.
46. Mahaffy, P.R., et al., *The Sample Analysis at Mars Investigation and Instrument Suite*. Space Science Reviews, 2012. **170**(1): p. 401-478.
47. ; Available from: wikipedia.org/wiki/Mass_Spectrometer_for_Planetary_Exploration.
48. Bleakney, W. and J.A. Hipple, Jr., *A new mass spectrometer with improved focusing properties*. Physical Review, 1938. **53**(7): p. 521-529.
49. Yates, R.C., *A Handbook on Curves and Their Properties*. 1947: J.W. Edwards.
50. Piacentino, E.L., et al., *The Long Neglected Cycloidal Mass Analyzer*. Analytical Chemistry, 2021. **93**(33): p. 11357-11363.
51. Hahn, Y.B., et al., *Channeltron Gain in Magnetic Fields*. Review of Scientific Instruments, 1972. **43**(4): p. 695-696.
52. Felton, J.A., et al., *Evaluation of a fourth-generation focal plane camera for use in plasma-source mass spectrometry*. Journal of Analytical Atomic Spectrometry, 2011. **26**(2): p. 300-304.
53. Amsden, J.J., et al., *Coded Apertures in Mass Spectrometry*. Annu Rev Anal Chem (Palo Alto Calif), 2017. **10**(1): p. 141-156.
54. Brady, D.J., *Optical imaging and spectroscopy*. 2009: John Wiley & Sons.
55. Wagadarikar, A.A., M.E. Gehm, and D.J. Brady, *Performance comparison of aperture codes for multimodal, multiplex spectroscopy*. Appl Opt, 2007. **46**(22): p. 4932-42.
56. MacCabe, K., et al., *Pencil beam coded aperture x-ray scatter imaging*. Optics Express, 2012. **20**(15): p. 16310-16320.
57. Amsden, J.J., et al., *Proof of Concept Coded Aperture Miniature Mass Spectrometer Using a Cycloidal Sector Mass Analyzer, a Carbon Nanotube (CNT) Field Emission Electron Ionization Source, and an Array Detector*. Journal of the American Society for Mass Spectrometry, 2018. **29**(2): p. 360-372.
58. Russell, Z.E., et al., *Compatibility of Spatially Coded Apertures with a Miniature Mattauch-Herzog Mass Spectrograph*. J Am Soc Mass Spectrom, 2016. **27**(4): p. 578-84.

59. Russell, Z.E., et al., *Two-dimensional aperture coding for magnetic sector mass spectrometry*. J Am Soc Mass Spectrom, 2015. **26**(2): p. 248-56.
60. Vyas, R., et al., *Improving the Performance of a Cycloidal Coded-Aperture Miniature Mass Spectrometer*. Journal of the American Society for Mass Spectrometry, 2020. **32**(2): p. 509-518.
61. Gazit, S., et al., *Super-resolution and reconstruction of sparse sub-wavelength images*. Optics Express, 2009. **17**(26): p. 23920-23946.
62. Abd-Almajeed, A. and F. Langevin, *Sub-pixel shifted acquisitions for super-resolution proton magnetic resonance spectroscopy (1H MRS) mapping*. Magnetic Resonance Imaging, 2015. **33**(4): p. 448-458.
63. Radauscher, E.J., et al., *Chemical Ionization Mass Spectrometry Using Carbon Nanotube Field Emission Electron Sources*. Journal of The American Society for Mass Spectrometry, 2015. **26**(11): p. 1903-1910.
64. Radauscher, E.J., et al., *A miniature electron ionization source fabricated using microelectromechanical systems (MEMS) with integrated carbon nanotube (CNT) field emission cathodes and low-temperature co-fired ceramics (LTCC)*. International Journal of Mass Spectrometry, 2017. **422**: p. 162-169.
65. Liang-Yu, C., et al., *A Microionizer for Portable Mass Spectrometers Using Double-Gated Isolated Vertically Aligned Carbon Nanofiber Arrays*. IEEE Transactions on Electron Devices, 2011. **58**(7): p. 2149-2158.
66. Vyas, R., et al., *Comparison of thermionic filament and carbon nanotube field emitter-based electron ionization sources in cycloidal coded aperture mass analyzers*. International Journal of Mass Spectrometry, 2020. **457**: p. 116415.
67. Jonge, N.d., et al., *Low noise and stable emission from carbon nanotube electron sources*. Applied Physics Letters, 2005. **87**(13): p. 133118.
68. Pandey, A., et al., *Stable Electron Field Emission from PMMA–CNT Matrices*. ACS Nano, 2010. **4**(11): p. 6760-6766.
69. Yu Dian, L., et al., *Field emission properties of SiO₂-wrapped CNT field emitter*. Nanotechnology, 2018. **29**(1): p. 015202.
70. Pandey, A., et al., *Very Stable Electron Field Emission from Strontium Titanate Coated Carbon Nanotube Matrices with Low Emission Thresholds*. ACS Nano, 2013. **7**(1): p. 117-125.
71. Arevalo Jr, R., Z. Ni, and R.M. Danell, *Mass spectrometry and planetary exploration: A brief review and future projection*. Journal of Mass Spectrometry, 2020. **55**(1): p. e4454.

72. Sloane, N.J. and M. Harwit, *Hadamard Transform Optics*. 1979, Academic Press New York.
73. Gehm, M.E., et al., *Static two-dimensional aperture coding for multimodal, multiplex spectroscopy*. Appl. Opt., 2006. **45**(13): p. 2965-2974.
74. Eckhardt, C.J. and M.L. Gross, *A proposed technique for signal multiplexing in mass spectrometry*. International Journal of Mass Spectrometry and Ion Physics, 1970. **5**(3): p. 223-227.
75. Jacquinet, P., *New developments in interference spectroscopy*. Reports on progress in physics, 1960. **23**(1): p. 267.
76. Fellgett, P., *Conclusions on multiplex methods*. Le Journal de Physique Colloques, 1967. **28**(C2): p. C2-165-C2-171.
77. Vyas, R., et al., *Improving the Performance of a Cycloidal Coded-Aperture Miniature Mass Spectrometer*. J Am Soc Mass Spectrom, 2021. **32**(2): p. 509-518.
78. Robinson, C.F. and L.G. Hall, *Small general purpose cycloidal-focusing mass spectrometer*. Review of Scientific Instruments, 1956. **27**(7): p. 504-508.
79. Horvath, K.L., et al., *Design considerations for a cycloidal mass analyzer using a focal plane array detector*. Journal of Mass Spectrometry, 2022. **57**(7): p. e4874.
80. Aloui, T., et al., *A Super-Resolution proof of concept in a cycloidal coded aperture miniature mass spectrometer*. Rapid Commun Mass Spectrom, 2023: p. e9477.
81. Nier, A.O., *A mass spectrometer for routine isotope abundance measurements*. Review of Scientific Instruments, 1940. **11**(7): p. 212-216.
82. Richardson, W.H., *Bayesian-based iterative method of image restoration*. JoSA, 1972. **62**(1): p. 55-59.
83. Lucy, L.B., *An iterative technique for the rectification of observed distributions*. The astronomical journal, 1974. **79**: p. 745.
84. Griffiths, J., *A brief history of mass spectrometry*. Anal Chem, 2008. **80**(15): p. 5678-83.
85. Snyder, D.T., et al., *Miniature and Fieldable Mass Spectrometers: Recent Advances*. Analytical Chemistry, 2016. **88**(1): p. 2-29.
86. Yu, Z., et al., *Real time analysis of trace volatile organic compounds in ambient air: a comparison between membrane inlet single photon ionization mass spectrometry and proton transfer reaction mass spectrometry*. Analytical Methods, 2020. **12**(35): p. 4343-4350.

87. McDonald, B.C., et al., *Volatile chemical products emerging as largest petrochemical source of urban organic emissions*. *Science*, 2018. **359**(6377): p. 760-764.
88. Mach, P.M., et al., *A portable mass spectrometer study targeting anthropogenic contaminants in Sub-Antarctic Puerto Williams, Chile*. *International Journal of Mass Spectrometry*, 2016: p. In Press <http://doi.org/10.1016/j.ijms.2016.12.008>.
89. Petrie, B., R. Barden, and B. Kasprzyk-Hordern, *A review on emerging contaminants in wastewaters and the environment: Current knowledge, understudied areas and recommendations for future monitoring*. *Water Research*, 2015. **72**: p. 3-27.
90. Reid, M.C., et al., *Global Methane Emissions from Pit Latrines*. *Environmental Science & Technology*, 2014. **48**(15): p. 8727-8734.
91. Sanders, N.L., et al., *Detection of explosives as negative ions directly from surfaces using a miniature mass spectrometer*. *Analytical Chemistry*, 2010. **82**(12): p. 5313-5316.
92. National Academies of Sciences, E., and Medicine. , *Strategy for Improving Trace Detection Capabilities. Opportunities to Improve Airport Passenger Screening with Mass Spectrometry*. Washington, DC: The National Academies Press., 2004.
93. Snyder, D.T., et al., *Miniature and Fieldable Mass Spectrometers: Recent Advances*. *Anal Chem*, 2016. **88**(1): p. 2-29.
94. Page, J.S., C.D. Masselon, and R.D. Smith, *FTICR mass spectrometry for qualitative and quantitative bioanalyses*. *Current opinion in biotechnology*, 2004. **15**(1): p. 3-11.
95. Marshall, A.G. and C.L. Hendrickson, *High-resolution mass spectrometers*. *Annual review of analytical chemistry*, 2008. **1**(1): p. 579.
96. Eliuk, S. and A. Makarov, *Evolution of orbitrap mass spectrometry instrumentation*. *Annu. Rev. Anal. Chem*, 2015. **8**(1): p. 61-80.
97. Arnaud, C.H., *Mini mass specs are still looking for an audience*, in *cen acs*. 2018.
98. Sung Cheol, P., P. Min Kyu, and K. Moon Gi, *Super-resolution image reconstruction: a technical overview*. *IEEE Signal Processing Magazine*, 2003. **20**(3): p. 21-36.
99. Xu, L., et al., *Resolution enhancement by combination of subpixel and deconvolution in miniature spectrometers*. *Appl Opt*, 2007. **46**(16): p. 3210-4.
100. Chung, J., E. Haber, and J. Nagy, *Numerical methods for coupled super-resolution*. *Inverse Problems*, 2006. **22**(4): p. 1261-1272.
101. Chu, N., *Super-résolution: Création d'une séquence d'images hautes résolutions à partir d'une séquence d'images basses résolution*. 2010.

102. Pernechele, C., et al., *Spectral resolution improvement technique for a spectrograph mounting a discrete array detector*. SPIE's 1995 International Symposium on Optical Science, Engineering, and Instrumentation. Vol. 2517. 1995: SPIE.
103. Piacentino, E.L., et al., *The Long Neglected Cycloidal Mass Analyzer*. Anal Chem, 2021. **93**(33): p. 11357-11363.
104. Serpa, R.B., et al., *Virtual-slit focusing in a cycloidal mass spectrometer – A proof of concept*. International Journal of Mass Spectrometry, 2021: p. 116706.
105. Horvath, K.L., et al., *Design considerations for a cycloidal mass analyzer using a focal plane array detector*. Journal of Mass Spectrometry, 2022. **57**(7): p. e4874.
106. Russell*, Z.E., et al., *Two-Dimensional Aperture Coding for Magnetic Sector Mass Spectrometry*. Journal of The American Society for Mass Spectrometry, 2015. **26**(2): p. 248-256.
107. Xu, L., et al., *Resolution enhancement by combination of subpixel and deconvolution in miniature spectrometers*. Applied Optics, 2007. **46**(16): p. 3210-3214.
108. Pernechele, C., et al., *Spectral resolution improvement technique for a spectrograph mounting a discrete array detector*. Optical Engineering, 1996. **35**(5).
109. Poletto, L. and P. Nicolosi, *Enhancing the spatial resolution of a two-dimensional discrete array detector*. Optical Engineering, 1999. **38**(10).
110. van Oosterom, A., *History and Evolution of Methods for Solving the Inverse Problem*. Journal of Clinical Neurophysiology, 1991. **8**(4): p. 371-380.
111. Hadamard, J., *Sur les problèmes aux dérivées partielles et leur signification physique*. Princeton university bulletin, 1902: p. 49-52.
112. Kabanikhin, S.I., *Definitions and examples of inverse and ill-posed problems*. 2008.
113. Mueller, J.L. and S. Siltanen, *Linear and nonlinear inverse problems with practical applications*. 2012: SIAM.
114. LEE, D.Q., *NUMERICALLY EFFICIENT METHODS FOR SOLVING LEAST SQUARES PROBLEMS*. 2012.
115. Siltanen, J.L.M.a.S., *linear and nonlinear inverse problems with practical applications*. 2012.
116. Amita Garg¹, K.G., *Regularization Methods to Solve Various Inverse Problems*. International Journal of Science and Research (IJSR), 2014.
117. Lawson, C.L. and R.J. Hanson, *Solving least squares problems*. 1995: SIAM.

118. Tikhonov, A.N. *Regularization of incorrectly posed problems*. in *Soviet Mathematics Doklady*. 1963.
119. Lawson, C.L.H.R.J.S.f.I. and M. Applied, *Solving least squares problems*. 1995, Philadelphia, Pa.: Society for Industrial and Applied Mathematics.
120. Gazzola, S. and Y. Wiaux, *Fast nonnegative least squares through flexible Krylov subspaces*. *SIAM Journal on Scientific Computing*, 2017. **39**(2): p. A655-A679.
121. Gockenbach, M.S., *Linear Inverse Problems and Tikhonov Regularization*. 2016: Mathematical Association of America.
122. Bertero, M., *Regularization methods for linear inverse problems*, in *Inverse problems*. 1986, Springer. p. 52-112.
123. Egger, H. and H.W. Engl, *Tikhonov regularization applied to the inverse problem of option pricing: convergence analysis and rates*. *Inverse Problems*, 2005. **21**(3): p. 1027-1045.
124. Calvetti, D., G.H. Golub, and L. Reichel, *Estimation of the L-curve via Lanczos bidiagonalization*. *BIT Numerical Mathematics*, 1999. **39**(4): p. 603-619.
125. Hanke, M., *Limitations of the L-curve method in ill-posed problems*. *BIT Numerical Mathematics*, 1996. **36**(2): p. 287-301.
126. Gazzola, S., P.C. Hansen, and J.G. Nagy, *IR Tools: a MATLAB package of iterative regularization methods and large-scale test problems*. *Numerical Algorithms*, 2018. **81**(3): p. 773-811.
127. Lemmon, E., et al., *NIST chemistry WebBook, Nist standard reference database number 69*. National Institute of Standards and Technology, Gaithersburg, 2011.
128. Connelly, M., *Michael Connelly (2022). sgauss(t,Tfwhm,E,C,m)* (<https://www.mathworks.com/matlabcentral/fileexchange/61181-sgauss-t-tfwhm-e-c-m>), *MATLAB Central File Exchange*. Retrieved August 31, 2022. 2022.
129. Aloui, T., et al., *A super-resolution proof of concept in a cycloidal coded aperture miniature mass spectrometer*. *Rapid Commun Mass Spectrom*, 2023. **n/a**(n/a): p. e9477.
130. NASA, *2014 Science Plan*.
131. Amsden, J., et al., *Radiation Survivability of MEMS Microelectronic Circuits with Carbon Nanotube Field Emitters*. 2019.
132. Fowler, R.H. and L. Nordheim, *Electron emission in intense electric fields*. *Proceedings of the Royal Society of London. Series A, Containing Papers of a Mathematical and Physical Character*, 1928. **119**(781): p. 173-181.

133. Murphy, E.L. and R. Good Jr, *Thermionic emission, field emission, and the transition region*. Physical review, 1956. **102**(6): p. 1464.
134. Forbes, R.G., et al., *Fowler-Nordheim plot analysis: a progress report*. arXiv preprint arXiv:1504.06134, 2015.
135. Collins, C.M., *Ordered Nanomaterials for Electron Field Emission*. 2017, University of Cambridge.
136. Chernozatonskii, L., et al., *Electron field emission from nanofilament carbon films*. Chemical Physics Letters, 1995. **233**(1-2): p. 63-68.
137. Bonard, J.-M., et al., *Field emission properties of multiwalled carbon nanotubes*. Ultramicroscopy, 1998. **73**: p. 7-15.
138. De Heer, W.A., A. Chatelain, and D. Ugarte, *A carbon nanotube field-emission electron source*. Science, 1995. **270**(5239): p. 1179-1180.
139. Nojeh, A., *Carbon nanotube electron sources: from electron beams to energy conversion and optophonics*. ISRN Nanomaterials, 2014. **2014**.
140. Milne, W., et al., *Carbon nanotubes as field emission sources*. Journal of Materials Chemistry, 2004. **14**(6): p. 933-943.
141. Amsden, J.J., et al., *Proof of concept coded aperture miniature mass spectrometer using a cycloidal sector mass analyzer, a carbon nanotube (CNT) field emission electron ionization source, and an array detector*. Journal of The American Society for Mass Spectrometry, 2018. **29**(2): p. 360-372.
142. Radauscher, E.J., et al., *A miniature electron ionization source fabricated using microelectromechanical systems (MEMS) with integrated carbon nanotube (CNT) field emission cathodes and low-temperature co-fired ceramics (LTCC)*. International Journal of Mass Spectrometry, 2017. **422**: p. 162-169.
143. Evans-Nguyen, T., et al., *Carbon Nanotube Electron Ionization Source for Portable Mass Spectrometry*. Analytical Chemistry, 2011. **83**(17): p. 6527-6531.
144. Gaertner, G., *Historical development and future trends of vacuum electronics*. Journal of Vacuum Science & Technology B, Nanotechnology and Microelectronics: Materials, Processing, Measurement, and Phenomena, 2012. **30**(6): p. 060801.
145. Fowler, R.H. and L. Nordheim, *Electron emission in intense electric fields*. Proc. R. Soc. Lond. A, 1928. **119**(781): p. 173-181.
146. de Jonge, N., et al., *Low noise and stable emission from carbon nanotube electron sources*. Applied Physics Letters, 2005. **87**(13): p. 133118.

147. Kayastha, V.K., B. Ulmen, and Y.K. Yap, *Effect of graphitic order on field emission stability of carbon nanotubes*. Nanotechnology, 2007. **18**(3): p. 035206.
148. Ulmen, B., et al., *Stability of field emission current from various types of carbon nanotube films*. Diamond and Related Materials, 2006. **15**(2-3): p. 212-216.
149. Sun, Y., et al., *Field emission behavior of carbon nanotube field emitters after high temperature thermal annealing*. AIP advances, 2014. **4**(7): p. 077110.
150. Deng, J.-h., et al., *Temperature dependent field emission performances of carbon nanotube arrays: Speculation on oxygen desorption and defect annealing*. Applied Surface Science, 2012. **258**(18): p. 7094-7098.
151. Stoner, B.R., B. Brown, and J.T. Glass, *Selected topics on the synthesis, properties and applications of multiwalled carbon nanotubes*. Diamond and Related Materials, 2014. **42**: p. 49-57.
152. Brown, B., et al., *Growth of vertically aligned bamboo-like carbon nanotubes from ammonia/methane precursors using a platinum catalyst*. Carbon, 2011. **49**(1): p. 266-274.
153. Meyyappan, M., et al., *Carbon nanotube growth by PECVD: a review*. Plasma Sources Science and Technology, 2003. **12**(2): p. 205.
154. Bower, C., et al., *Plasma-induced alignment of carbon nanotubes*. Applied Physics Letters, 2000. **77**(6): p. 830-832.
155. Natarajan, S., *A study of field emission based microfabricated devices*. 2008, Duke University.
156. Pandey, A., et al., *Stable electron field emission from PMMA– CNT matrices*. Acs Nano, 2010. **4**(11): p. 6760-6766.
157. Kleint, C., *Surface diffusion model of adsorption-induced field emission flicker noise: II. Experiments*. Surface Science, 1971. **25**(2): p. 411-434.
158. Kleint, C.H., *Surface diffusion model of adsorption-induced field emission flicker noise: I. Theory*. Surface Science, 1971. **25**(2): p. 394-410.
159. Zhu, M., et al., *Enhanced field emission of vertically oriented carbon nanosheets synthesized by C₂H₂/H₂ plasma enhanced CVD*. Carbon, 2011. **49**(7): p. 2526-2531.
160. Knápek, A., et al., *Field emission from the surface of highly ordered pyrolytic graphite*. Applied Surface Science, 2017. **395**: p. 157-161.
161. Lisunova, M., et al., *Field emission properties of screen-printed activated carbons*. Carbon, 2009. **47**(4): p. 1119-1125.

162. Lee, C.J., J.H. Park, and J. Park, *Synthesis of bamboo-shaped multiwalled carbon nanotubes using thermal chemical vapor deposition*. Chemical Physics Letters, 2000. **323**(5-6): p. 560-565.
163. Gautier, L.-A., V. Le Borgne, and M.A. El Khakani, *Field emission properties of graphenated multi-wall carbon nanotubes grown by plasma enhanced chemical vapour deposition*. Carbon, 2016. **98**: p. 259-266.
164. Ubnoske, S.M., et al., *Perspectives on the growth of high edge density carbon nanostructures: Transitions from vertically oriented graphene nanosheets to graphenated carbon nanotubes*. Journal of Physical Chemistry C, 2014. **118**(29): p. 16126-16132.
165. de Heer, W.A., A. Châtelain, and D. Ugarte, *A Carbon Nanotube Field-Emission Electron Source*. Science, 1995. **270**(5239): p. 1179-1180.
166. Parker, C.B., et al., *Three-dimensional arrays of graphenated carbon nanotubes*. Journal of Materials Research, 2012. **27**(07): p. 1046-1053.
167. Stoner, B.R. and J.T. Glass, *Carbon nanostructures: A morphological classification for charge density optimization*. Diamond and Related Materials, 2012. **23**(0): p. 130-134.
168. Stoner, B.R., et al., *Graphenated carbon nanotubes for enhanced electrochemical double layer capacitor performance*. Applied Physics Letters, 2011. **99**(18).
169. Yu, K., et al., *Carbon nanotube with chemically bonded graphene leaves for electronic and optoelectronic applications*. The Journal of Physical Chemistry Letters, 2011. **2**(13): p. 1556-1562.

Biography

Tanouir Aloui is a Ph.D. candidate in the Department of Electrical and Computer Engineering at the Nanomaterials and Thin Films Lab (NTFL), Duke University. Her dissertation work lies at the intersection of nanomaterials and design of instrumentation with computational techniques. She is focused on integrating new technologies for use in space flight mass spectrometers including super-resolution coded aperture spectral reconstruction and carbon-nanotube based field emission electron ionization. These technologies will eventually enable a miniature super-resolution coded aperture mass spectrometer capable of high-precision isotope ratio measurements and low-mass isobaric separation. Tanouir first joined the NTFL at Duke in March 2015 as an intern. As part of her internship, she worked on Graphene-Insulator-Semiconductor Electron Emitter Cathode Development for Large Area Electron Lithography. This work was published in Applied Physics Letters. Before coming to Duke, she earned the *Diplôme d'ingénieur généraliste de l'École Centrale de Lyon* in 2017. She also earned her M.S in Nanoscale Engineering from Lyon University in France. She was awarded a Bachelor of Science in Physics and a Bachelor of Science in Mathematics from Versailles Saint-Quentin-en-Yvelines University (Paris). She speaks fluent Arabic and French.

List of publications:

In progress

Aloui, T., Vyas., R et al. (2023). Spectral reconstruction improvement in a cycloidal coded-aperture mass spectrometer. *Journal of Mass Spectrometry*

Published

Aloui, T., Serpa, RB., Abboud, N., et al. (2023). A Super-Resolution proof of concept in a cycloidal coded aperture miniature mass spectrometer. *Rapid Communications in Mass Spectrometry*, e9477.

Horvath, K. L., Piacentino, E. L., Serpa, R. B., **Aloui, T.**, Vyas, R., Zhilichev, Y., ... & Amsden, J. J. (2022). Design considerations for a cycloidal mass analyzer using a focal plane array detector. *Journal of Mass Spectrometry*, 57(7), e4874.

Piacentino, E., Serpa, R. B., Horvath, K. L., Vyas, R., **Aloui, T.**, ... & Amsden, J. J. (2021) The long neglected cycloidal mass analyzer. *Analytical chemistry, perspective article*

Serpa, R. B., Piacentino, E., Horvath, K. L., **Aloui, T.**, ... & Amsden, J. J. (2021) Virtual-Slit Focusing in a Cycloidal Mass Spectrometer – A Proof of Concept. *International Journal of Mass Spectrometry*

Aloui, T., Kirley, M. P., Vick, E., Hilton, A., Colon, P., Kim, W., ... & Gilchrist, K. H. (2020). High current density electron emission from an electrodeposited metal nanowire array. *Journal of Vacuum Science & Technology B, Nanotechnology and Microelectronics: Materials, Processing, Measurement, and Phenomena*, 38(4), 043204.

Vyas, R., **Aloui, T.**, Horvath, K., Herr, P. J., Kirley, M. P., Parker, C. B., ... & Amsden, J. J. (2020). Improving the Performance of a Cycloidal Coded-Aperture Miniature Mass Spectrometer. *Journal of the American Society for Mass Spectrometry*.

Vyas, R., Herr, P. J., **Aloui, T.**, Horvath, K., Kirley, M. P., Parker, C. B., ... & Amsden, J. J. (2020). Comparison of thermionic filament and carbon nanotube field emitter-based electron ionization sources in cycloidal coded aperture mass analyzers. *International Journal of Mass Spectrometry*, 457, 116415

Kirley, M. P., **Aloui, T.**, & Glass, J. T. (2017). Monolayer graphene-insulator-semiconductor emitter for large-area electron lithography. *Applied Physics Letters*, 110(23), 233109.